



MINISTÉRIO DA
CIÊNCIA, TECNOLOGIA
E INOVAÇÕES



sid.inpe.br/mtc-m21c/2020/05.20.19.22-TDI

EVALUATION OF ULF ACTIVITY ON THE ELECTRON TRANSPORTATION IN THE OUTER RADIATION BELT

José Paulo Marchezi

Doctorate Thesis of the Graduate Course in Space Geophysics/Science of the Solar-Terrestrial Environment, guided by Drs. Lívia Ribeiro Alves, Lígia Alves da Silva e David Gary Sibeck, approved in May 19, 2020.

URL of the original document:

<<http://urlib.net/8JMKD3MGP3W34R/42GSL8>>

INPE
São José dos Campos
2020

PUBLISHED BY:

Instituto Nacional de Pesquisas Espaciais - INPE
Gabinete do Diretor (GBDIR)
Serviço de Informação e Documentação (SESID)
CEP 12.227-010
São José dos Campos - SP - Brasil
Tel.:(012) 3208-6923/7348
E-mail: pubtc@inpe.br

**BOARD OF PUBLISHING AND PRESERVATION OF INPE
INTELLECTUAL PRODUCTION - CEPPII (PORTARIA Nº
176/2018/SEI-INPE):****Chairperson:**

Dra. Marley Cavalcante de Lima Moscati - Centro de Previsão de Tempo e Estudos
Climáticos (CGCPT)

Members:

Dra. Carina Barros Mello - Coordenação de Laboratórios Associados (COCTE)
Dr. Alisson Dal Lago - Coordenação-Geral de Ciências Espaciais e Atmosféricas
(CGCEA)
Dr. Evandro Albiach Branco - Centro de Ciência do Sistema Terrestre (COCST)
Dr. Evandro Marconi Rocco - Coordenação-Geral de Engenharia e Tecnologia
Espacial (CGETE)
Dr. Hermann Johann Heinrich Kux - Coordenação-Geral de Observação da Terra
(CGOBT)
Dra. Ieda Del Arco Sanches - Conselho de Pós-Graduação - (CPG)
Sílvia Castro Marcelino - Serviço de Informação e Documentação (SESID)

DIGITAL LIBRARY:

Dr. Gerald Jean Francis Banon
Clayton Martins Pereira - Serviço de Informação e Documentação (SESID)

DOCUMENT REVIEW:

Simone Angélica Del Ducca Barbedo - Serviço de Informação e Documentação
(SESID)
André Luis Dias Fernandes - Serviço de Informação e Documentação (SESID)

ELECTRONIC EDITING:

Ivone Martins - Serviço de Informação e Documentação (SESID)
Cauê Silva Fróes - Serviço de Informação e Documentação (SESID)



MINISTÉRIO DA
CIÊNCIA, TECNOLOGIA
E INOVAÇÕES



sid.inpe.br/mtc-m21c/2020/05.20.19.22-TDI

EVALUATION OF ULF ACTIVITY ON THE ELECTRON TRANSPORTATION IN THE OUTER RADIATION BELT

José Paulo Marchezi

Doctorate Thesis of the Graduate Course in Space Geophysics/Science of the Solar-Terrestrial Environment, guided by Drs. Lívia Ribeiro Alves, Lígia Alves da Silva e David Gary Sibeck, approved in May 19, 2020.

URL of the original document:

<<http://urlib.net/8JMKD3MGP3W34R/42GSL8>>

INPE
São José dos Campos
2020

Cataloging in Publication Data

Marchezi, José Paulo.

M332e Evaluation of ulf activity on the electron transportation in the outer radiation belt / José Paulo Marchezi. – São José dos Campos : INPE, 2020.

xxvi + 141 p. ; (sid.inpe.br/mtc-m21c/2020/05.20.19.22-TDI)

Thesis (Doctorate in Space Geophysics/Science of the Solar-Terrestrial Environment) – Instituto Nacional de Pesquisas Espaciais, São José dos Campos, 2020.

Guiding : Drs. Lívia Ribeiro Alves, Lígia Alves da Silva e David Gary Sibeck.

1. Radiation Belts. 2. ULF waves. 3. Magnetosphere.
4. Diffusion coefficients. I.Title.

CDU 52-854:52-6



Esta obra foi licenciada sob uma Licença [Creative Commons Atribuição-NãoComercial 3.0 Não Adaptada](https://creativecommons.org/licenses/by-nc/3.0/).

This work is licensed under a [Creative Commons Attribution-NonCommercial 3.0 Unported License](https://creativecommons.org/licenses/by-nc/3.0/).

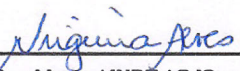
Aluno (a): **Jose Paulo Marchezi**

Título: " TÍTULO EM INGLES: EVALUATION OF ULF ACTIVITY ON THE ELECTRON TRANSPORTATION IN THE OUTER RADIATION BELT

TÍTULO EM PORTUGUES: AVALIAÇÃO DA ATIVIDADE DE ONDAS ULF NO TRANSPORTE DE ELÉTRONS NO CINTURÃO DE RADIAÇÃO EXTERNO"

Aprovado (a) pela Banca Examinadora em cumprimento ao requisito exigido para obtenção do Título de **Doutor(a)** em **Geofísica Espacial/Ciências do Ambiente Solar-Terrestre**

Dra. **Maria Virginia Alves**

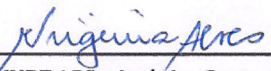


Presidente / INPE / SJCampos - SP

Participação por Video - Conferência

Aprovado () **Reprovado**

Dra. **Livia Ribeiro Alves**

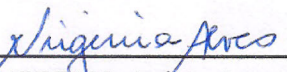


Orientador(a) / INPE / São José dos Campos - SP

Participação por Video - Conferência

Aprovado () **Reprovado**

Dra. **Ligia Alves da Silva**

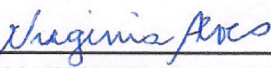


Orientador(a) / INPE / São José dos Campos - SP

Participação por Video - Conferência

Aprovado () **Reprovado**

Dr. **David Gary Sibeck**

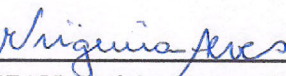


Orientador(a) / NASA / Washington, D.C. - USA

Participação por Video - Conferência

Aprovado () **Reprovado**

Dr. **Vitor Moura Cardoso e Silva Souza**



Convidado(a) / INPE / São José dos Campos - SP

Participação por Video - Conferência

Aprovado () **Reprovado**

Este trabalho foi aprovado por:

() **maioria simples**

unanimidade

Aprovado (a) pela Banca Examinadora
em cumprimento ao requisito exigido para
obtenção do Título de **Doutor(a)** em
**Geofísica Espacial/Ciências do Ambiente
Solar-Terrestre**

Dra. Aline de Lucas

Aline de Lucas

Convidado(a) / IFSP. / Jacareí - SP

Participação por Vídeo - Conferência

Aprovado () Reprovado

Dra. Flávia Reis Cardoso Rojas

Flávia Reis Cardoso Rojas

Convidado(a) / EEL - USP / Lorena - SP

Participação por Vídeo - Conferência

Aprovado () Reprovado

Este trabalho foi aprovado por:

() maioria simples

unanimidade

São José dos Campos, 19 de maio de 2020

*"All things must pass
None of life's strings can last
So I must be on my way
And face another day."*

GEORGE HARRISON
"All things must pass", 1970

A minha família.

ACKNOWLEDGEMENTS

In portuguese.

Agradeço primeiramente à Coordenação de Aperfeiçoamento de Pessoal de Nível Superior (CAPES) e ao Conselho Nacional de Desenvolvimento Científico e Tecnológico (CNPq), as bolsas de doutorado e auxílios concedidos para conferências e visitas técnicas a instituições de pesquisa do Brasil e no Exterior.

Meus agradecimentos, à Dra. Lívia Ribeiro Alves e à Dra. Ligia Alves da Silva suas orientações e discussões, compreensão e paciência no decorrer do desenvolvimento dessa tese e na minha formação como profissional.

Meus agradecimentos ao Dr. David G. Sibeck que me recebeu durante o período que passei nos EUA. (I'd like to thanks Dr. David Sibeck who received me during my time in the USA.)

Ao Instituto Nacional de Pesquisas Espaciais o ambiente de novas aprendizagens e as facilidades técnicas. Estendo esse agradecimento às secretárias, equipe de suporte técnico, funcionários e professores.

Ao programa de pós-graduação da Geofísica Espacial os recursos para a introdução a novas fronteiras do conhecimento.

Agradeço aos amigos que me acompanham desde o primeiro dia de mestrado aqui no INPE, Anna, Müller e Rodrigo. Estendo o agradecimento aos meus colegas de apartamento, em especial aos que convivi por mais tempo e durante o final do doutorado, Vinícius, Breno, Guilherme e André a amizade, ajuda, o companheirismo e parceria indispensável durante o doutorado.

Meus mais sinceros agradecimentos a meus pais, Genuir e Ivete, e a minha irmã Liana a minha gratidão pelo incentivo aos estudos e a felicidade de estarmos juntos em todas as batalhas. Também agradeço muito a meu irmão, Paulo, a ajuda, as dicas e discussões durante todo o período de construção e desenvolvimento do trabalho. A Priscila agradeço o carinho, a paciência, o apoio, o incentivo e o companheirismo durante o final dessa jornada.

Agradeço aos colegas da Dom Rock a disponibilidade, compreensão e convivência necessárias no final do desenvolvimento deste trabalho.

ABSTRACT

Van Allen's radiation belts consist of two regions with entrapment of charged particles in the Earth's magnetic field: inner and outer belts. The inner belt is composed mainly of protons with energies between 100 keV and a few hundred MeV. The outer belt is primarily consisting of high-energy electrons, ranging from dozens of keV to a few dozen MeV. Those particles rotate around the field line, mirroring movement along the magnetic field line and a drift movement around the Earth. Each movement has a particular time and is associated with an adiabatic invariant. Changes in the configuration of the solar magnetic field influence the solar wind and, consequently, all planets and spaceships within the heliosphere can be affected by disturbances of the solar wind. Interplanetary Coronal Mass Ejections (ICME) and fast solar wind High-Speed Streams (HSS), cause disturbances in the Earth's magnetosphere, including radiation belts from Van Allen. ICME events are more frequent during the growing phase of the solar cycle, while HSS is more critical during the declining period. The characteristics of the disturbances observed in the flux of electrons from the outer radiation belt due to these events are also different. Since October 2012, NASA initiated the Van Allen Probes mission that monitors, among other parameters, the magnetic field and the variation of particles in the radiation belts. The main objective of this work is to describe, based on observational data, the radial diffusion mechanism in the presence of ULF waves. For this, it is necessary to explain the role of ULF waves in the frequency bands corresponding to the natural oscillations of the magnetosphere, that is, Pc4 and Pc5, observed in the region of the external radiation belt, during periods of increased relativistic electron flux in the outer radiation belt. The energy penetration capacity as a function of the L-shell of the magnetosphere was investigated for the different frequency ranges considered in this research. The radiation belt events were investigated when related to HSS and ICME occurrences. Statistical results considering all ICMEs and HSS during the Van Allen Probes era show that for both solar wind structures, solar wind plasma parameters are strongly related to the radiation belt response at $L - shell = 5 R_E$, and on average they show a higher magnitude compared to those related to decrease in particle flux. Also, the ULF wave power is obtained as being more intense throughout enhancement events. Finally, we compare the integrated ULF wave power measured by the satellites and obtained via empirical modeling, for each L-shell, the results show that the empirical model overestimates integrated power for all the investigated L-shells and its discrepancy is increased at higher L-shells.

Keywords: Radiation Belts. ULF waves. Magnetosphere. Diffusion coefficients.

AValiação DA ATIVIDADE DE ONDAS ULF NO TRANSPORTE DE ELÉTRONS NO CINTURÃO DE RADIAÇÃO EXTERNO

RESUMO

Os cinturões de radiação de Van Allen consistem em duas regiões com aprisionamento de partículas carregadas no campo magnético da Terra: cinturão interno e externo. O cinturão interno é composto principalmente de prótons com energias entre 100 keV e algumas centenas de MeV. O cinturão externo, é composto principalmente por elétrons de altas energias, variando de dezenas de keV e algumas dezenas de MeV. Essas partículas realizam três movimentos periódicos: giro em torno da linha de campo, movimento de espelhamento ao longo da linha de campo magnético e um movimento de deriva em torno da Terra. Cada movimento possui um tempo característico e está associado a um invariante adiabático. As mudanças na configuração do campo magnético solar influenciam o vento solar e, conseqüentemente, todos os planetas e espaçonaves dentro da heliosfera podem ser afetados por perturbações do vento solar. As Ejeções de Massa Coronal Interplanetárias (*Interplanetary Coronal Mass Ejection* - ICMEs) e os feixes rápidos do vento solar (*High Speed Streams* - HSS), causam distúrbios na magnetosfera da Terra, incluindo os cinturões de radiação de Van Allen. Os eventos de ICME são mais frequentes durante a fase crescente do ciclo solar, enquanto os HSS são mais importantes durante a fase de declínio. As características dos distúrbios observados no fluxo de elétrons do cinturão de radiação externo devido a esses eventos também são diferentes. Desde outubro de 2012, a NASA iniciou a Missão Van Allen Probes que monitora o campo magnético e a variação de partículas nos cinturões de radiação. O objetivo principal deste trabalho é descrever, a partir de dados observacionais, o mecanismo de difusão radial na presença de ondas ULF. Para isso, é preciso descrever o papel das ondas ULF nas faixas de frequências correspondentes as oscilações naturais da magnetosfera, ou seja, Pc3, Pc4 e Pc5, observadas na região do cinturão externo de radiação, durante períodos de aumento de fluxo de elétrons relativísticos no cinturão externo de radiação. Serão investigadas a capacidade de penetração de energia em função das camadas L (*L-shell*) da magnetosfera, para as diferentes faixas de frequência consideradas nessa pesquisa. Com a finalidade de associar os eventos a perturbações geomagnéticas, serão considerados os eventos relacionados a ocorrências de HSS e ICME. Os resultados estatísticos, considerando todos os ICMEs e HSS durante a era de Van Allen Probes, mostram que, para ambas as estruturas de vento solar, os parâmetros do plasma de vento solar estão fortemente relacionados à resposta do cinto de radiação em $L - shell = 5 R_E$ e, em média, mostram uma magnitude maior em comparação com aqueles relacionado à diminuição do fluxo de partículas. Além disso, a potência da onda ULF é obtida como sendo mais intensa durante os eventos de aprimoramento. Por fim, comparamos a potência de onda ULF integrada medida pelos satélites e obtida por modelagem empírica, valor de *L-shell*, os resultados mostram que o modelo empírico superestima a potência integrada para cada valor de *L-shell* investigadas e sua discrepância é aumentada em *L-shell* mais altos.

Keywords: Cinturões de Radiação. Ondas ULF. Magnetosfera. Coeficiente de difusão.

LIST OF FIGURES

	<u>Page</u>
3.1 The figure presents a scheme showing the interaction of the solar wind with the Earth. The left panel represents the field lines moving with the fast (slow) solar wind, in red (blue). On the right, an observer's view on Earth.	9
3.2 The figure shows a schematic representation of an ICME and its shock wave reaching the Earth.	11
3.3 Artistic representation of the interaction between a rapid flow of the solar wind and the Earth's magnetosphere. The HSS is in yellow, and the coronal holes on the solar surface are the darkest parts of the solar corona, the Earth's magnetic field is represented in blue, the radiation belts in red.	13
4.1 A cross-section representation of the IMF and magnetosphere intersection region (bow shock) and the main regions at magnetosphere	16
4.2 Scheme exemplifying shear disturbances at the magnetopause generating Kelvin-Helmholtz instability and a magnetopause disturbance that compresses the plasma, generating waves that propagate towards the Earth. These modes can couple with the dipole field and generate resonances that can be recorded on the ground.	22
4.3 Scheme exemplifying shear disturbances in the magnetopause generating Kelvin-Helmholtz instability and a magnetopause disturbance that compresses the plasma, generating waves that propagate towards the Earth. These modes can couple with the dipole field and generate resonances that can be recorded on the ground.	24
4.4 Artistic visualization of radiation belts. The trapped particles form two toroidal regions, called Van Allen Radiation Belts	26
4.5 Trajectory of particles trapped in the geomagnetic field lines.	27
5.1 Spatial arrangement of the CARISMA network magnetometers, with Churchill line sensors indicated by the red rectangle.	35
5.2 Spatial arrangement of the IMAGE network magnetometers, with the sensors used indicated by the red rectangle.	36
5.3 Example of PostgreSQL data storage architecture. The structure and information contained in each table are presented.	39

5.4	Example of a Superposed Epoch Analysis using 40 ICME events with increased electron flux in the external radiation belt.	42
5.5	Vector elements of the magnetic field of the Earth.	47
5.6	Average power in the range of Pc5, for the horizontal component, along the IMAGE network located at approximately 110 CGM longitude for the period from 20 to 24 April 2003. The vertical axis represents the values for <i>L-shell</i> as a function of time in UT and MLT, the colors represent the average value of the wave power.	51
5.7	Diagram showing the steps to fit the curves on the PhSD calculation.	57
5.8	Diagram depicting the different signatures of radial diffusion (Panel A) and local acceleration (Panel B).	58
6.1	(a) Number of ICME and HSS events per year, arriving on Earth, related to changes in electron flux observed during the first four years of the Van Allen Probes mission. (b) The proportion of events that may be associated with dropouts or acceleration in the flux of electrons from the outer belt. In the panel (b)-left are the HSS related events and the panel (b)-right show the ICME related events.	61
6.2	Superposed Epoch analysis on the 2.10 MeV electron flux and solar wind parameters for flux enhancements (panels a, c, e, and g) and reduction (panels b, d, f and h), for ICME events. The solid blue line corresponds to the median, while the yellow ones are the upper and lower quartiles. From top to bottom: Relativist electron flux density, solar wind speed, proton density and Interplanetary Magnetic Field (IMF) in the z-component.	63
6.3	Superposed Epoch analysis for the electron flux density in L-shell ranging from 3 to 5.5 R_E , in cases of enhancement (Left) and reduction (Right), during coronal mass ejection events.	65
6.4	Superposed Epoch analysis for the AE index, for enhancement (Left) and reduction (Right), during coronal mass ejection events. The same configuration and color lines as Figure 6.2.	66
6.5	Superposed Epoch analysis on the 2.10 MeV electron flux and solar wind parameters for flux enhancements (panels a, c, e, and g) and reduction (panels b, d, f and h), for HSS events. The solid blue line corresponds to the median, while the yellow ones are the upper and lower quartiles. From top to bottom: Relativist electron flux density, solar wind speed, proton density and Interplanetary Magnetic Field (IMF) in the z-component.	68

6.6	Superposed Epoch analysis for the electron flux density in L-shell ranging from 3 to 5.5 R_E , in cases of enhancement (Left) and reduction (Right), during solar wind high-speed streams events.	69
6.7	Superposed Epoch analysis for the AE index, for enhancement (Left) and reduction (Right), during HSS events. The same configuration and color lines as Figure 6.2	70
6.8	Superposed Epoch Analysis Pc5 Power Spectral Density in L-shell values from 3.5 to 5.0 during flux enhancements (panels a, c, e, and g) and reduction (panels b, d, f and h), for ICME events. The solid blue line correspond to the median, while the yellow ones are the upper and lower quartile.	73
6.9	Superposed Epoch Analysis Pc5 Power Spectral Density in L-shell values from 3.5 to 5.0 during flux enhancements (panels a, c, e, and g) and reduction (panels b, d, f and h), for HSS events. The solid blue line correspond to the median, while the yellow ones are the upper and lower quartile.	74
6.10	Power Spectrum Density for the compressional magnetic field at $L^* = 5.5$ and MLT sectors of 0, 6, 12 and 18 for all ICME events. The lines colored red shows the upper and lower quartile, the mean is in black and the median in blue.	78
6.11	Power Spectrum Density for the azimuthal electric field component E_{phi} at $L^* = 5.5$ and MLT sectors of 0, 6, 12 and 18 for all ICME events. The lines colored red shows the upper and lower quartile, the mean is in black and the median in blue.	80
6.12	Drift averaged Power Spectrum Density, integrated over the frequency range range ~ 0.4 mHz to ~ 8 mHz versus L-shell, for all the paralell componet of the magnetic field (left) and the azimuthal component of the electric field (right). The red and green lines are the PSD for ICME and HSS events, respectively, estimated using the Equations 5.12 and 5.13. The blue and orange lines are the ICME and HSS PSD, calculated using our approximation.	82
6.13	The diffusion coefficients calculated using Ozeke et al. (2014) equation. This is a mean value for all Kp during the period chosen for each event type. The panels on the left are for ICME events, and on the right are the HSS events. The gray lines represent the maximum and minimum values in each L-shell.	83

7.1	From top: (a) Electron flux density at 2.10 MeV energy as a function of L^* (vertical axes) and time (horizontal axis); (b) 2.10 MeV electron flux density at $L^* = 5.0ER$; (c) solar wind speed; (d) solar wind proton density; (e) Interplanetary Magnetic Field (IMF) B_z component; (f) B_x and B_y component of the IMF. The electron fluxes are obtained by the REPT instrument on board of the Van Allen Probes. The flux speed, Density, B_z , B_x and B_y are obtained by the Advanced Composition Explorer (ACE) satellite in the Lagrangian L1 point. Panel (f) shows the auroral activity index AE and the SYM-H index. The vertical dashed line shows the time of the enhancement on flux and the increase on solar wind speed coincident to the substorm expansion onset.	87
7.2	Flux density for low energies, panels (a) and (b), in the energy channels of 144 keV, 184 keV, 226 keV and 235 keV measured by the MagEIS instrument. The panels (c) and (d) the channels at higher energies, 1.8 MeV, 2.1 MeV, 2.6 MeV and 3.4 MeV registered by REPT instrument, both onboard Van Allen Probe A.	89
7.3	The power spectrum of ULF waves, within the frequency range between 1 to 10 mHz using data from the magnetometer network on the Earth's surface, IMAGE as a function of the McIlwain parameter, L-shell and time (UT and MLT) between the 7th until the 11th of February 2014.	91
7.4	(a) MagEIS electron flux density, energies range from 144 keV to 235 keV. (b) Flux of relativistic electrons from the REPT instrument, energies from 1.8 MeV to 3.4 MeV. (c), (d) and (e) present the ULF signal filtered in the frequency bands Pc3, Pc4 and Pc5 for the B_p component of the geomagnetic field, and for the E_ϕ and E_r components of the electric field.	93
7.5	(a) Ultralow-frequency (ULF) power spectral density in the 1 to 10 mHz frequency range (color scale) as a function of L-shell and time, during 9 February 2014. (b) Radial diffusion coefficient D_{LL} (color scale) as a function of L-shell (vertical axis-left) and time (horizontal axis) during 9 February 2014.	94
7.6	Temporal evolution of the radial profile of the phase space density to fixed values of the adiabatic invariants μ and K . The legend shows the start times of the orbit portions of the Van Allen A.	96

LIST OF TABLES

	<u>Page</u>
4.1	Classification scheme developed by IAGA in 1964. 20
5.1	Location of the 22 magnetic stations and their geomagnetic coordinates, together with the parameter L for each station. 37
A.1	All the events with flux variations related to ICME events. The columns represents the event type, the day that it occurs and the instant that the structure arrives and interact with Earth's magnetosphere. The last column show the 2.10 MeV electron flux density during the event, plotted with respect of L^* (y-axis) and time (x-axis). The period corresponds to 3 days before and after the event, marked with the dashed black line in each graph. 127
B.1	All the events with flux variations related to HSS events. The columns represents the event type, the day that it occurs and the instant that the structure arrives and interact with Earth's magnetosphere. The last column show the 2.10 MeV electron flux density during the event, plotted with respect of L^* (y-axis) and time (x-axis). The period corresponds to 3 days before and after the event, marked with the dashed black line in each graph. 135

LIST OF ABBREVIATIONS AND SYMBOLS

α	Pitch Angle
μ	First Adiabatic Invariant
ω	Wave frequency
ω_d	Particle drift frequency
B_{\parallel}	Parallel component of the magnetic field
D_{LL}	Diffusion Coefficient
Dst	Disturbance Storm Time Index
E_{ϕ}	Azimuthal component of Electric Field
E_r	Radial component of Electric Field
K	Second Adiabatic Invariant
Kp	Planetary K-Index
L^*	Roederer Parameter
m	Wave number
SD	Solar Disturbed
Sq	Solar quiet
ACE	Advanced Composition Explorer
CARISMA	Canadian Array for Realtime Investigations of Magnetic Activity
CIR	Corotating Interaction Region
CWT	Continuous Wavelet Transform
DFT	Discrete Fourier Transform

DWT	Discrete Wavelet Transform
EFW	Electric Field and Waves
EMFISIS	Electric and Magnetic Field Instrument Suite and Integrated Science
ER	Earth radii
FFT	Fast Fourier Transform
HSS	High-Speed Stream
ICME	Interplanetary Coronal Mass Ejection
IMAGE	International Monitor for Auroral Geomagnetic Effect
IMF	Interplanetary Magnetic Field
L	McIlwain parameter
MAG	Magnetic Field Experiment
MagEIS	Magnetic Electron Ion Spectrometer
MHD	Magnetohydrodynamic
MLT	Magnetic Local Time
Pc	Continuous Pulsation
PhSD	Phase Space Density
PSD	Power Spectral Density
REPT	Relativistic Electron Proton Telescope
SEA	Superposed Epoch Analysis
SWEPAM	Solar Wind Electron, Proton, and Alpha Monitor

T tesla

ULF Ultra-Low Frequency

CONTENTS

	<u>Page</u>
1 INTRODUCTION	1
2 OBJECTIVES AND JUSTIFICATIVE	5
3 THE INTERPLANETARY MEDIUM	7
3.1 Solar wind	8
3.2 Interplanetary Coronal Mass Ejections	9
3.3 High-Speed Streams	12
4 THE EARTH'S MAGNETOSPHERE	15
4.1 Main field	15
4.2 Geomagnetic field variation	17
4.3 Waves in the magnetosphere	19
4.3.1 Generation mechanisms of ULF waves	21
4.3.2 ULF waves propagation in the magnetosphere	23
4.4 Van Allen radiation belts	25
4.4.1 ULF wave-particle interaction	29
5 INSTRUMENTS, DATA AND ANALYSES TOOLS	33
5.1 Instrumentation	33
5.2 Database structure	37
5.3 Methodology	40
5.3.1 Event selection criteria	40
5.3.2 Superposed Epoch Analysis	41
5.3.3 Signal analysis	43
5.3.4 Ground-based instruments methodology	47
5.3.5 Satellite data methodology	49
5.4 ULF waves Power Spectrum Density - IMAGE and CARISMA	50
5.5 Diffusion Coefficients	51
5.6 Phase space density	55
6 STATISTICAL ANALYSIS	59
6.1 Coronal mass ejection events	61
6.2 High-speed streams events	67

6.3	Power spectrum	71
6.3.1	Integrated Power Spectrum	77
7	COMPLEX CASE STUDY	85
7.1	Solar wind conditions and electron flux density	85
8	CONCLUSIONS	99
	REFERENCES	105
	APPENDIX A - ICME EVENT DATES AND FLUX	127
	APPENDIX B - HSS EVENT DATES AND FLUX	135

1 INTRODUCTION

Since the end of the 1950 decade, two regions are known to have charged particles trapped in the Earth's magnetic field, the Van Allen Radiation Belts. The name was given in honor to the American scientist James Van Allen, who led the group responsible for the particle's detection experiments onboard the Explorer I e Explorer III satellites, in 1958. The first results showed the count of charged particles in the near-Earth space environment. However, the detection showed different energy ranges from those expected by the entire scientific community in the space area (HARGREAVES, 1992). The experiments also showed high-energy levels concentrated in two regions, called internal and external belts. The inner belt, between ~ 1 and 2 Earth's radii (ER), is predominantly populated by protons, with energies between 100 keV and a few hundred of MeV. The outer belt, is located between approximately 3 and 6 ER, is composed mainly of high energy electrons, ranging from dozens of keV to a few dozen of MeV.

In a more realistic view, the Van Allen belt region presents itself as a conjunction of particles statistically distributed in energy, a region in which the particles obey an approximately anisotropic distribution, occupying a smaller portion on its dayside and reaching up to 9 ER on the night side. The particles trapped in the outer radiation belt, especially the relativistic and ultra-relativistic ones, can be harmful to instruments on satellites (BAKER, 2001). Therefore, the study of the particles dynamics and their gain of energy in the terrestrial magnetosphere is a matter of great importance for the understanding and exploration of the near-Earth space environment.

The Earth's magnetosphere geometry causes charged particles, trapped in magnetic field lines, to perform a complex motion around the Earth. However, this complex motion can be understood as composed by three types of periodic movements, which have different time scales. The first type of movement refers to the particle rotation around the magnetic field line and has a particular period of milliseconds. The latitudinal movement, along the magnetic field lines, between two mirroring points, has a specific period between tenths of seconds to units of seconds. The third is the longitudinal drift movement around the Earth, with a time scale of a few minutes. Each of the three movements mentioned above is associated with a constant of motion that must be conserved under adiabatic changes of the magnetic field, i.e. when the period of the disturbances in the fields is longer than the time scales of the particle movements. These constants of motion are known as adiabatic invariants

(for a complete review on this subject see (BAUMJOHANN; TREUMANN, 1997)).

Under nominal solar wind conditions, the adiabatic invariants are kept constant since the changes in the fields are slow. However, during interactions between disturbed solar wind structures and Earth's magnetosphere, adiabatic invariants can be violated and the belt dynamics become highly complex, decreasing (dropout) or increasing (re-formation) the electron flux density (BORTNIK; THORNE, 2007; ARTEMYEV et al., 2013; THORNE et al., 2013; BAKER et al., 2014a; ALVES et al., 2016). Solar structures that generate intense and extreme storms, such as the Interplanetary Coronal Mass Ejections (ICMEs), are more frequent in periods of high solar activity. At the same time, the High-Speed Streams (HSS), are capable of producing weak and moderate geomagnetic activity, being more often in the descending phase of the solar activity cycle (GONZALEZ et al., 1994; TSURUTANI et al., 1995; ECHER et al., 2011). Through the disturbed solar wind interaction to the magnetosphere, the geomagnetic field can be perturbed in periods comparable to the charged particles constants of motion, which may cause the violation of adiabatic invariants. In this condition, the periodic motions can no longer be held. So, it is important to identify the adiabatic invariants that are not constant during the geomagnetic storm growth.

At the Earth's magnetosphere, the violation of one or more adiabatic invariants can lead to the occurrence of several critical dynamic processes, which are capable of altering the particle flow density in the outer radiation belt (ELKINGTON et al., 1999; ELKINGTON, 2006). Wave-particle interaction are the most common relation to broke adiabatic invariants, since the waves and charged particles motions frequencies can be comparable. Among the several wave-particle interaction types, the Ultra Low Frequency (ULF) waves have periods comparable to the eastward drift of electrons in the belt (GREEN; KIVELSON, 2001; NAKAMURA et al., 2002; MANN et al., 2004), besides they are known to be often observed in the magnetosphere and deliver high amounts of energy to the charged particles, being much related to the break the third adiabatic invariant.

In magnetosphere studies, the frequency range corresponding to ULF waves ranges from 1 mHz to 10 mHz (SAITO, 1969; JACOBS, 1991; PILIPENKO, 1990; MOLCHANOV et al., 2003). The manifestation of these magnetohydrodynamic (MHD) waves in the magnetosphere are also classified as magnetic pulsations, when their frequency reaches the normal resonante magnetospheric frequencies, divided into continuous pulsation (Pc), with a well-defined spectral peak, and irregular pulsation (Pi), when they involve a large frequency range. In this work, the focus of the study is on the fre-

quency range corresponding to Pc4 (6.6–22.2 mHz) and Pc5 (1.6–6.6 mHz) (SAITO, 1969; JACOBS, 1991). The mechanisms for generating these fluctuations can be either external to the magnetosphere, continuously or suddenly affected by the solar wind, or internal, mainly linked to abrupt transients in the magnetized plasma environment and the free energy stored in the terrestrial magnetosphere (YUMOTO, 1988).

Oscillations in the Pc5 range are generally observed at high latitudes, related to oscillations in the magnetospheric cavity (CLAUDEPIERRE et al., 2009b), Kelvin-Helmholtz instabilities and mirror drift waves. However, the occurrence of Pc5 at low latitudes, including equatorial latitudes, has been reported in recent years (TRIVEDI et al., 1997; HUDSON et al., 2004; CARVALHO et al., 2017; SILVA et al., 2020). At very low latitudes, they may be related to eddy currents of Pedersen’s ionospheric currents induced by the electric field of the Pc3 compressional wave that reaches the ionosphere. Saito (1983) proposed that peak occurrences of Pc3 at dusk in the subtropical region may be associated with electrical currents due to the source effect in the ionosphere. Satellite observations also revealed the existence of compression waves in the Pc4-5 range as well as shear Alfvén waves (BARFIELD; MCPHERRON, 1972; YUMOTO, 1988).

Several mechanisms of interaction between ULF waves and particles are proposed in the literature. However, the radial diffusion transport mechanism is considered by the scientific community to be one of the most efficient (FÄLTHAMMAR, 1965). Radial diffusion transport must first obey the resonance condition given by $\omega = m\omega_d$, where m is the azimuth wave number, and ω and ω_d are the frequency of the wave and the frequency of drift of the particle, respectively (SCHULZ; LANZEROTTI, 2012). The quantification of this mechanism must also consider that the process is stochastic, and can be described from the diffusion theory. Thus, some empirical models of radial diffusion are proposed in the literature to explain the interaction between ULF waves and particles by calculating the radial diffusion coefficient (OZEKE et al., 2014; BRAUTIGAM; ALBERT, 2000; ELKINGTON et al., 1999). Nonetheless, it is essential to highlight that they all consider the importance of the polarization modes of ULF waves in the efficiency of the interaction. The model of Elkington et al. (1999) considered an asymmetric field and quantify the efficiency of the toroidal mode, on the other hand, the model of Elkington et al. (2003) highlighted the importance of the poloidal and toroidal modes (ELKINGTON, 2006).

In this work we investigated the contribution of the ULF waves on the mechanisms

that lead to a radial diffusion, acting on the outer radiation belt particles flux, using ground measurements and in situ observational data. We performed the description of ULF waves in the frequency bands corresponding to the natural oscillations of the magnetosphere, i.e. Pc4 and Pc5 ULF frequency range. The outer radiation belt flux variation are usually related to changes in the geomagnetic field. The geomagnetic disturbance (not restricted to storms), are related to solar wind interplanetary events. For this work we've selected the flux variation events based on the solar wind structure that may cause the magnetospheric variation at the time when the relativistic electron flux content presents some change. We considered the solar wind High-Speed Stream and Interplanetary Coronal Mass ejection as a proxy for the flux variations in the outer radiation belt. The results intend to provide support for the improvement of the particle models, considering not only the geomagnetic conditions when the magnetosphere is highly disturbed by a geomagnetic storm but when the small perturbation can also affect the outer belt flux content.

The thesis is organized as follows.

In Chapter 2 are presented the objectives and the justification for this work.

In Chapter 3 an overview of the interplanetary medium as well as the geophysical phenomena related to the perturbations in the Earth's magnetosphere.

In Chapter 4 the phenomena related to the inner magnetosphere is presented as well as the characteristics of the geomagnetic pulsation and a introduction of the plasma physics related to this study.

In Chapter 5 are presented the database and the methodology used in this work.

In Chapter 6 the statistical analysis over all the HSS and ICME events related to flux variation is presented.

In Chapter 7 is presented a case study involving an complex interplanetary structure interacting with Earth's magnetosphere and related to an increase on outer radiation belt electron flux density.

In Chapter 8 are presented the conclusions of this work as well as the perspectives for future work.

2 OBJECTIVES AND JUSTIFICATIVE

Several physical mechanisms act to alter the dynamics of the outer radiation belt electrons. Among these mechanisms, it is considered that the activity of ULF waves has a great impact on the energy transfer to the particles, promoting particle diffusion to both inward and outward through the magnetosphere and may also cause the particles to accelerate. During the occurrence of geomagnetic disturbances, magnetohydrodynamic wave activity is observed in the same frequency range as the electron drift movement around the Earth. In the condition that these waves are resonant with the drift movement, significant changes in the flow of relativistic electrons are observed.

Although these phenomena have been described and investigated for decades, they are still not completely known since their correlation with solar events, such as ICME and HSS, generally associated with intense and moderate disturbances, respectively, are not fully described.

The proposed models used to quantify the wave-particle interaction due to ULF waves empirically relate the ULF waves power to the intensity of geomagnetic storms indices (OZEKE *et al.*, 2014), such as the planetary Kp and the Disturbance Storm time Index (Dst). Thought this significantly restricts the effectiveness of the models to the periods when the geomagnetic perturbation responsible for the the ULF waves generation is not as intense as those generated by an storm. In this scenario the well-established models fail (SILVA *et al.*, 2019). Furthermore, the empirical models are developed for the Pc5 frequencies, which are resonant with electrons from 1 to 2 MeV (SCHULZ; LANZEROTTI, 2012). This restriction prevents to describe the variation of the particles flow related to the other frequency ranges of ULF waves. To improve the results of the quantification of the radial diffusion coefficient during resonant interactions between the ULF waves and the electrons of the external belt in different frequency and energy ranges, the present work will use the physical model of Fei *et al.* (2006), using frequency bands, which refer to Pc4 and Pc5 integrated. With this, it is intended to contribute to the improvement of particle models, and especially to improve the effectiveness of calculating the radial diffusion coefficient for periods of weak and moderate storms, thus providing support for decision makers regarding the protection of space equipment.

In this context, the main objective of this work is to give a description of the radial diffusion mechanism due to ULF waves, acting on the outer radiation belt particles flux, using ground measurements and in situ observational data. To do that, it is

performed the description of ULF waves in the frequency bands corresponding to the natural oscillations of the magnetosphere, i.e. Pc4 and Pc5 ULF frequency range, observed in the region of external radiation belt, during periods of increased relativistic electron flux density in the external radiation belt. The ULF waves energy as a function of the L-shell of the magnetosphere will be investigated, for the different frequency ranges considered in this research. In order to associate events with geomagnetic disturbances (not restricted to storms), the events related to both HSS and ICME occurrences will be considered. The results intend to provide support for the improvement of the particle models, and thus contribute to the improvement of the outer radiation belt electron flux models during periods of external disturbances. The specific objectives to reach this are detailed in the following:

- 1) To carry out a survey of the HSS and ICME events in the period of interest related to this study;
- 2) To carry out a survey of the electron flux density data from the Van Allen probes;
- 3) To obtain ground magnetometer data over a wide range of latitudes;
- 4) To filter the data from ground magnetic field, and magnetic field and electric field from the Van Allen Probes in the ULF frequency ranges;
- 5) To calculate the power spectral density (PSD) for the filtered data;
- 6) To estimate the average behavior of the spectral power integrated in the frequency range during the periods of analysis to compare the events;
- 7) To calculate the diffusion coefficients related to empirical models and compare with the electric and magnetic fields power spectral density using the spectral power information during the analysis periods for ICME and HSS;
- 8) To obtain, for the different ULF waves frequency ranges, the depth of penetration of wave energy as a function of the L-shell, during the occurrence of ICME and HSS;
- 9) To develop computer programs to apply statistical tools for database analysis, adapted for events linked to ICME and HSS.

3 THE INTERPLANETARY MEDIUM

Until almost half of the last century, it was believed that there was nothing in the interplanetary space besides some explosions of energetic particles associated with solar flares. However, a new era, which began with the launch of the Sputnik satellite in 1957, has enabled more detailed studies of this region. Among these studies, it was verified that the solar wind which is a continuous source of plasma (PARKS, 1991; SCHUNK; NAGY, 2009) fill in the interplanetary environment. This observation lead to the Sun to be the primary source of energy for the various phenomena that occur in the Earth's space environment. The interaction of the solar wind super-Alfvénic and magnetized plasma with the Earth's magnetic field generates a region that surrounds our planet and governs the dynamics of the charged particles present in this medium, and which are under influence of this geomagnetic field. This region is called the magnetosphere. The solar wind dynamic pressure makes the side facing to the Sun takes the form of a compressed dipole, while on the night side, it has an elongated tail that reaches up to more than 200 terrestrial radii. The characteristics of this region and the dynamics involved is discussed through this chapter.

The Sun is the dominant source of energy and plasma in the solar system. Although the Sun is a relatively typical star in our galaxy, it is our nearest star. The Sun is classified as G2-V spectral type, with a radius of $r_{\odot} \approx 695,500$ km, a mass of $m_{\odot} \approx 1.98 \times 10^{30}$ kg, a luminosity of $L_{\odot} \approx 3.8 \times 10^{26}$ W, and an age of $t_{\odot} \approx 4.6 \times 10^9$ years (ASCHWANDEN, 2014). It is the main origin for the various processes that occur on Earth, both our climate and the interactions of the geomagnetic field with the interplanetary medium. The enormous pressures and temperatures generated by the star's gravitational force on ionized gases (mainly Helium and Hydrogen) cause them to be compressed and become the star's energy source. Nuclear fusion, collisions between particles and the strength of electromagnetic fields dominate in different regions of the Sun. Its interior can be subdivided into the following layers: core (the region where the fusion occurs), radiative zone, and convective zone (areas where the transport of the energy produced in the nucleus).

The solar atmosphere can be divided into photosphere (region between the interior of the Sun and its atmosphere), above that are chromosphere, and corona, the border region between the interplanetary medium and the Sun's atmosphere (GREEN et al., 2004). The corona has a relatively low density and high temperature. The huge difference in gas pressure between the solar corona and the interplanetary space drives the plasma outward in this region (KIVELSON; RUSSELL, 1995). This flow of

plasma, or solar wind, can become supersonic and super-Alfvénic (when speeds are greater than the Alfvén wave speed in plasma) as the solar activity evolves. If activity reaches the extreme level, a large amount of coronal mass can be released into the interplanetary medium in a short time, this phenomenon is known as Coronal Mass Ejections (CME) (BOTHMER; DAGLIS, 2007; PRIEST, 2014). Other sources of energy that affect the Earth’s environment include energy particles and electromagnetic emissions, such as X-rays, gamma rays, and ultraviolet radiation (BOTHMER; DAGLIS, 2007). In the following, some of the most energetic solar wind structures are described.

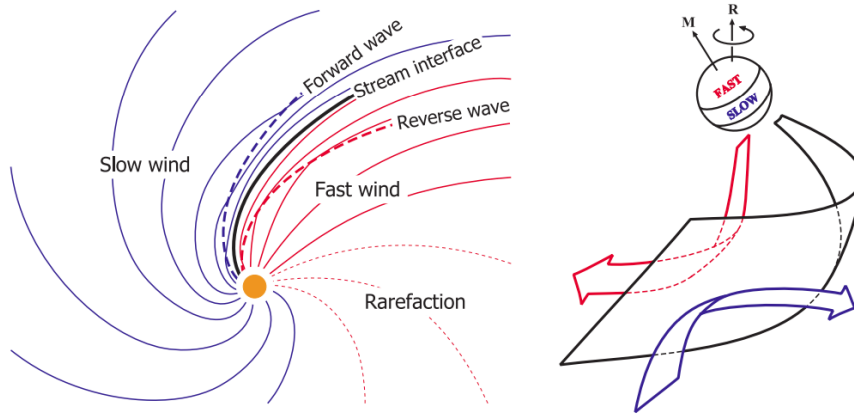
3.1 Solar wind

The existence of a matter flow coming out of the Sun was predicted for the first time by Ludwing Biermann in 1951. He observed a deviation of the comet’s tail in the opposite direction of the Sun as far as it approached the star. In 1957, Hannes Alfvén postulated that the solar wind was magnetized and that the flow of particles carried the solar magnetic field while traveling through space (BIERMANN, 1963; PARKS, 1991; KIVELSON; RUSSELL, 1995) being responsible for the comet’s tail deviation. In 1958, Eugene Parker showed that it was required the existence of the supersonic plasma flowing out of the Sun, that he called Solar Wind (PARKER, 1958). This is due to the fact that Sun’s photosphere and corona temperatures are approximately 6000 K, 10^6 K (KAMIDE; CHIAN, 2007), respectively, and the interplanetary medium has a temperature significantly lower than that, together with a thermal pressure much lower than the solar corona base.

The solar wind is a plasma that flows radially in the opposite direction to the Sun with speed ranging from 200 km s^{-1} up to more than 1000 km s^{-1} . The solar wind is typically classified as slow ($\approx < 450 \text{ km s}^{-1}$) and fast ($\approx > 450 \text{ km s}^{-1}$) depending on the solar activity. The slow solar wind is denser, cooler and more variable than the fast solar wind (BOTHMER; DAGLIS, 2007). The average density is 5 cm^{-3} for slow solar wind. According to Alfvén’s theorem, in a perfectly conductive fluid, the magnetic flux through any closed circuit that moves together with the fluid is constant in time (BAUMJOHANN; TREUMANN, 1997). Thus, as the solar wind is highly conductive, it carries the solar magnetic field as it propagates through the interplanetary medium. This constitutes the Interplanetary Magnetic Field (IMF). The stuck field lines rotate with the Sun and configure a spiral-shaped geometry. At the Earth’s magnetosphere standoff position, the magnetic field of the solar wind forms an angle of approximately 45° concerning the Sun-Earth line (PARKS, 1991),

as one can see on the schematic representation shown in Figure 3.1.

Figure 3.1 - The figure presents a scheme showing the interaction of the solar wind with the Earth. The left panel represents the field lines moving with the fast (slow) solar wind, in red (blue). On the right, an observer's view on Earth.



SOURCE: Adapted from Owens and Forsyth (2013).

In addition to the rotation, the Sun has a cycle of approximately 11 years, as mentioned in the previous chapter, characterized by an increase in the number of sunspots reaching a period of maximum activity through roughly two years and then reducing its activity after. Eventually, Coronal Mass Ejection (CME) related to the spots eject plasma with high density and speed. The solar wind is directly related to these variations which are the primary source of energy for physical processes in the magnetosphere (KIVELSON; RUSSELL, 1995; MOLDWIN, 2008).

3.2 Interplanetary Coronal Mass Ejections

The first observation of a Coronal Mass Ejection (CME) was made in the early 1970s. Observation made by a coronagraph onboard the Orbiting Solar Observatory 7 (OSO-7) satellite shown a phenomenon, which was described as following: changes in the coronal structure occurred on time scales ranging from minutes to a few hours, it is linked to the presence of bright white light in the field of view of the coronagraph (HOWARD et al., 2013). Mass ejections were first mentioned by Gosling et al. (1975). Other works (e.g. Fernández (2005), Mierla et al. (2010)) defined CMEs taking into account the physical processes involved, thus, enormous eruptions of magnetized plasma expelled from the Sun to the interplanetary medium, lasting in

the order of minutes up to several hours.

Coronal mass ejections originate from the complex configuration of the solar magnetic field. Often they are related to solar magnetic field lines that prompt from the solar surface, and due to solar rotation, end up releasing a large amount of plasma. This phenomena are known as reconnection. The ejected plasma conserves the topology of the magnetic field from the solar surface and propagates into the interplanetary medium.

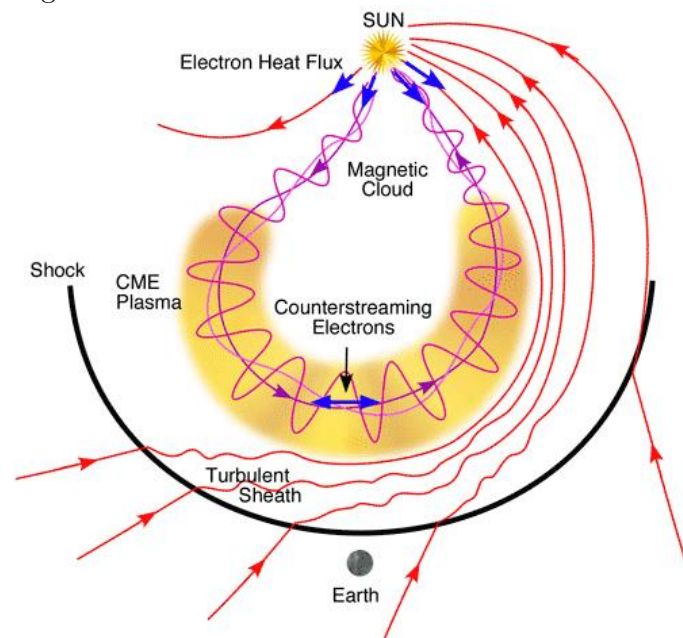
CMEs can be classified depending on their angular expansion on the field of view of a given coronagraph, from a given point of observation. Most CMEs maintain an approximately constant angular opening and so their propagation through the heliosphere is similar (SCHWENN et al., 2005). The angular widths can vary from a few degrees, for CMEs similar to a jet (called *narrow jet*), and up to 360° , for CMEs that surround the entire coronagraph disc, the so called full halo CMEs (HOWARD et al., 1982; FERNÁNDEZ, 2005; SCHWENN, 2006; VOURLIDAS et al., 2013).

There are several catalogs available online summarizing the CMEs properties such as, period of observation, speed, acceleration, angular position, among others:

- CDAW (https://cdaw.gsfc.nasa.gov/CME_list/index.html), a LASCO CME catalog produced by hand;
- CACTus (<http://sidc.oma.be/cactus/>), a catalog of CMEs from LASCO and recently from STEREO, that use unsupervised software providing information about properties of CMEs (speed, location, and frequency of occurrence)
- Multi-View CME Catalog - (MVC) (VOURLIDAS et al., 2017) (<http://solar.jhuapl.edu/Data-Products/COR-CME-Catalog.php>). In this case, the detection of kinematic properties of CMEs are done using the CORSET technique on STEREOs probes data
- List of CMEs made by Cane and Richardson (2003), Richardson and Cane (2010), (hereafter named Richardson's catalog) which has organized a list of events since 1996, taking into account the observations made by SOHO, LASCO and the ACE satellites. It considers the solar wind parameters, such as temperature, magnetic field, and the occurrence or not of interplanetary shocks, this list is constantly updated and is available at <http://www.srl.caltech.edu/ACE/ASC/DATA/level3/icmetable2.htm>

As Richardson's catalogue considers the observation of structures made by distant satellites, this list contains solar wind structures that propagate over great distances. It is possible to separate them into structures with or without the presence of a magnetic cloud. Such parameter is important to consider, among others, it is a proxy to confirm if the structure is coming towards the earths and will interact with the magnetosphere. We choosed this list because it is widely used in the literature and it covers the entire era of the Van Allen Probes. Also, the list provides the time of ICME arrival, and the start/end times of the structure.

Figure 3.2 - The figure shows a schematic representation of an ICME and its shock wave reaching the Earth.



SOURCE: Adapted from Richardson and Cane (2010).

When the CMEs propagates in the interplanetary medium, covering distances far from the field of view of the coronagraphs, they are called Interplanetary coronal mass ejections (ICMEs). The distinction between CMEs and ICMEs is mainly by the fact that the definition of CME is related to the observation in the coronagraph field of view and the ICME is the structure traveling in the interplanetary medium. At the interplanetary region, ICMEs are often characterized by twisted magnetic fields; such ICMEs are commonly referred to as magnetic clouds (RICHARDSON; CANE, 2010). Figure 3.2 shows a schematic diagram of an ICME with magnetic cloud structure reaching the Earth.

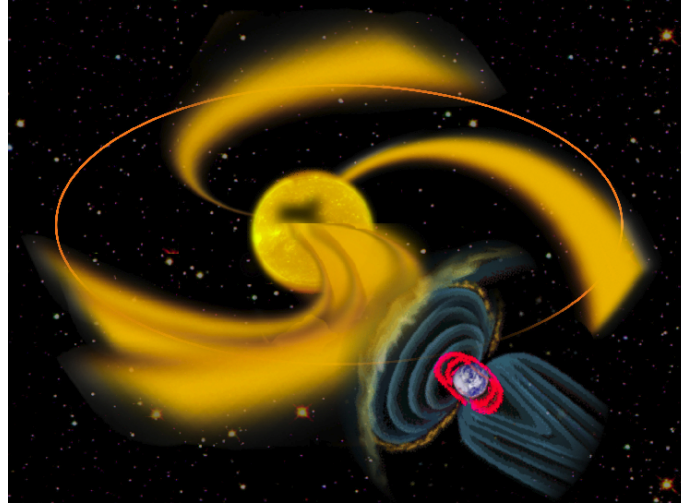
3.3 High-Speed Streams

Transient events, such as ICMEs are frequent during periods of high solar activity and through the maximum of the solar cycle. Despite the importance of these events, during the descending phase of solar activity, the solar wind flow of High-Speed Streams (HSS) is dominant during the solar-minimum activity and is responsible for conducting physical processes at the Earth's magnetosphere that last longer than those generated by ICMEs (BOROVSKY; DENTON, 2006; KAVANAGH; DENTON, 2007).

The flow velocity of solar corona particles has a solar latitudinal dependence besides the occurrence of transient events. The former was observed by Ulysses probe (PHILLIPS et al., 1995). It showed that the typical speed is higher over the poles ($\approx < 500 - 800 \text{ km s}^{-1}$), while in lower latitudes the average speeds vary between values lower than 300 km s^{-1} and 400 km s^{-1} . The fast solar wind emanates from regions less bright than the other in the corona and with magnetic field lines that close far in the interplanetary medium. This solar structure are named Coronal Holes (CH), they can be periodically prompted at solar disc high latitudes and to be transported to medium and low solar latitudes as the solar cycle evolves to the minimum. During the declining solar activity phase, the Sun is relatively more stable, than CH can last for several months and recurrent interact with the Earth's magnetosphere with a period of around 27 days, according to the solar rotation period (TSURUTANI et al., 2006; MORLEY et al., 2009; DENTON et al., 2008). Figure 3.3 shows, in an artistic representation of the origin of HSS events in the solar and the interaction with the Earth's magnetosphere.

Streams of high speed associated with coronal holes push low-speed streams (associated with the heliospheric current sheet), generating a compression region between them. The compressed region is named as corotating interaction regions (CIRs), another large-scale solar wind disturbance called, first discovered by Smith and Wolfe (1976). The first observation of shock conducted by the CIR was discussed by Tsurutani et al. (1982), who was the first to show that shocks can accelerate particles. If the relative speed between the fast and slow flows is higher than the local magnetosonic speed, then shocks can also be triggered by the CIRs.

Figure 3.3 - Artistic representation of the interaction between a rapid flow of the solar wind and the Earth's magnetosphere. The HSS is in yellow, and the coronal holes on the solar surface are the darkest parts of the solar corona, the Earth's magnetic field is represented in blue, the radiation belts in red.



SOURCE: Adapted from Gibson et al. (2009).

The HSS plasma parameters has typical characteristics at distances close to Earth. The parameters which characterize HSS are:

- the increase in the speed of the solar wind, going from "slow" to "fast" and lasting through a few days;
- the increase in the plasma density at the arrival of the structure, followed by very slow values inside the structure;
- the IMF has a local maximum at the arrival of the structure, at the same time as the plasma density.

According to Bame et al. (1976), HSSs are observed as a variation in solar wind speed of at least $\approx 150 \text{ km s}^{-1}$ within five days interval. Other authors (e.g. (INTRILIGATOR, 1977; BROUSSARD et al., 1978)) describe the events as a period in which the solar wind reaches speeds between $\approx 400 \text{ km s}^{-1}$ and $\approx 500 \text{ km s}^{-1}$ on average for one day. Lindblad and Lundstedt (1981) defines an HSS event based on the difference between two periods: 3 hours at minimum speed and 3 hours at high speed. This difference should be greater than 100 km s^{-1} and last for at least two days. Later, Mavromichalaki et al. (1988) and Mavromichalaki and Vassilaki (1998)

defined an HSS as a period in which the difference between maximum speed and average speed before and after the flow front is greater than 100 km s^{-1} , lasting for at least two days.

There are some catalogs and lists available with the HSS records and their properties. At those catalogs it is possible to get the structure's arrival time at the detector. Xystouris et al. (2014) cataloged events during the solar cycle 23, using the definition of Mavromichalaki and Vassilaki (1998), identifying 710 events and comparing their characteristics with past events from previous solar cycle. Also, the Database Of Notifications, Knowledge, Information (DONKI - <https://kauai.ccmc.gsfc.nasa.gov/DONKI/>) provides such information and add the arrival at the magnetosphere and which instruments were used to detect the structures. This repository was chosen to select the events of this work, because it has data from the entire period of interest.

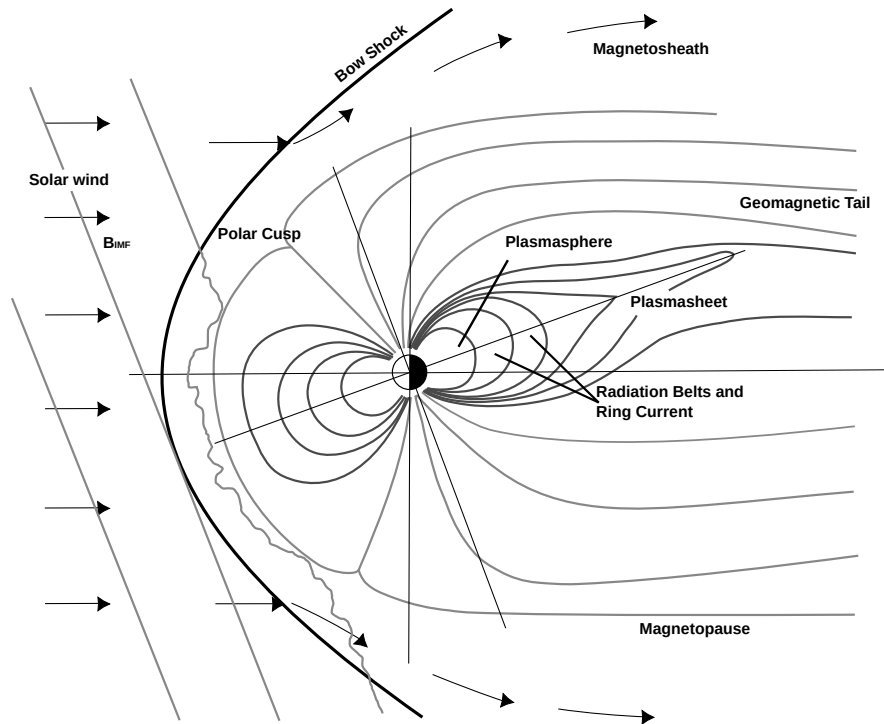
4 THE EARTH'S MAGNETOSPHERE

4.1 Main field

The origin of the magnetic field is not well defined yet. Given the structure of the Earth, with a solid metallic nucleus, surrounded by a region composed primarily by iron and nickel in a liquid state, the movement of ions present in this region is capable of originating the Earth magnetic field. The "Dynamo Theor", suggested by Joseph Larmor in 1919 (MERRILL et al., 1998), states that the magnetic field is considered the Earth's "main field" and it is characterized as a magnetic dipole slightly displaced concerning the Earth's axis of rotation.

The Earth's magnetic field has a dipole-like configuration in the vicinity of the Earth. The Earth's magnetic field presents an obstacle to the solar wind flow. The sun-earth interaction causes a difference in the configuration in the magnetosphere's outer most regions, compressing the field at the noon sector and stretching the field lines in the night portion. The propagating solar wind, when reaches the Earth's magnetic field, is supersonic and super Alfvénic, it causes a shock wave (bow shock) at the nose of the magnetosphere. This shock region is controlled by the pressure balance between the solar wind dynamic pressure and the magnetic pressure exerted inside de magnetosphere, this balance determine the region also known as magnetopause (SCHUNK; NAGY, 2009). The force exerted by solar wind in the magnetosheath is basically the $\mathbf{J} \times \mathbf{B}$ force produced by the Chapman-Ferraro current that confines the geomagnetic field inside the magnetosphere (LOPEZ; GONZALEZ, 2017; KIVELSON; RUSSELL, 1995). As the solar wind passes through the shock wave, it is slow down and deflected around the Earth in a region called the magnetosheath, forming an extensive tail, the magnetotail. The thin layer that separates the magnetized plasma from the solar wind in the magnetic sheath of the Earth's magnetic field is known . The magnetosphere regions are outlined in Figure 4.1.

Figure 4.1 - A cross-section representation of the IMF and magnetosphere intersection region (bow shock) and the main regions at magnetosphere



SOURCE: Adapted from Moldwin (2008).

When the north-south solar wind magnetic field component is oriented in opposite direction to the magnetosphere, the phenomenon of reconnection may occur at magnetopause (DUNGEY, 1961; GONZALEZ; MOZER, 1974). In this situation, the solar wind magnetic field lines connect to those of the geomagnetic field, and then both environments can exchange the particles previously trapped and allows solar wind plasma to enter into Earth's magnetosphere. As the solar wind moves through the magnetosphere, the open field lines are dragged along with until they connect again in the magnetospheric tail. Once the lines are closed again, they return to the dayside via convective process, this is a cyclic processes. This process is called Dungey cycle (BAUMJOHANN; TREUMANN, 1997; KIVELSON; RUSSELL, 1995; DUNGEY, 1961).

The geomagnetic field topology is convenient to trap charged particles present in the internal magnetosphere and linked to the lines of the magnetic field. Although plasma can be found throughout the magnetosphere, there are several distinct populations, as shown in Figure 4.4. The radiation belts contain electrons and protons

trapped in oscillatory motion by the Earth's magnetic field, as will be discussed in Section 4.4.

4.2 Geomagnetic field variation

Disturbances of the geomagnetic field can occur with different periods, ranging from fractions of a second to millions of years. In general, slow variations are caused by internal phenomena of the Earth (such as the motion of the viscous fluid in the Earth's core). In contrast, rapid variations are associated with external phenomena (such as the arrival of disturbed solar wind). Generally, the geomagnetic field variations can be classified as follow:

- Secular variation, lasting for periods of more than one year;
- Daytime variation, lasting for 24 hours;
- Disturbances, when associated with geomagnetic storms and with several periods;
- Pulsations, lasting for minutes to hours, with a given period of 0.2 and 1000 seconds;
- Atmospherics variations, lasting for periods lower than 1 second.

Secular variations that are slow and continuous, related to the electrical currents that flux in the Earth's outer core. They provide essential information for a better understanding of this region of the planet. It has a time scale that reaches thousand years ago, and is given by the annual change in the total magnetic field value (MERRILL et al., 1998).

Daytime variations are related to electric current systems generated by ionospheric current. At quiet geomagnetic periods (without geomagnetic activity), it can be measured the diurnal variation. The system of currents that directly influence the diurnal variation is present in the ionospheric E layer, located between 80 and 120 km of altitude (KELLEY, 2009). Daily variation is related to the time of year, solar activity, and geomagnetic latitude.

Geomagnetic pulsations, or simply magnetic pulsations, observed on the Earth's surface, are manifestations of ultra-low frequency ¹ one hydromagnetic waves in the

¹According to the International Telecommunication Union (ITU), the frequency range of ULF

magnetosphere (DUNGEY, 1961). The frequency range of these pulsations ranges from 1 mHz to greater than 10 Hz. Waves with lower frequencies have wavelengths comparable to the size of the magnetosphere and, generally, have the highest amplitudes, reaching hundreds of nanoteslas.

The activity of the geomagnetic field can be classified employing indices, related to the:

- Sq Variation (Solar quiet): days magnetically stables;
- SD Variation (Solar Disturbed): days of more intense activity;
- Dst Variation (Storm Time Disturbance): days in which occur the so-called "geomagnetic storms."

Solar wind events, such as solar explosions, high-speed streams and coronal mass ejections, which occur in active regions present in the solar disk, if they are in the Sun-facing the Earth, can interact with Earth's magnetosphere and due to its supersonic velocity it generates a shock wave that reaches the magnetosphere. The impact of impulsive shocks on the magnetosphere can be associated with numerous types of disturbances that can be detected in situ or on the ground. The most immediate effect is an abrupt increase in the intensity of the magnetic field due to the compression of the field by shock, which generates an intensification in the Chapmann-Ferraro current. Part of the solar wind energy is transferred to the magnetosphere due to magnetic reconnection (DUNGEY, 1961; TSURUTANI et al., 1995). The excess of energy is suggest to be release in the tail and due to convection in the magnetosphere, the open field lines are reconnected across the tail neutral sheet and are carried into the inner magnetosphere leading to an intensification the ring current due to an increase of particle precipitation. These currents generate magnetic fields that overlap with the Earth's magnetic field (CAMPBELL, 2003; MENDES et al., 2005) Intense fluctuations in the geomagnetic field characterize what is known as geomagnetic disturbances (GONZALEZ et al., 1994). In medium and low latitudes, its characteristic is a decrease in the horizontal component (H) of the geomagnetic field, lasting from a few hours to a few days, which are the geomagnetic storms.

waves goes from 300 Hz up to 3 kHz. In magnetosphere and sismology studies, the frequencies varies in the range of 1 mHz to 10 mHz (SAITO, 1969; JACOBS, 1991; PILIPENKO, 1990; MOLCHANOV et al., 2003))

4.3 Waves in the magnetosphere

The Earth's magnetosphere is a region with a plasma of different temperatures immersed in a magnetic field. The waves in this region refer to small disturbances in a magnetized plasma, which can be stationary or propagate as impulses. Waves are time-dependent phenomena that involve electron and ion dynamics. Considering a wave generated by the pressure variation exerted by the solar wind, this takes away the balance configuration between magnetic and dynamic pressure, and the deformation in the fluid element will propagate in the Alfvén waveform (PARKS, 1991).

At the magnetosphere, it is possible to detect a wide range of wave frequencies. These waves can be classified as electromagnetic or electrostatic in terms of their propagation orientation, defined by the wave vector \mathbf{k} with respect to the electric field \mathbf{E} . An electrostatic wave has the propagation vector \mathbf{k} parallel to the electric field \mathbf{E} , while the electromagnetic waves have the vector \mathbf{k} perpendicular to the electric field \mathbf{E} (PARKS, 1991; KAMIDE; CHIAN, 2007).

Waves with frequencies between 10 mHz 0.1 Hz are often observed at ground and space observatories. This range of frequencies extends from to the resonance of the magnetospheric cavity, up to higher the cyclotron frequency of the ions. This interval is subdivided into three other bands, which are the low ($1 \leq f \leq 10$ mHz), medium ($10 \leq f \leq 10^2$ mHz) and high ($10^2 \leq f \leq 10^4$ mHz). When observed on the ground, these signals are also called geomagnetic pulsations, while in space, they are called Ultra-low frequency (ULF) waves. Generally, geomagnetic pulsations can be interpreted as the manifestation of ULF waves on the ground, but ULF waves do not always generate pulsations (SAMSON, 1991; WOODROFFE, 2010).

In 1958, the International Year of Geophysics, the study of waves in the magnetohydrodynamic theory (MHD), had a significant boost. The first morphology of magnetic pulsations was established (SAITO, 1969; JACOBS, 1991). The fact led the pulsation classification by IAGA to be divided into two categories according to their regularity and the period of variations. The pulsations with a very well defined spectral peak were classified as continuous pulsations (Pc), while those involving a broad spectral range were classified as irregular pulsations (Pi). Within each group, the heartbeats are divided according to the period and frequency.

This classification was created since little was known about the mechanisms for generating these signals. Although this classification is still widely used, the scheme

has been modified over the years, seeking to take into account the physical processes and mechanisms of pulsations source. The pulsations with prolonged periods are interpreted as MHD waves, while those of short periods are related to ions-cyclotron waves that propagate in the magnetosphere. The pulsations were then divided into three bands of different frequencies: low frequency (1 – 10 Hz), medium frequency (10 – 100 mHz) and high frequency (0,1 – 10 Hz), and in two types of wave packets: continuous and impulsive (Table 4.1) (SAMSON, 1991; GUBBINS; HERRERO-BERVERA, 2007).

Table 4.1 - Classification scheme developed by IAGA in 1964.

Class	Period (s)	Frequency	Sources
Pc1	0.2 – 5	High:	Cyclotron instabilities
Pc2	5 – 10	0.1 – 10 Hz	in the magnetosphere
Pc3	10 – 45	Medium: 10 – 100 mHz	Proton cyclotron instabilities in the solar wind; Kelvin-Helmholtz instability.
Pc4	45 – 150	Low: 1 – 10 mHz	Kelvin-Helmholtz instability; Drift mirror instability;
Pc5	150 – 600		Resonance.
Pi1	1 – 40		Field aligned currents instabilities.
Pi2	40 – 150		Abrupt changes in the geomagnetic tail; Flux transfer events.

The pulsations were classified morphologically by the IAGA in 1958 according to their waveform, continuous (Pc) or irregular (Pi), and subdivided according to frequency. In 1964 they were classified according to the generation mechanisms as well.

SOURCE: Samson (1991), Villante (2007).

The magnetospheric ULF waves can be Alfvén modes (propagating along the magnetic field) or fast compressive waves (propagating along or through the magnetic field) (KAMIDE; CHIAN, 2007). Although the two wave modes can be coupled, they generally occur in different parts of the magnetosphere. The most straightforward description of the generation of ultra-low frequency waves relies on the magnetopause disturbances driven by the solar wind, which in turn, conduct waves that rapidly propagate towards the Earth. The solar wind and the magnetosphere conditions directly influence the occurrence and characteristics of the pulsations. Magnetic latitude and longitude also change the morphological and physical properties of the

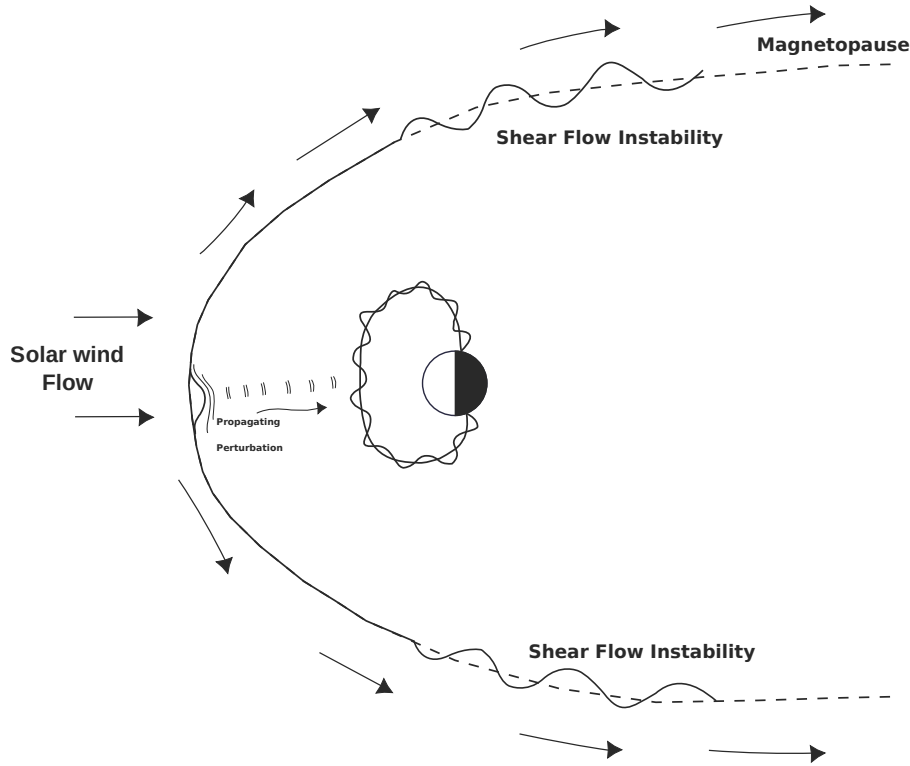
pulsations. The location of the regions of interest is generally given in terms of geomagnetic latitude or the L parameter. The McIlwain L parameter (MCILWAIN, 1961) is the distance from the center of the Earth to the magnetic line, in the equatorial plane, given in terrestrial radii. A parameter related to the latitude invariant $\Lambda = \cos^2(1/L)$, which is the latitude at which the field line intersects the Earth's surface (KIVELSON; RUSSELL, 1995; KAMIDE; CHIAN, 2007).

4.3.1 Generation mechanisms of ULF waves

ULF waves in magnetosphere can be generated both by internal processes and by interaction with the solar wind. Dungey (1967) proposed that standing waves along magnetic field lines can generate oscillation that are called geomagnetic pulsations. Besides, upstream waves are considered an important external source of medium frequency pulsations. They are generated by particles reflected from the shock wave along the lines of the interplanetary magnetic field (IMF). High-frequency continuous pulsations are believed to be generated by ion-cyclotron instabilities that occur in the magnetosphere (KIVELSON; RUSSELL, 1995; VILLANTE, 2007).

Waves with a lower frequency bands are also excited in the contours of the magnetopause in response to the shear velocity (CLAUDEPIERRE et al., 2008) or fluctuations in solar wind dynamic pressure (UKHORSKIY et al., 2006; CLAUDEPIERRE et al., 2009a). They can also be excited by natural instabilities in the magnetospheric plasma (THORNE, 2010). The characteristics of the wave spectrum are used to analyze its occurrence, intensity and to determine the radial diffusion coefficients (BRAUTIGAM et al., 2005). Field line resonant waves are a particular class of the ULF variations. In this case, the waveform is quasisinusoidal, it persists for long periods and is considered continuous. They may be associated with the constant presence of Alfvén waves in the geomagnetic field lines. In the toroidal mode of this theory, the magnetospheric cavity oscillates coherently with disturbances of the azimuth direction. Toroidal waves have been associated with an electric field induced in the radial direction. The mode of poloidal oscillation (limited by the southern plane) is characterized by magnetic compression disturbances and induced electric field in the azimuth direction (HUGHES, 1994). Figure 4.2 shows an example of disturbances generated by Kelvin-Helmholtz instabilities and due to a disturbance that compresses magnetopause and spreads towards Earth.

Figure 4.2 - Scheme exemplifying shear disturbances at the magnetopause generating Kelvin-Helmholtz instability and a magnetopause disturbance that compresses the plasma, generating waves that propagate towards the Earth. These modes can couple with the dipole field and generate resonances that can be recorded on the ground.



SOURCE: Production of the author.

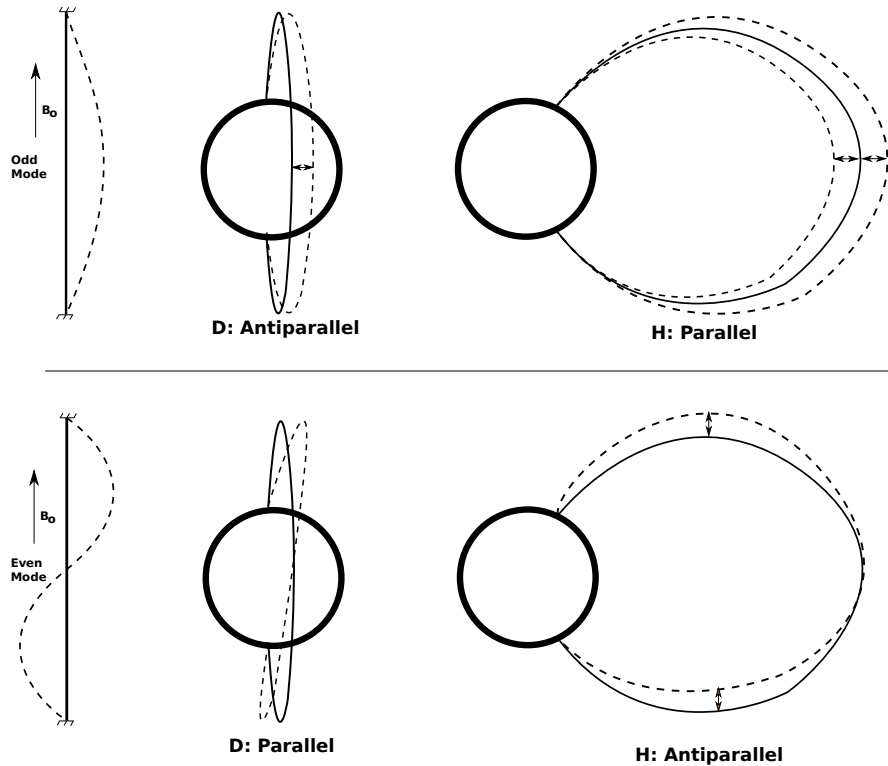
The focus of this work is related to waves generated by processes of interaction between the magnetosphere and the solar wind. These mechanisms are generally associated with lower frequencies within the spectrum of these waves (MCPHERRON, 2005). The disturbances of magnetopause caused by the solar wind interaction and on a time scale corresponding to the ULF frequencies compress the magnetospheric magnetic field, generating waves that propagate inward. Such disturbances can have sources related to global or local mechanisms. The interaction of solar wind and the magnetosphere result in contractions and expansions in magnetosphere as a direct influence of regions with high density and rarefaction in the solar wind, or changes in the average magnetic field of the magnetospheric region. These disturbances, together with macro-scale fluid instabilities, such as Kelvin-Helmholtz or Rayleigh-Taylor instabilities, can contribute to the generation of ULF waves over a large extent of the Earth's magnetopause (BAUMJOHANN; TREUMANN, 1997; MCPHERRON, 2005;

TAKAHASHI, 2016). Considering a local scale, ULF waves have variations in the magnetic sheath, generated by the configuration of the solar wind, together with positive and negative pressure pulses originated by small instabilities in the shock wave and magnetic sheath (MCPHERRON, 2005; TAKAHASHI, 2016).

4.3.2 ULF waves propagation in the magnetosphere

The external waves generated at magnetopause are strongly transformed by magnetospheric processes. In the static representation shown in Figure 4.2, fast mode waves generated by the magnetopause disturbances propagate inward and engage the dipolar field line. In turn, this drives the Alfvén waves that travel along the magnetic field. They can become standing waves if the length of the field line matches the frequency of the driving wave. In this simple description, the resonances of the field line can be poloidal (that is, radial oscillations of a magnetic field line) or toroidal (azimuthal oscillations). An example of each type of resonance is shown in Figure 4.3. In practice, most field line oscillations have both poloidal and toroidal components and the wave quickly does not fully fit the field line.

Figure 4.3 - Scheme exemplifying shear disturbances in the magnetopause generating Kelvin-Helmholtz instability and a magnetopause disturbance that compresses the plasma, generating waves that propagate towards the Earth. These modes can couple with the dipole field and generate resonances that can be recorded on the ground.



SOURCE: Production of the author.

Other types of standing waves are also possible in the magnetosphere, for example, fast standing waves between the magnetopause and the plasmasphere, known as resonances of the magnetospheric cavity. However, as the magnetosphere is not a true dipole, the resonance effect of the cavity acts as a waveguide, conducting any resonances to the tail, while the reflectivity of the magnetopause varies between the nose and the flanks (MANN et al., 1999).

The waves generated at the border are attenuated as they propagate inward. As the density profile varies considerably between the magnetopause and the ionosphere, the Alfvén speed also varies. When there is a change in density at the edge of the plasma break, the radial profile of Alfvén speed (and therefore the frequency of rotation - the frequency of the wave in which the waves are reflected) decreases markedly, allowing the existence of standing waves between the ionosphere and plasmasphere.

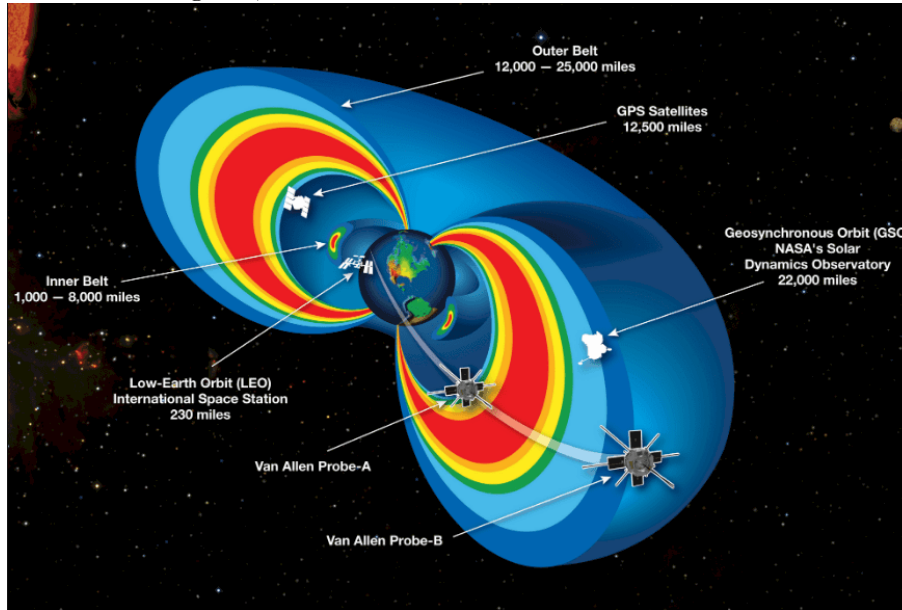
The variable nature of the plasmasphere population and the location of the plasma-pause (MOLDWIN et al., 2002) means that the density profile is constantly changing, as well as the ability of the magnetosphere to withstand the oscillation of standing waves.

4.4 Van Allen radiation belts

The Earth's radiation belts stand in the inner magnetosphere and are characterized by magnetic field configuration that traps charged energetic particles. These particles can be linked to the ring current or radiation belts; often higher energy particles are considered to belong to the radiation belts, although the energy level are related to physical processes observed in the magnetosphere and they need to be better understood (KIVELSON; RUSSELL, 1995). Cayton et al. (1989) separates the particles from the belts as being electrons with energies greater than 0.5 MeV, the electron rest mass, as they can be considered relativistic. Considering physical processes in the variation of electrons by waves in the magnetosphere, they dominate the acceleration of electrons with energies lower than 500 keV and losses occur in dozens of energies up to a few hundreds of keV (GLAUERT et al., 2014). For this reason Glauert et al. (2014) considers the lower limit to be a lower energy limit in the radiation belts, reaching up to dozens of MeV which it is the upper limit of the energy range.

In a classical view the belts are located in two separated regions. The inner belt is located between approximately 1 and 3 terrestrial radii. It is predominantly proton-populated, with energies between 100 keV and a few hundred MeV. The external belt is located approximately between $\sim 3,5$ to $6,5$ terrestrial radii. It is composed mainly of electrons with energies between dozens of KeV to a few tens of MeV. In a more realistic view, we understand the belt region as a statistically distribution of particle density, with two higher particle density regions: a highly variable external belt, located between $L \approx 3 - 7 R_E$, with a predominance of electrons with energies reaching up to dozens of MeV and a lower L-shell inner belt, consisting mainly of protons. Figure 4.4 presents an artistic representation of the radiation belts and the orbits of the Van Allen probes (BOTHMER; DAGLIS, 2007; GLAUERT et al., 2014).

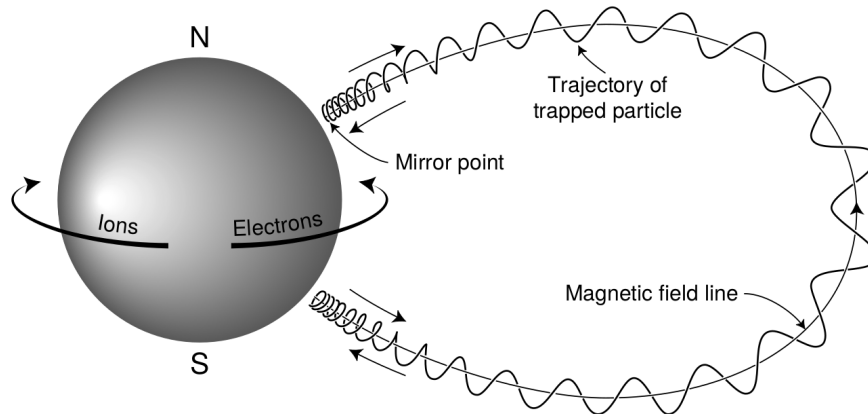
Figure 4.4 - Artistic visualization of radiation belts. The trapped particles form two toroidal regions, called Van Allen Radiation Belts



SOURCE: NASA (2007). Available in https://www.nasa.gov/mission_pages/sunearth/news/gallery/20130228-radiationbelts.html. Access in: May 6, 2020.

The particles in these regions move immersed in the Earth's magnetic field and, consequently, are governed by the Lorentz force, describing three movements: gyromotion, in which the particles rotate around the field line; drift motion when particles gradient drive around the Earth and mirroring movement, which causes the particles to move in a spiral around the field lines from one pole to another. When the charged particles approach the polar regions, where the density of field lines is larger and the field is more intense, they slow down until change direction, and return to the other hemisphere and so on (BAUMJOHANN; TREUMANN, 1997). Figure 4.5 illustrates the three types of movement.

Figure 4.5 - Trajectory of particles trapped in the geomagnetic field lines.



SOURCE: Adapted from Baumjohann and Treumann (1997).

The processes involving the dynamics of the belts are still not completely understood, the population of particles is determined by a complicated balance between competing processes, which can increase or decrease the energy of the particles; inject or remove particles from the region and is directly linked to solar activity acting on the magnetosphere (REEVES et al., 2003).

Studies involving particle dynamics are linked to processes of transport, acceleration and loss in the belts. The movements of particles in these regions are best described in terms of adiabatic invariants, which are physical parameters conserved during the performance of three periodic movements characteristic of particles trapped in the Earth's magnetic field. Each of the three movements has a characteristic time to be performed, from milliseconds (gyromotion) to minutes (drift) and are associated with an adiabatic invariant (NORTHROP, 1963; ROEDERER; ZHANG, 2014; SCHULZ; LANZEROTTI, 2012). Most of the phenomena of interest are related to the violation of one or more of the invariants. The processes are moderated by a wide range of waves with different time and space scales. Usually, each frequency range of these waves is associated with a periodic movement of the particles and thus they tend to violate one of the adiabatic invariants associated with such time scale (SCHULZ; LANZEROTTI, 2012).

The first adiabatic invariant, μ , is defined by the movement of the particle in the field line:

$$\mu = \frac{mv_{\perp}^2}{2B} = \frac{p_{\perp}^2}{2m_o B}, \quad (4.1)$$

where, p_{\perp} is the moment perpendicular to the magnetic field B , and m_o is the resting mass of the particle. Thus, μ is constant in the cyclotron movement since changes in the magnetic field are slower than the particle's cyclotron period, and while the cyclotron radius is much smaller than the curvature radius of the field line.

As the particles rotate around the magnetic field lines, due to the intensity gradient of the dipole magnetic field, the particle's gyro center also changes. The equation 4.1 can be written as,

$$\mu = \frac{mv^2 \sin^2 \alpha}{2B}. \quad (4.2)$$

The magnetic moment is invariant and only the *pitch angle*, or angle of inclination of the particle's rotation, can vary when the magnetic field intensifies or weakens along the path (BAUMJOHANN; TREUMANN, 1997). As the particle moves to the more intense field regions, the *pitch angle* increases to keep the magnetic moment constant. Once the particle reaches the mirroring point (*pitch angle* $\approx 90^\circ$), it will change its direction and return to the opposite mirror point on the field line in the other hemisphere. The second adiabatic invariant, J , it is defined, therefore, by the periodic mirroring movement of a particle trapped between two conjugated mirroring points on a field line.

$$J = \oint p_{\parallel} ds = 2 \int mv_{\parallel} ds, \quad (4.3)$$

where p_{\parallel} is the moment of the particle parallel to the field line. J is invariant as long as the magnetic field varies over a much larger time scale than the mirroring period.

The third invariant, ϕ , is given by the total flux in the drift path around the Earth, which in turn is an effect of the gradient curvature of the dipole magnetic field,

$$\phi = \oint \mathbf{B} \cdot d\mathbf{s}. \quad (4.4)$$

The total flux in the drift path is invariant as long as the frequencies of the magnetic

variations disturbing the particle are much less than the drift frequency ω_d . The drift movement, in which ions move in one direction and electrons in the other, generates an electric current system known as ring current.

One way to represent the data using the third invariant is the parameter L^* , or *L – star* (ROEDERER, 1970). L^* is the radial distance (in earth radii) of the equatorial points of a magnetospheric shell in which the particles would be found, if all adiabatically (slowly) non-dipolar disturbances of the magnetic field were turned off. The invariant can be defined as $L^* = -2\pi k_0 / \phi R_E$, where k_0 e R_E are the the Earth’s magnetic dipole and the Earth’s radius. This parameter is easier to use due to the asymmetry of the geomagnetic field (ROEDERER; ZHANG, 2014).

4.4.1 ULF wave-particle interaction

Adiabatic invariants are constant in systems with slow changes. However, during interactions between solar wind structures and the Earth’s magnetosphere, adiabatic invariants can be violated and the belt dynamics become highly complex, decreasing (*dropout*) or increasing (*re-formation*) the electron flux (BORTNIK J; THORNE, 2007; ARTEMYEV et al., 2013; THORNE et al., 2013; BAKER et al., 2014a; ALVES et al., 2016). Solar structures that generate intense and extreme storms, such as ICMEs, are more frequent in periods of high solar activity, while the fast beams of the solar wind (HSS) are capable of producing weak and moderate geomagnetic activity, being more geoeffective in the descending phase of the solar activity cycle (GONZALEZ et al., 1994; TSURUTANI et al., 1995; ECHER et al., 2011). Considering that the charged particles are subject to geomagnetic disturbances with time scales of the order of the motion constants, it is important to identify which adiabatic invariants are violated during the geomagnetic storm process.

The violation of one or more adiabatic invariants can lead to the occurrence of several important dynamic processes, which are capable of altering the particle flux density in the external radiation belt (ELKINGTON et al., 1999; ELKINGTON, 2006). As an example, there is an interaction between waves and particles. Specifically, the interaction between ULF waves and the charged particles, can violate the third adiabatic invariant, since ULF waves have periods comparable to the drift movement of electrons in the belt (GREEN; KIVELSON, 2001; NAKAMURA et al., 2002; MANN et al., 2004).

Liu et al. (1999) proposed an acceleration mechanism that involves interaction with ULF and spreading of pitch angle via interaction with whistler waves. In this process,

ULF waves offer energy through the term $E \cdot v_d$ of the equation

$$\frac{dW}{dt} = q\mathbf{E} \cdot \mathbf{v}_d + \mu \frac{\partial B}{\partial t} \quad (4.5)$$

where, q is the particle's charge, E is the background electric field, \mathbf{v}_d is the drift velocity and μ is the invariante associated to the magnetic momentum (SOUTHWOOD; KIVELSON, 1981).

This equation represents the energy changes of an electron conserving the first adiabatic invariant. Summers and Ma (2000) suggested an alternative mechanism for acceleration via interaction with ULF, including the spreading of *pitch angle* as a fundamental element of the interaction, which is a resonant interaction of the Fermi acceleration type. Depending on the geomagnetic conditions, this mechanism can accelerate electrons from keV energies to MeV in a few hours (SUMMERS; MA, 2000; ELKINGTON, 2006).

Hudson et al. (1999) report a rapid increase in the flux of relativistic electrons together with the occurrence of large-scale monochromatic ULF waves with predominant toroidal polarization. Elkington (2006) shows that the particles exchange energy with the ULF waves, mainly with the movement in the azimuthal direction, at frequencies comparable to particle drift. Thus, the interaction with the waves occurs mainly with the azimuthal electric field of the poloidal polarization mode. This interaction occurs through a mechanism called *drift-ressonance*, or resonance with the drift of the particle. For an interaction with the azimuth electric field in a symmetric dipole the resonance condition is given by:

$$\omega = m\omega_d, \quad (4.6)$$

where m and ω are the azimuthal wave number and wave frequency, respectively, and ω_d is the particle drift frequency. This mechanism can accelerate the particles through stochastic interactions, that transports the particles trough L-shell values. Elkington et al. (1999) also shows that the particles can interact and gain energy interacting with the toroidal mode also, that are due to the asymmetry between the magnetosphere's noon and midnight sectors. In that case, the resonance is expressed by:

$$\omega = (m \pm 1)\omega_d. \quad (4.7)$$

This mechanism acts in the movement described by the third adiabatic invariant. This interaction can cause electron radial diffusion in the belt, the distribution of particles under diffusion is given by the radial diffusion equation:

$$\frac{\partial f}{\partial t} = L^2 \frac{\partial}{\partial L} \left[\frac{D_{LL}}{L^2} \frac{\partial f}{\partial L} \right] - \frac{PhSD}{\tau}, \quad (4.8)$$

where $PhSD$ is the average density of the phase space over all phase angles. τ is the characteristic lifetime of the particle. The radial diffusion coefficient D_{LL} describes the average radial transport due to wave disturbances.

In radial diffusion models, the effects of ULF waves are described by the diffusion coefficients, D_{LL} . Several approaches have been studied to derive the radial diffusion coefficients caused by the interaction with ULF waves. Works such as from Brautigam and Albert (2000) derived the coefficients by separating them into electrostatic and electromagnetic components. The calculation for the electrostatic component is made assuming a linear relationship between the electric field and the geomagnetic index Kp , while the D_{LL}^B is done by combining *in situ* along with data on the ground measurements from the power spectrum density (PSD) of magnetic field measurement. Brautigam et al. (2005) developed an analytical expression for D_{LL}^E that depends on Kp and L and showed that the electromagnetic component of Brautigam and Albert (2000) is dominant over the electrostatic component.

Analytical equations for D_{LL}^E as function of Kp or solar wind speed were also derived by Ozeke et al. (2012), based on 15 years of ground data magnetometer and for different values of L mapped to the equatorial plane. The coefficients for the compressional magnetic field were derived with 10 years of data from satellites such as the Geostationary Operational Environmental Satellites (GOES), together with the Active Magnetospheric Particle Tracer Explorer (AMPTE) and showed that it is the coefficient related to the electric field that dominates over the magnetic. However, these equations are difficult to implement in numerical models. Ozeke et al. (2014) presented simpler analytical expressions for the radial diffusion coefficients in the belts, also as a function of Kp and L , which can be easily incorporated into radial transport models in radiation belts.

5 INSTRUMENTS, DATA AND ANALYSES TOOLS

In this chapter we present, the data and the instrumentation used, also the methodology applied throughout the development of the thesis . The first part of methodology refers to the selection criteria for the events of interest. The second part refers to data processing techniques regarding the identification of the most varied phenomena that occur in the outer radiation belt, such as, for example, the electron flux variability and the magnetohydrodynamic wave activity.

5.1 Instrumentation

The period defined for the study of this thesis refers to the same period of reliability of the Van Allen mission data, which was estimated by the Van Allen mission itself before the launch of the twin probes (October, 2012 to December, 2017). Therefore, for the period defined above, data from several instruments installed on the ground and onboard different satellites are used, covering at least three distinct regions of the Solar-Terrestrial environment, as described below:

(i) Interplanetary data and solar wind: Magnetic Field Experiment instruments (MAG) (SMITH *et al.*, 1998) and Solar Wind Electron, Proton, and Alpha Monitor (SWEPAM) (MCCOMAS *et al.*, 1998) onboard Advanced Composition Explorer satellite (ACE) (STONE *et al.*, 1998), available at <https://cdaweb.gsfc.nasa.gov/> provide magnetic field data, solar wind speed (V_{sw}), dynamic pressure (ρ) and proton density (N).

Located at the Lagrangian point L1, the ACE satellite was launched on August 25, 1997, and provides data for monitoring interplanetary conditions and real-time measurements of solar wind conditions.

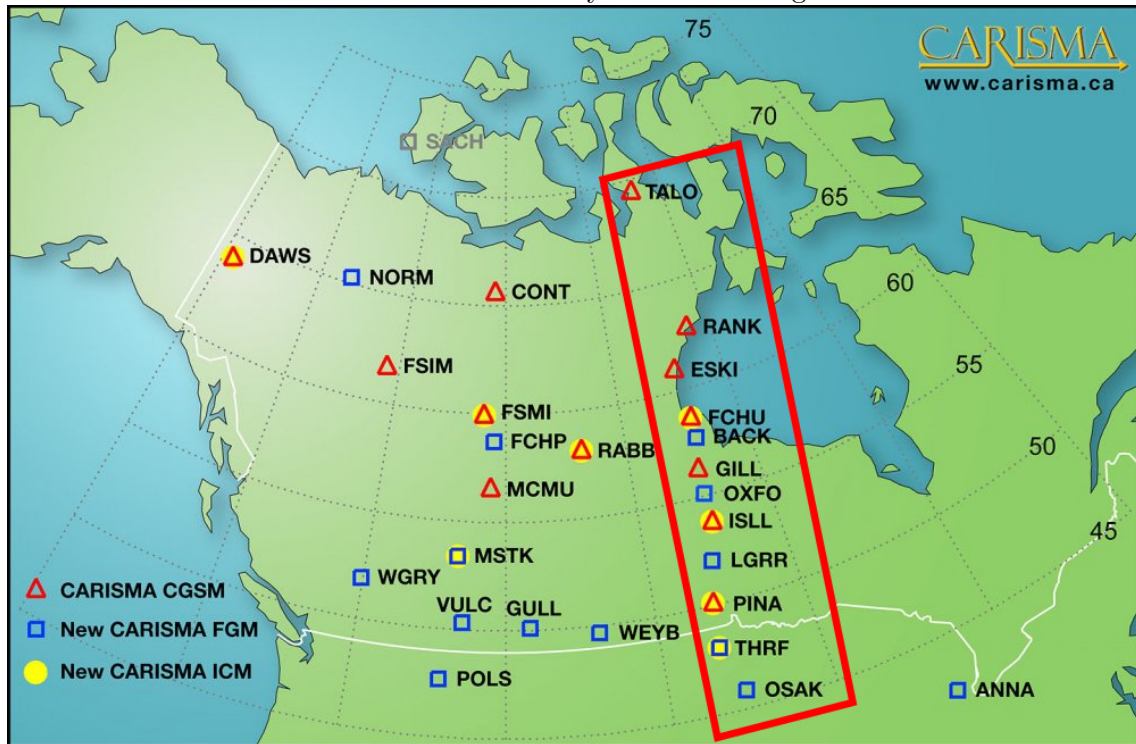
(ii) Data of the inner magnetosphere: The Relativistic Electron Proton Telescope (REPT) (BAKER *et al.*, 2014b), Magnetic Electron Ion Spectrometer (MagEIS) (BLAKE *et al.*, 2013), Electric and Magnetic Field Instrument Suite and Integrated Science (EMFISIS) (KLETZING *et al.*, 2013) and Electric Field and Waves (EFW) onboard the Van Allen Probes (MAUK *et al.*, 2013), available at https://rbsp-ect.lanl.gov/data_pub/ provide the electron flux data, magnetic field, an electric field, respectively.

The Van Allen Probes are a NASA mission dedicated mainly to the study of the behavior of radiation belts. It consists of two identical probes: Van Allen Probes A and B launched on August 30, 2012. They have practically the same orbit with an

inclination of approximately ten degrees and highly elliptical (MAUK et al., 2013), with perigee in ~ 500 km and apogee in ~ 30000 km.

(iii) Ground based geomagnetic data: surface magnetometer data from two networks located at high latitudes are used (CARISMA - Canadian Array for Real-time Investigations of Magnetic Activity (MANN et al., 2008), available at <http://www.carisma.ca/>); and from the International Monitor for Auroral Geomagnetic Effect (IMAGE) network (LUEHR et al., 1991), available at www.supermag.com. The choice of these networks is due to the location of the instruments, which make their data available according to the local time. Besides, the two networks use fluxgate magnetometers and offer data with a temporal resolution of one measure per second, which is ideal for studying the frequency range of interest in this work. In this type of magnetometer, a ferromagnetic core with high permeability of natural saturation is used to obtain the signal of the magnetic field existing in the environment. The CARISMA network has 23 sensors installed in high latitude auroral regions, from $45,871^\circ$ up to $69,540^\circ$ n Canada, and the United States; Figure 5.1 shows the spatial arrangement of the network's magnetometers. Currently, most sensors are located on the North-South meridian known as the "Churchill Line". As the measurements of the magnetic field at high latitudes are affected by disturbances in regions farther away from Earth than those made at low latitudes, this arrangement of the magnetometer allows investigating the radial propagation of events in these locations.

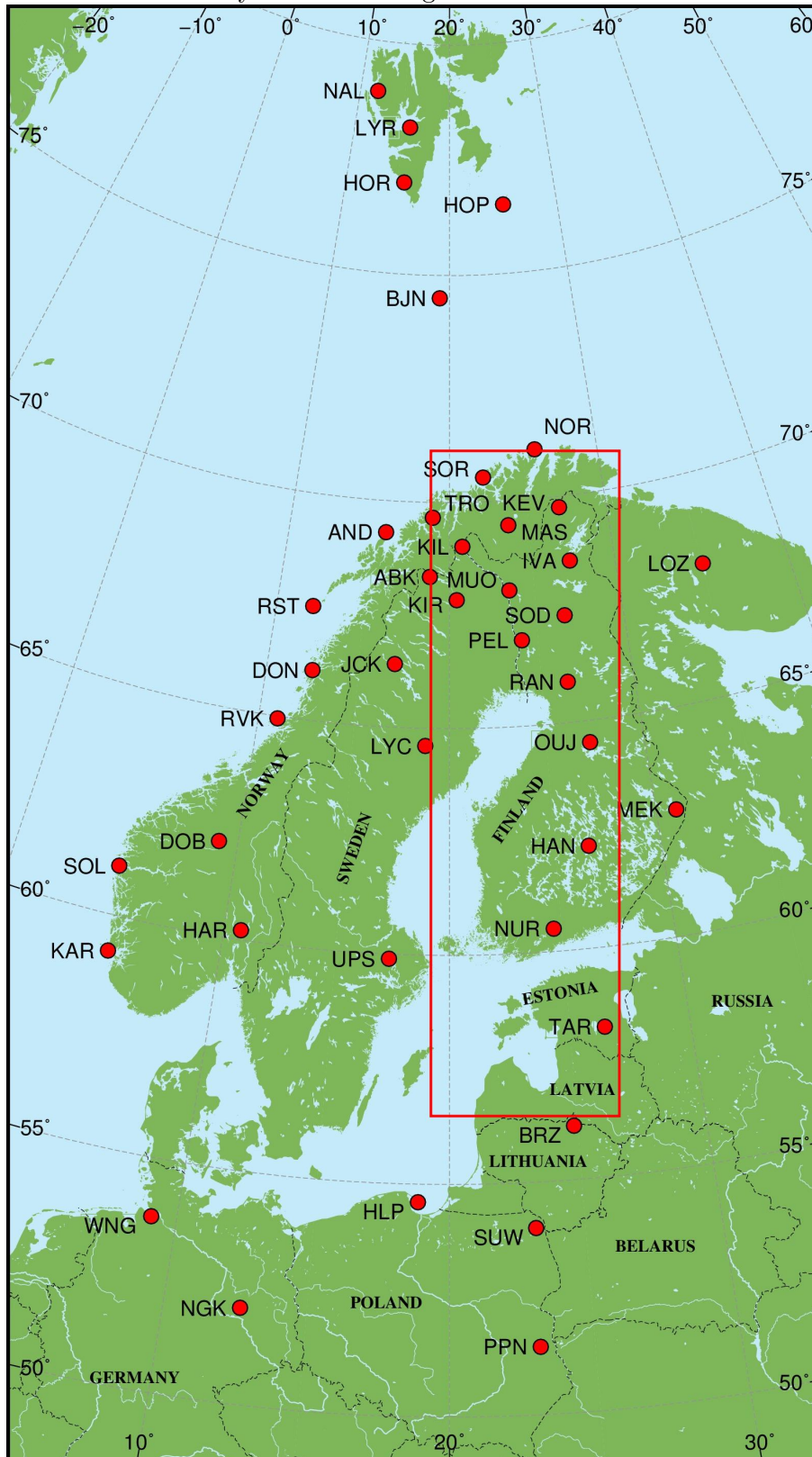
Figure 5.1 - Spatial arrangement of the CARISMA network magnetometers, with Churchill line sensors indicated by the red rectangle.



SOURCE: Adapted from CARISMA (2020). Available at <http://www.carisma.ca/station-information>. Access in: May 6, 2020.

The IMAGE network has 41 magnetic stations maintained by eight institutions in different countries: Finland, Germany, Norway, Poland, Russia, and Switzerland. The main objective of the network is to study auroral electro-jets. The instruments are installed in such a way that they cover geographic latitudes from 51 to 79. Figure 5.2 shows the layout of the IMAGE stations and the locations used in this work.

Figure 5.2 - Spatial arrangement of the IMAGE network magnetometers, with the sensors used indicated by the red rectangle.



SOURCE: Adapted from IMAGE (2018). Available at <https://space.fmi.fi/image/www/index.php?page=maps>. Access in: May 6, 2020.

In addition to this network, stations from other networks installed in the same region, longitude $\approx 110^\circ$, were used, the data of these, together with those of the IMAGE network, are made available by the SuperMag collaboration, previously mentioned. The total number of stations in this longitude is summarized in Table 5.1, it presents the geomagnetic coordinates and the parameter L for each station.

Table 5.1 - Location of the 22 magnetic stations and their geomagnetic coordinates, together with the parameter L for each station.

Station	Magnetic Longitude (degree)	Magnetic Latitude (degree)	L -shell (E_R)
SOR	106.21	67.30	6.75
TRO	102.95	66.68	6.35
KEV	109.27	66.28	6.21
KIL	130.85	65.78	5.98
ABK	101.82	65.18	5.72
IVA	108.61	65.03	5.65
MUO	105.26	64.61	5.47
KIR	102.69	64.56	5.46
SOD	107.29	63.81	5.18
PEL	104.95	63.42	5.05
OUJ	106.15	60.82	4.25
HAN	104.63	58.51	3.71
NUR	102.2	56.70	3.35
LOV	96.06	55.74	3.18
TAR	102.92	54.33	2.96
HLP	95.19	50.79	2.50
BEL	96.09	47.84	2.21
LVV	98.22	45.76	2.04
HRB	92.81	43.58	1.88
THY	92.02	42.49	1.82
SUA	99.57	40.48	1.73
ISK	101.58	35.95	1.51

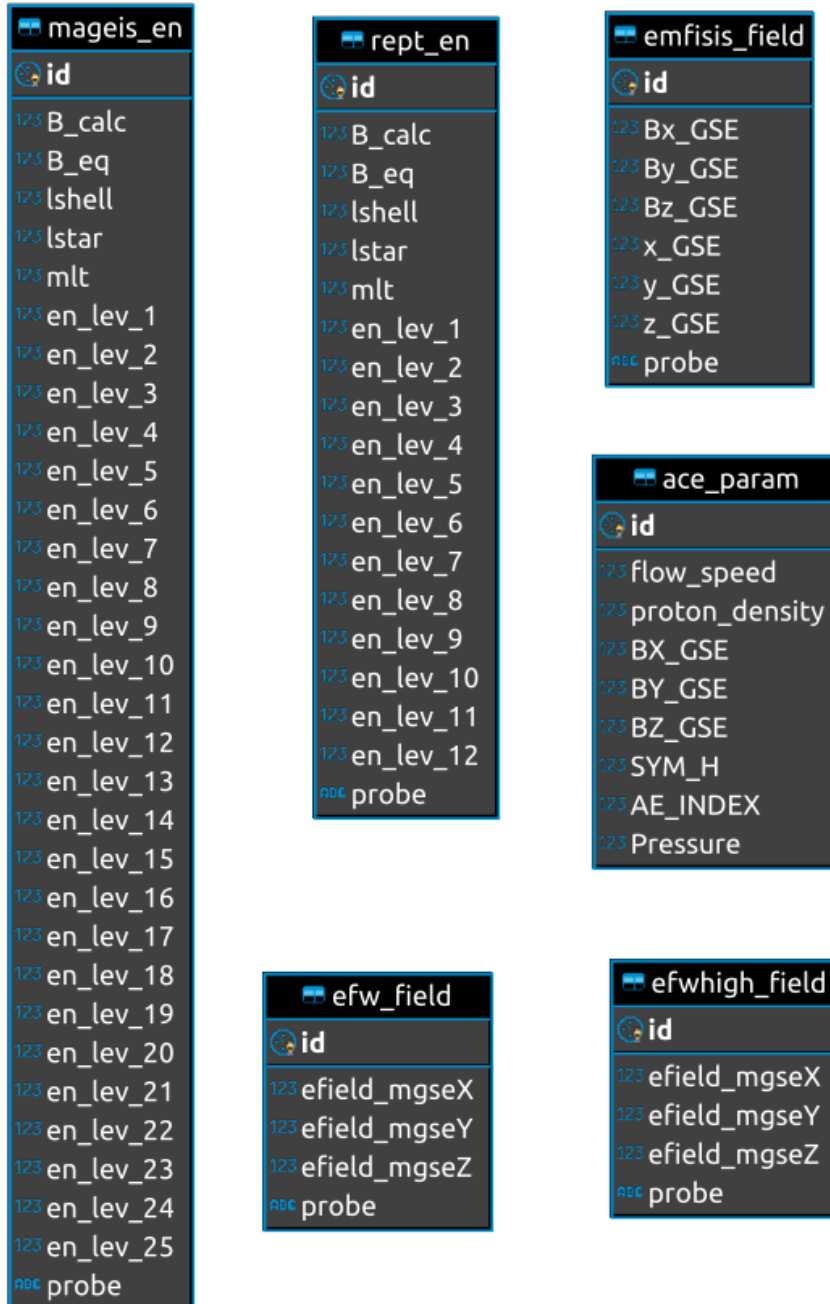
5.2 Database structure

Assuming that the database used contains different instrumentation repositories, this data was organized in a PostgreSQL database, using the Python framework. The database is structured with six tables containing the data used in this work. This structure allows to list the values of each table at the time the query is made.

The tables contain the respective data for each instrument of the Van Allen probes

and the ACE satellite. Figure 5.3 presents the structure of the data storage, where the tables *mageis_en*, *rept_en*, *emfisis_field*, *efw_field* e *efwhigh_field* store the energy flux and electric and magnetic fields data obtained by instruments MagEis, REPT, EMFISI e EFW (low and high resolution), respectively. The data is stored in such a way that, with only the date information and the probe (Van Allen-A or Van Allen-B), we can obtain the values of: L-shell, L^* , the values at all energy levels for Rept and MagEis, the electric field values recorded by the EFW, magnetic field values and coordinates provided by the instrument EMFISIS.

Figure 5.3 - Example of PostgreSQL data storage architecture. The structure and information contained in each table are presented.



SOURCE: Author production.

The use of this data storage technique avoids the need to download, as well as, to perform reading of each file separately before analysis. In addition, it provides

considerable savings in disk storage and speed in the execution of routines, also allowing the automatic creation of database backup.

5.3 Methodology

5.3.1 Event selection criteria

The selection criteria for events of interest are established based on the conditions of the interplanetary environment (ACE data), in which the different types of solar wind structures (ICME and HSS) and their respective characteristics are identified when passing through the $L1$ Lagrangian point. Structures of this type can go to Earth and cause direct and indirect impacts on the external and internal magnetosphere (outer Van Allen belt). From the identification of the referred solar wind structures, all events with occurrence of ICME and HSS directed to Earth are separated. Using this first selection of data, we identify the occurrences of concomitances between these structures and the variability in the flux of relativistic electrons in the external radiation belt, thus obtaining a new set of events for the study. For this new set of events, the identification of the magnetohydrodynamic wave activity (of the ULF type) in the radiation belt is carried out with ground-based and in-situ data, of which only the events in which the relativistic electron population increased significantly (> 1 order of magnitude).

ICME events are selected based on the list available at <http://www.srl.caltech.edu/ACE/ASC/DATA/level3/icmetable2.htm>, which is a compilation of ICME events, cataloged since 1996, based on the work of Cane and Richardson (2003), Richardson and Cane (2010). These lists provide information about the speed of the plasma, time of detection by the satellites, time of arrival at the magnetosphere and whether or not the structure has a magnetic cloud. Only cases in which the list points that there is magnetic cloud were selected, this ensures that most of the structure is interacting with the terrestrial magnetosphere and is primarily responsible for changes in the field.

HSS events are retrieved from the DONKI repository (*Database Of Notifications, Knowledge, Information*) available at <https://kauai.ccmc.gsfc.nasa.gov/DONKI/search/>. It is an environment that provides information on activities related to Space Weather, one of which is the occurrence of HSS events, also with information on speed and moments of detection and arrival in the magnetosphere. Only events recorded by the ACE satellite are selected, as the satellite is at the Lagrangian point $L1$ between Sun and Earth, this ensures that the structure has the potential

to impact the magnetosphere.

For the period under study, 140 ICME and HSS events were selected. These events presented some concordance between the variables of the solar wind structures and the variability in the flux of electrons in the outer belt, either a decrease or an increase in the flux (> 1 order of magnitude). This variability in flux was observed in relation to the radial distance in terrestrial radii, represented by the McIlwain parameter, L .

Turner et al. (2012) proposed a general definition of dropout in the flux in the external belt, which consists of events where there is a reduction in the flux of at least 50 times. This same value was used as a parameter for cases of increased flux, which is the main objective of the study. Therefore, the density of the electron flux in the energy channel of 2.10 MeV is analyzed two days before and two days after the occurrence of the event recorded in the interplanetary data. Then, only the events that showed variability in the flux from an order of magnitude in $L_{star} = 5 E_R$ are selected. This selection criterion follows the definition of electron flux variability established by Turner et al. (2012). However, the first results regarding the application of this technique are presented in Chapter 6, in which statistical analysis are also applied to better understand the variability of electron flux during occurrences of different solar wind structures detected in the interplanetary medium.

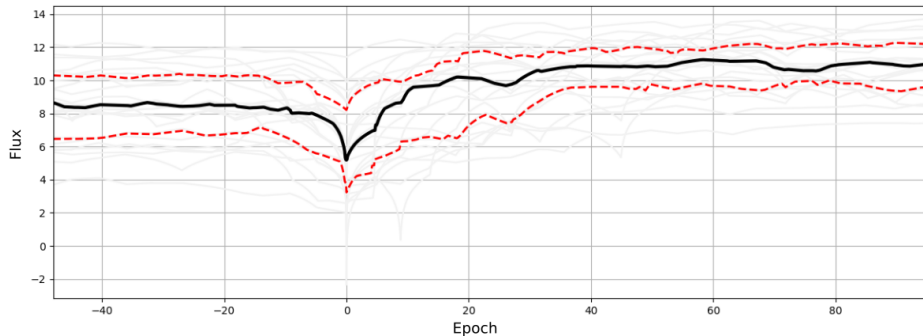
5.3.2 Superposed Epoch Analysis

The Superposed Epoch Analysis (SEA) is a widely used technique by the scientific community in the radiation belts area and the results are very significant (*e.g.* Murphy et al. (2018), Turner et al. (2019), O'Brien et al. (2001)). The SEA is a technique used to deal with the effect of noise and not significant fluctuations in the signal, in order to obtain the average behavior of the variations of a given event in the magnetosphere. The method consists of organizing the data into subcategories, depending on the characteristic to be studied, considering the same time window and a characteristic instant to synchronize them, so it is possible to evaluate the average of these subsets. This technique has been widely used in several areas, including to evaluate the relationship between solar and magnetospheric events in relation to the variation of electron flux in the radiation belts (BOROVSKY; DENTON, 2009; LI et al., 2015; KATSAVRIAS et al., 2019).

The first procedure used to apply SEA consists in determining the average variation of the electron flux for the selected events according to the type of solar structure,

as established in the event selection criteria described in the Section 5.3.1. Thus, considering the moment when the structure of the interplanetary medium reaches the Earth’s magnetosphere, a 48-hour time window is selected, centered at that moment, from which the flux information is extracted in $L^* = 5_{RE}$. From this, a time series is obtained and the zero epoch can be defined for the epoch overlap analysis (SEA). It is important to highlight that the time was defined from the minimum flux value observed in the established time window. The application of this technique is performed for all events that showed an increase in electron flux (> 1 order of magnitude) after the passage of the solar structure, as well as, for events that presented an decrease in electron flux (> 1 order of magnitude). Figure 5.4 shows an example of SEA during the occurrence of ICME, in which only the events that showed a decrease in the flux of electrons in the external radiation belt were selected, followed by rapid repopulation.

Figure 5.4 - Example of a Superposed Epoch Analysis using 40 ICME events with increased electron flux in the external radiation belt.



SOURCE: Author Production.

The scientific community generally uses the intensity of the storm as criteria to select the events and to define the zero epoch (*e.g.* Murphy et al. (2018), Turner et al. (2019)). Here we used the criteria described in Section 5.3.1, in which the interplanetary medium parameters are considered. It means that the results presented in this Section can be compared with several case studies published (*e.g.* Alves et al. (2016), Alves et al. (2017), Souza et al. (2017), Silva et al. (2019)). The statistical results obtained here also can substantiate the real impact of the different solar wind structures on the outer radiation belt flux. This method was used for flux data in

all energy ranges of the REPT and EMFISIS instrument, when it comes to spectral power, the results obtained are presented in the Chapter 6.

5.3.3 Signal analysis

A signal can be understood as the representation of a phenomenon or physical process that varies with time or space and carries information. A magnetometer is an example of an instrument that records magnetic field variations as a signal. This signal can be transcribed so that its variations can be analyzed in a convenient way. Several methods can be used to extract information from a signal. Each method has characteristics that make them more or less suitable for a particular type of analysis. The analysis of the frequency spectrum of a signal using the Fourier transform is the most common, this category includes the fast (FFT) and discrete (DFT) Fourier transforms, the windowed Fourier transform and the digital filters based on the Fourier transform. In the analysis of real data, especially in this work, the Fourier transform is an option to know the frequency content that can be extracted from the signal. It is a step towards knowing which frequencies can be filtered and analyzed. Another tool available is the analysis by wavelets which, similar to FFT, extracts information about the signal frequency spectra. However, the wavelets function analyzer, or mother wavelets, has two main parameters: a scale parameter, that extends the mother wavelet; and a translation parameter, allowing a better spatial location of these frequencies and adds the dynamic analysis capacity (BOLZAN, 2006; CASTILHO et al., 2012).

In signal analysis, we must also take into account the restrictions imposed by the instruments used. The sampling frequency of the sensor defines the maximum frequency that can be detected in the signal, following the definition of the Sampling Theorem. If a continuous function $f(t)$, sampled in a given time range Δ , is limited by frequencies between $-f_c$ e f_c , then the function is fully represented by its samples h_n , f_c is called critical frequency or *Nyquist frequency* (PRESS, 2007), expressed by

$$f_c = \frac{1}{2\Delta}. \quad (5.1)$$

When the signal is not limited between Nyquist frequency, the power spectrum outside that range is falsely transposed within the range.

Fourier Transform

The Fourier transform is a linear operation. It can be expressed in terms of a sum of sine waves, well located in frequency, but not through time. One way to represent a $h(t)$ function using the Fourier transform is:

$$H(\omega) = \int_{-\infty}^{\infty} h(t) \exp(i\omega t) dt. \quad (5.2)$$

$H(\omega)$ is a function of ω instead of t and is called the Fourier transform of $h(t)$. The Fourier transform is an operation that transforms a function in the time domain into one in the frequency domain. The inverse Fourier transform can be expressed by

$$h(t) = \frac{1}{2\pi} \int_{-\infty}^{\infty} H(\omega) \exp(-i\omega t) d\omega. \quad (5.3)$$

The total power of a signal can be calculated both in time and frequency domains. The relationship is given by the Parseval theorem

$$\int |h(t)|^2 dt = \frac{1}{2\pi} \int |H(\omega)|^2 d\omega. \quad (5.4)$$

Wavelet Analysis

The wavelet transform was introduced in the early 1980s for geophysical purposes, Alex Grossmann and Jean Morlet perfected the Fourier transform, creating what would be considered the first formalism for the continuous wavelet transform (DAUBECHIES, 1992). The theory has since been refined by Yves Meyer, Ingrid Daubechies, Stéphane Mallat, among others. As the method was developed independently in several fields, the theory is similar to several methods, from functional analysis to signal processing (HUBBARD, 1998).

The wavelet transform is a linear transformation with the property of being covariant under translation and expansion. It is similar to the Fourier windowed transform. The difference is that while the Fourier transform decomposes the signal into sines and cosines, well located in the frequency space; the wavelet transform uses functions that are located in time and frequency. This characteristic can be used in the analysis of non-stationary signals to obtain information about the frequency variations and to detect structures located in time and/or space (DOMINGUES et al., 2005). The wavelet transform of a $f(t)$ function is defined by the integral transform:

$$W(a, b) = \int_{-\infty}^{\infty} f(t) \bar{\psi}_{a,b}(t) dt \quad a > 0, \quad (5.5)$$

where:

$$\psi_{a,b}(t) = \frac{1}{\sqrt{a}} \psi \left(\frac{t-b}{a} \right), \quad (5.6)$$

To satisfy the admissibility condition, the wavelet must be an integrable function with zero mean. The reversibility of the wavelet ensures that it is possible to reconstruct exactly the original signal from the wavelet coefficients. Analyzer functions must be regular, excluding discontinuous functions. It also allows the study of local fluctuations in the signal, in addition to possible local singularities and discontinuities in the signal or its derivatives.

Whereas, in the Fourier transform, the base is very well located in frequency; in the wavelet transform, the bases are located both in the frequency domain and in the temporal domain. In fact, there is a balance between the resolution in each of the domains, respecting the Heisenberg Uncertainty Principle. The local evaluation of the signal occurs through the local behavior of the wavelet coefficients. The wavelet coefficients of a locally smooth function will be small; if the function has local variations, with very small periods, the values of the coefficients in the vicinity of these structures will be higher (SIMOES, 2011; CASTILHO et al., 2012). The ULF wave signals present in the electric and magnetic field data, recorded by the Van Allen probes, were filtered using a *Butterworth* type filter, which is based on the Fourier transform.

The ULF waves signals present in the electric and magnetic fields, measured by the Van Allen Probes were filtered using a Butterworth filter, that has in his basis the Fourier transform to extract the frequencies that will be removed.

Continuous wavelet transform

The continuous wavelet transform (*CWT*) refers to the equation 5.5 with scale and location parameters assuming continuous values. Visualization of CWT parameters is usually done by wavelet spectra or scales, which represent the energy distribution of the signal over time by its scale. (DOMINGUES et al., 2005; CASTILHO et al., 2012).

Each scale (a) is associated with a central frequency, or also called, pseudo-frequency

(ξ_a) given by the relation:

$$\xi_a = \frac{\xi_\psi}{a\Delta t}, \quad (5.7)$$

where ξ_ψ is the central frequency associated with wavelet and Δr the time interval between each signal sample (DAUBECHIES, 1992; KUMAR; FOUFOULA-GEORGIU, 1997).

Due to the redundancy of CWT, it is generally used as a first analysis of the signal content, allowing a complete characterization of the signal information. However, the computational cost is high, from the order of operations squared to the number of points in the series.

The choice of the mother wavelet is also important. A complex wavelet may be more suitable for amplitude and phase changes; whereas a real function can better show more localized structures.

Discrete wavelet transform

In the discrete wavelet transform (*DWT*) the scale and translation parameters receive discrete values. It can be redundant or not, depending on the function used, whether it is orthogonal or not. The discrete transform is expressed in terms of the wavelet coefficients d_k^j as:

$$d_k^j = 2^j \int_{-\infty}^{\infty} f(t)\psi(2^j t - k)dt. \quad (5.8)$$

The coefficients d_k^j are also called details. They express the difference between two consecutive levels of signal decomposition.

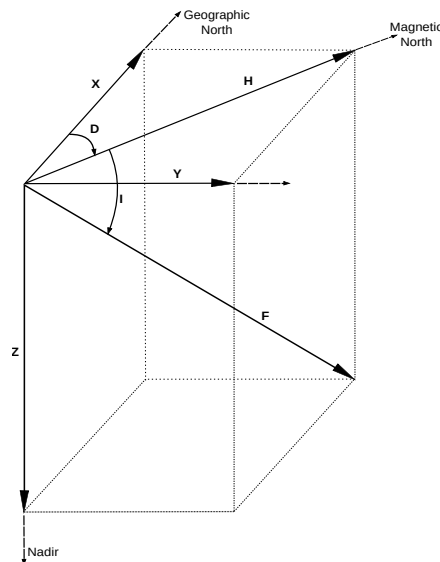
There are several ways to implement an algorithm for DWT. The best known is the Mallat or pyramidal algorithm. In this algorithm, two filters, one smooth and the other coarse, are built from the wavelet coefficients and are used to obtain the data for each scale.

The analyzes presented in the Chapter 7 were made using Wavelet and Fourier transforms to the electric and magnetic field data recorded by the Van Allen probes.

5.3.4 Ground-based instruments methodology

The terrestrial magnetic field is a vector field with full intensity \mathbf{F} which is determined based on three reference planes: a vertical plane containing the vector oriented from east to west; a southern plane that contains the vector whose orientation is north-south and a horizontal plane that contains the vector that points to the nadir. The magnetic meridian is defined as the plane containing the vector \mathbf{F} , as shown in the Figure 5.5. The intensity of the magnetic field is measured in the International System of Units (SI) in tesla (T) and in the centimeter-gram-second system (cgs) in gauss, where 10000 gauss is equal to 1 T . The magnetic field of the Earth is usually measured in nanoteslas (nT), or gamma ($1\gamma = 10^{-9}T$) (MERRILL et al., 1998).

Figure 5.5 - Vector elements of the magnetic field of the Earth.



SOURCE: Author production.

The components \mathbf{H} and \mathbf{Z} are the horizontal and vertical projections, respectively, of \mathbf{F} at the measurement location.

The component \mathbf{X} is the component of \mathbf{H} in the north-south direction and \mathbf{Y} is the component of \mathbf{H} in the east-west direction. The vectors \mathbf{X} , \mathbf{Y} and \mathbf{Z} are thus the magnetic components in the Cartesian coordinates defined by the geographic north, the geographic east and the vertical downwards, respectively.

The angle between the geographic north and the magnetic meridian is the declination D , by convention it is considered positive from the north to the geographic east, in the northern hemisphere. The magnetic inclination I , which is the angle that \mathbf{F} makes with the horizontal plane is considered positive when pointing downwards.

The mathematical relations between the magnetic components are

$$H = F \cos(I), \quad X = H \cos(D), \quad D = \arctan\left(\frac{Y}{X}\right),$$

$$Z = F \sin(I), \quad Y = H \sin(D), \quad I = \arctan\left(\frac{Z}{H}\right),$$

$$F^2 = H^2 + Z^2, \quad H^2 = X^2 + Y^2, \quad F^2 = X^2 + Y^2 + Z^2,$$

Data from both networks were used with time resolution of seconds. The data of the Carisma network are made available in a file for each day. Each file contains the measurements in the X, Y and Z coordinates of the geomagnetic field and the temporal information of the measurement: day, hour, minute and second. The MagNet network offers the data compiled in a file for each hour of measurement. The file contains the voltage measurements of the channels corresponding to the H, D and Z components of the field. This signal was then converted using the device's technical information and base values for each station, which need periodic calibration. Failed files are processed by adding null values, *i.e.* Computationally setting *NaN* (*Not a number*), in the missing moments.

These data were used to evaluate the activity of the ULF waves, in the frequency bands defined by the pulsations Pc3, Pc4 and Pc5, in the region of the external belt. This is possible due to the latitudinal arrangement of the magnetometers that reflect the disturbances that occur at a distance of up to 6 terrestrial radii. Along with the information collected on the surface, electric and magnetic field data measured in the belt region by Van Allen probes were used.

The signal of the ULF waves, in the desired frequency ranges, is extracted using a band-pass filter in the signal of the diurnal variation of the H component of the magnetic field measured on the ground. For each frequency range, the continuous wavelet transform is applied, with the Morlet analyzer wavelet, to assemble a fre-

quency spectrogram and extract the average value of the spectral power for each station as a function of latitude. So we can relate the measurements of the waves on the surface to regions in the radiation belts. With the two networks available, we have a latitudinal coverage ranging from equatorial regions, with the MagNet network, to auroral regions, with the CARISMA network.

5.3.5 Satellite data methodology

Relativistic Electrons Flux - REPT

REPT provides data on electron flux density at 12 energy levels (from 1.80 to 59.45 MeV) and in 17 values of *pitch angle* (5.3° , 15.9° , 26.5° , 37.1° , 47.6° , 58.2° , 68.8° , 79.4° , 90.0° , 100.6° , 111.2° , 121.8° , 132.4° , 142.9° , 153.5° , 164.1° , 174.7°). The mean value of the electron flux density data over all values of *pitch angle* were used, for energies from 2.10 MeV to 5.00 MeV. The flux values were interpolated with the measurements of the position of VAP-A and VAP-B in L-Shell, from $L = 2$ to $L = 6$. Thus assembling a graphical representation of the electron flux density as a function of L-Shell and time. The increase in flux is verified with a cut at $L = 5$ in the interpolation.

Electric and Magnetic Fields - EFW e EMFISIS

The EMFISIS has a magnetometer *fluxgate* which measures in three orthogonal directions, with an operating range between 0.008 and 65536 nT, and temporal resolution of up to 64 Hz (KLETZING et al., 2013). The magnetic field data came from the third level of refinement (L3) of EMFISIS, with a resolution of 1 s, in the geocentric solar magnetospheric (GSM) system. Only periods with few failures were used. The magnetic field measurements have a very large amplitude due to the orbit of the probes, when it approaches the perigee the magnetic field undergoes an abrupt increase to a point where there is only noise. This long-term variation was removed using multiresolution wavelet signal reconstruction methods, which consists of decomposing the original signal into levels of detail and approximations, and reconstructing the signal only at the highest frequencies.

The electric field data, offered by the instrument EFW, have a maximum cadence of 32 Hz and an operating range between 0.05 mV m^{-1} and 1 V m^{-1} (WYGANT et al., 2013). Electric field data is made available with a maximum resolution of 32 Hz at the second level of refinement (L2) of EFW. The temporal resolution of these data has been reduced to the same temporal resolution as the magnetic field data,

1 Hz. As the interest of the work is in the ULF waves up to a maximum frequency of 22.2 mHz (Pc3) the temporal resolution of 1 Hz, both for the surface data and for the the radiation belt data is in accordance with the Nyquist frequency for this sampling.

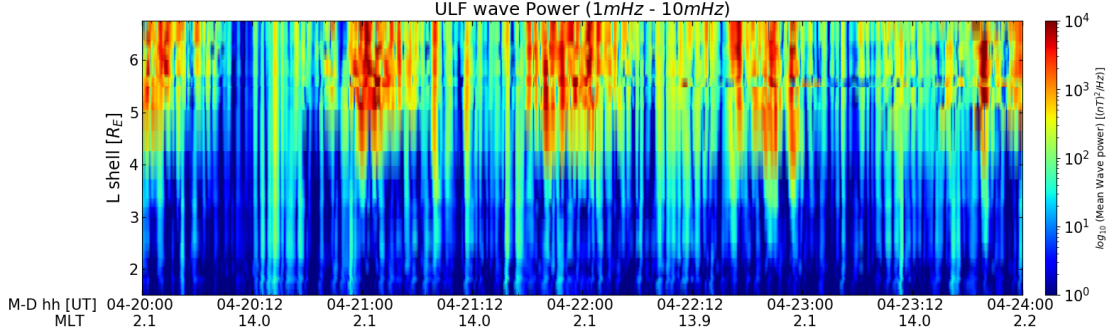
To measure the spectral density of the compressional, polyoidal and azimuthal modes, the electric and magnetic field vectors need to be rotated to the Field-aligned coordinate system: considering a point $\mathbf{s} = (x, y, z)$ in space where there is a magnetic field \mathbf{B} , the parallel direction (\parallel) is represented by $\mathbf{b} = \mathbf{B}/|\mathbf{B}|$, the azimuthal direction (ϕ) is the cross product between \mathbf{b} and the unit vector of the point $\mathbf{s}/|\mathbf{s}|$. The radial direction completes the orthogonal system being positive in the outward radial direction.

The power spectrum was made using the continuous wavelet transform with Morlet mother wavelet, for the parallel component of the magnetic field, B_{\parallel} , and for the azimuthal and radial components of the electric field, E_{ϕ} and E_r , these components are related to the compressional, poloidal and toroidal magnetic field mode, respectively.

5.4 ULF waves Power Spectrum Density - IMAGE and CARISMA

In this method of analysis, we seek to evaluate the temporal and spatial distribution of ULF wave power (frequencies between 1 and 10 mHz) according to the radial distance, using magnetometers installed in magnetic stations on the ground. Those measurements are provided by the SuperMag collaboration (GJERLOEV, 2009). An example of this visualization is shown in Figure 5.6, the same methodology was used in Chapter 7. The choice of stations must take into account the longitude, which cannot vary much, that is, all magnetometers must be in the same longitudinal range and their latitude must correspond to values in L within the desired altitude, in this case, Van Allen's radiation belts, from ≈ 2 to ≈ 6 terrestrial radii. The stations used, as already mentioned in Section 5.1 are located in the meridian region of 110° and cover a region in L -shell ranging from 1.51 to 6.75 R_E .

Figure 5.6 - Average power in the range of Pc5, for the horizontal component, along the IMAGE network located at approximately 110 CGM longitude for the period from 20 to 24 April 2003. The vertical axis represents the values for L -shell as a function of time in UT and MLT, the colors represent the average value of the wave power.



SOURCE: Author production.

The field measurements have a temporal resolution of 1 second, which is reasonable to obtain the signals at frequencies in the ULF range corresponding to Pc4-5, as already discussed in the previous sections. The signal is filtered using a *Butterworth* band-pass filter with cutoff frequency between 1 and 100 mHz, that corresponds to the pulse range already mentioned (SAMSON, 1991). To evaluate the signal in the frequency domain, a continuous wavelet transform with a Morlet analyzer function is applied to the filtered data, obtaining the Wavelet Power Spectrum (EPW). The average value of the power is extracted to obtain a quantification of the value of the power of the waves in each station in relation to the geomagnetic latitude and the value of L -shell.

5.5 Diffusion Coefficients

Radial diffusion transport must first obey the resonance condition given by: $\omega = m\omega_d$, where m is the azimuthal wave number and ω and ω_d are the frequency of the wave and the frequency of drift of the particle, respectively (SCHULZ; LANZEROTTI, 2012). To quantify radial diffusion one must consider that the process is stochastic, and thus it can be described by the diffusion theory. Thus, some empirical models of radial diffusion are proposed in the literature to explain the interaction between ULF waves and particles by calculating the radial diffusion coefficient (OZEKE et al., 2014; BRAUTIGAM; ALBERT, 2000; ELKINGTON et al., 1999). However, it is important

to highlight that all of them consider the dependence with the polarization modes of ULF waves in the efficiency of the interaction. [Elkington et al. \(1999\)](#) model considered an asymmetric field and quantified the efficiency of the toroidal mode, on the other hand, [Elkington et al. \(2003\)](#) model highlighted the importance of the poloidal and toroidal modes ([ELKINGTON, 2006](#)).

The radial diffusion coefficient is the average radial diffusion rate of a particle distribution in radial direction. The diffusion model proposed by [Brautigam and Albert \(2000\)](#) and latter incorporated with relativistic effects by [Fei et al. \(2006\)](#), is estimated from the sum of the electromagnetic (D_{LL}^M), and electrostatic (D_{LL}^E) components:

$$D_{LL}^E = \frac{1}{8B_E^2 R_E^2} L^6 \sum_m P_m^E(L, m\omega_d), \quad (5.9)$$

$$D_{LL}^B = \frac{\mu^2}{8q^2 \gamma^2 B_E^2 R_E^2} L^4 \sum_m m^2 P_m^B(L, m\omega_d), \quad (5.10)$$

$$D_{LL} = D_{LL}^E + D_{LL}^B, \quad (5.11)$$

where $\mu = \frac{p_\perp^2 L^3}{2m_e B_E}$ represents the first adiabatic invariant and γ the Lorentz relativistic correction factor, $\gamma = (1 - v^2/c^2)^{-1/2}$. B_E and R_E are the Earth's dipole moment and radius, respectively, P_m^E and P_m^B are the spectral power density of the disturbance of the electric and magnetic field, respectively, at the resonant frequency of $m\omega_d$, that satisfies the resonance condition.

The proposed models described above use equations that are proportional to the sum over all the wave modes power spectral density (PSD) and L-shell. It is possible to arrive at empirical functions for the diffusion coefficients, that can be based on in-situ measurements, or using geomagnetic index such as the global index Kp . [Ozeke et al. \(2014\)](#) formulated empirical expressions for D_{LL}^E and D_{LL}^B with data for a longer period of time and different L , taking into account periods with geomagnetic storms, characterized by the Kp index, those expressions are the most used in radiation belts models nowadays. However, the period of study did not comprises a well balanced cases with same geomagnetic intensities for Kp .

The empirical expressions for the coefficients proposed by [Ozeke et al. \(2014\)](#) only

assume positive values of m which contributes to the resonant interaction with the drift of the particles. He assumes that the power spectrum measurements are the PSD sum over m , so that the PSD value in each m is a fraction of the total PSD. These equations are used in the latest models of radiation belts, for example the Versatile Electron Radiation Belt (VERB) (SUBBOTIN; SHPRITS, 2009; DROZDOV et al., 2015). The estimate of PSD takes into account the geomagnetic activity estimated in terms of Kp index, but Ozeke et al. (2012) showed that the PSD estimate can be represented by other parameters as solar wind for instance, for compressional magnetic field, the PSD estimate can be expressed more generally by $P_{total}^B = B_{total}(L, I)f^{-2}$, where I can be a measure of the geomagnetic or solar activity, the Electric field can be expressed as $E_{total}(L, I)$. Ozeke et al. (2014) used I representing Kp index and showed P_{total}^B in units of nT^2/mHz expressed in function of Kp , L and frequency F in megahertz as:

$$P_{total}^B = F^{-2}10^{-0.0327L^2+0.625Kp^2+Kp0.499-25.9}. \quad (5.12)$$

The total power of electric fields in units of $(mV/m)^2/mHz$ can be expressed as:

$$P_{total}^E = 10^{0.217L+0.461Kp-4.11}. \quad (5.13)$$

The analytical expression for the diffusion coefficient for the compressional magnetic field, taking into account m and L is:

$$D_{LL}^B = \frac{L^8 4\pi^2 B_{total}(L, I)}{9 \times 8B_E^2}. \quad (5.14)$$

Taking into account the deduction presented in Ozeke et al. (2014), Equation 5.14 shows that if the compressional magnetic field PSD in each value of m varies as a function of the frequency $f \propto f^{-2}$, the resulting magnetic diffusion coefficient produced by these ULF waves does not depend on the energy of the electron, but only of the measured magnetic field. The equation can be expressed empirically by:

$$D_{LL}^B = 6.22 \times 10^{-13} L^8 10^{-0.0327L^2+0.625L-0.0108K_p^2+0.499K_p}, \quad (5.15)$$

and it is valid for frequencies below 8 mHz, m values higher than 10 and electrons

with energies ≥ 5 MeV (OZEKE et al., 2014).

Assuming that the total power spectrum of the azimuth electric field, P_{total}^E in the equatorial plane is independent of the frequency, but L and I , we arrive at the analytical equation for the electric field proposed by Ozeke et al. (2014):

$$D_{LL}^E = \frac{1}{8B_E^3 R_E^2} L^6 E_{total}(L, I). \quad (5.16)$$

If the total PSD does not depend on the frequency, the diffusion coefficient of the electric field produced by ULF waves can also be approximated empirically with data from the electric field and geomagnetic activity, expressed by:

$$D_{LL}^E = 2.16 \times 10^{-8} L^6 10^{0.217L+0.461K_p}. \quad (5.17)$$

Recently, Liu et al. (2016) made the derivation of the diffusion coefficients due to fluctuations in the electric field using measurements over a period of 7 years made by *Time History of Macroscale Interactions during Substorms* (THEMIS) and showed that there are differences between their model and the model proposed by Ozeke et al. (2014), having found a dependency with Kp and also with energy, not included in the model of Ozeke et al. (2014).

Sarris and Li (2016) made a PSD study for the compressional magnetic field during periods with HSS events for various wave numbers. His study shows that using probe measurements over different values of L for a given time, resulted in a dependence on L for that particular period. A distribution of measurements in several places helps to obtain a better understanding of the dependence on the wave power of radial diffusion in the phase space density of energetic particles

In order to verify the efficiency of different frequency bands of the ULF waves in the acceleration of the particles trapped in the external belt of Van Allen, the physical model of Brizard and Chan (2001) is used in this work. This physical model considers the spectral power of the waves in the compressional and poloidal mode, being more realistic than the empirical models for all periods of geomagnetic activity, including during weak and moderate storms. However, the methodology developed in this work supports the preliminary results that will be presented in the subsequent topics, as well as, it will enable the development of the proposed Thesis.

5.6 Phase space density

Phase Space Density (PhSD) is a quantity to evaluate the electron distribution, for a given energy, in a phase space. It is used to evaluate how particles in the radiation belts undergo over magnetic disturbances and fluctuations. PhSD is used in several areas of physics, such as quantum mechanics, thermodynamics, astrophysics and space physics. The most considerable interest here is the differentiation between mechanisms that lead to losses of electron and its population in the radiation belts.

The PhSD considers a coordinate system related to the trajectory of the particles in the belts. Van Allen Probes provide data on particle flux density at different pitch angles and energy ranges. Population processes, or particle losses in these regions are often linked to disturbances in the magnetic field in which some quantities must be maintained constants while others vary in a higher time scale than the characteristic movement of the particle and the medium studied, as we have already discussed in Chapter 4. Waves-particles interaction in these regions can alter the electron pitch angle leading to losses in the atmosphere; radial diffusion processes can transport electrons outwards, leading to losses to the magnetopause, so that the quantification of the relative contribution of each mechanism must be taken into account.

Particle detectors typically measure the electron flux at a distinct set of parameters: energy E , pitch angle α , position x , and time t . In turn, each of these parameters relates to one or more of the adiabatic invariants associated with electron motion in the geomagnetic field. The first adiabatic invariant, μ is dependent upon both the particle's pitch angle and the particle's energy. The second adiabatic invariant, K , depends upon pitch angle. The inverse of the third adiabatic invariant, L^* depends upon both position and pitch angle. A full definition of the adiabatic invariants is given by Schulz and Lanzerotti (2012), Green et al. (2004).

The conversion of the flux to PhSD can be performed following the steps showed on Hartley and Denton (2014), they show six steps to construct the conversion using in-situ measurements, made by the Van Allen Probes and calculation of the adiabatic invariants using International Radiation Belt Environment Modeling Library (IRBEM-LIB (BOSCHER et al., 2010)). The IRBEM-LIB is a set of source code dedicated to modelling the radiation belts and is available at <https://sourceforge.net/projects/irbem/>. The steps involve: 1) convert the differential flux to PhSD for each energy channel, in each instant of time; 2) For a given value of K , find the related pitch angle. For each energy channel, feature the pitch angle distributions and extract the PhSD values, given the energy spectrum. And

finally, for each instant of time, relate the measured pitch angle to the calculated L^* value; 3) For each value of μ , find the corresponding energy value. Adjust the energy spectrum curve to obtain the PhSD value as a function of μ , K , L^* and t .

The phase space density, relates to the differential particle flux, j , by the equation:

$$PhSD = \frac{j}{p^2}, \quad (5.18)$$

where p is the particle momentum. Inserting the expression for the relativistic momentum and a numerical factor to convert the units to the Geospace Environment Modeling (GEM) system, $\left(\frac{c}{MeVcm}\right)^3$ (GREEN et al., 2004; CHEN et al., 2005) in the equation 5.18, we have:

$$PhSD = 3.325 \times 10^{-8} \frac{j(E)}{E(E + 2m_0c^2)}, \quad (5.19)$$

where $j(E)$ is the differential particle flux given in $\#/s \cdot sr \cdot cm^2 \cdot keV$, m_0c^2 is the resting mass of the electron and E is the energy value of each detector channel, defined by $E = \sqrt{E_{min}E_{max}}$, where E_{min} e E_{max} are, respectively, the minimum and maximum value covered by the detector.

To obtain the flux, using the Equation 5.19, it is needed before we have a relationship between K and the pitch angle α . This relationship is given by the Equation:

$$K = \int_{S_m}^{S'_m} [\mathbf{B}_m(\alpha) - \mathbf{B}(s)]^{1/2} ds, \quad (5.20)$$

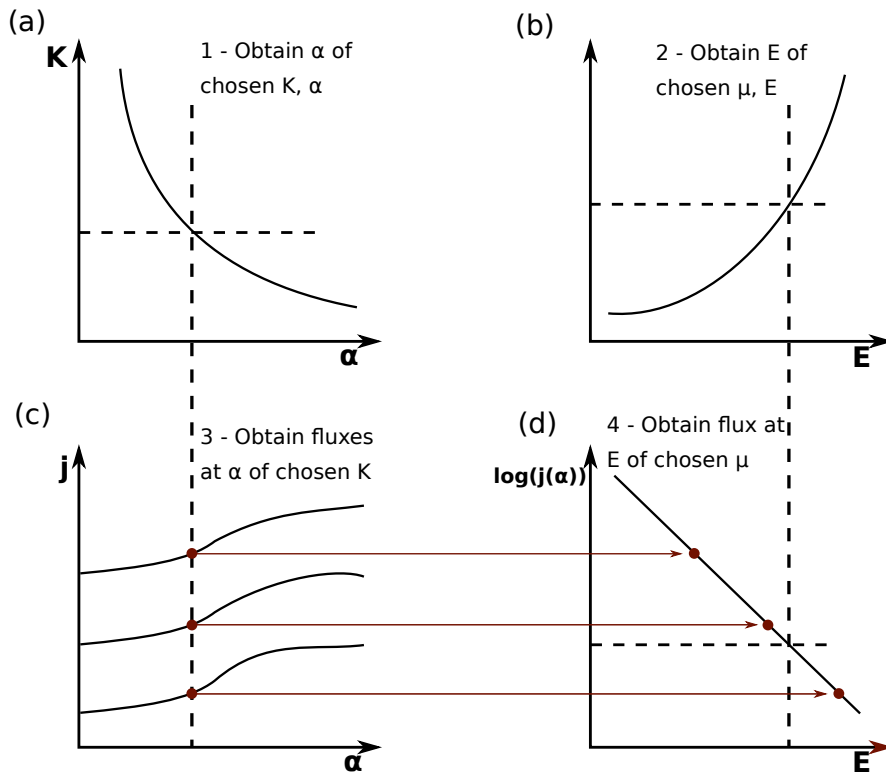
where B_m is the magnetic field at the mirror points, S_m and S'_m , using IRBEM-LIB routines. We can also use the values calculated for the Van Allen Probes, available at https://www.rbsp-ect.lanl.gov/data_pub/rbspa/MagEphem/definitive/. For each K value, there is a related α , this distribution can be fitted by an exponential equation, as shown in Figure 5.7-a.

μ , K and energy values are related by the following equation:

$$\mu = \frac{(E^2 + 2m_0c^2E) \sin^2 \alpha_K}{2m_0 \mathbf{B}c^2}, \quad (5.21)$$

with the values of α for a given K , we can build the relationship of μ and energy, using the equation 5.21, we can fit a curve as shown in Figure 5.7-b. The next step is to calculate the flux for the values of α for a given K , as shown in Figure 5.7-c. Thus, we can have a relationship between flux and energy values. This relationship can be adjusted by an exponential equation of the form $j = ae^{bE}$, where j is the calculated flux, E the energy, a and b are the coefficients of the curve. Getting the energy for a fixed μ (E_μ), is replaced in the curve fitting equation, using the calculated a e b coefficients, thus having the flux in function of μ e K , shown in Figure 5.7-d. After that, we use the Equation 5.19 to convert the energy flux into phase space density, $PhSD(\mu, K, x, t)$. A final step is necessary to convert the value of x in terms of the radial distance, related to the third adiabatic invariant L^* . This value is also calculated using the routines of IRBEM-LIB (HARTLEY; DENTON, 2014).

Figure 5.7 - Diagram showing the steps to fit the curves on the PhSD calculation.

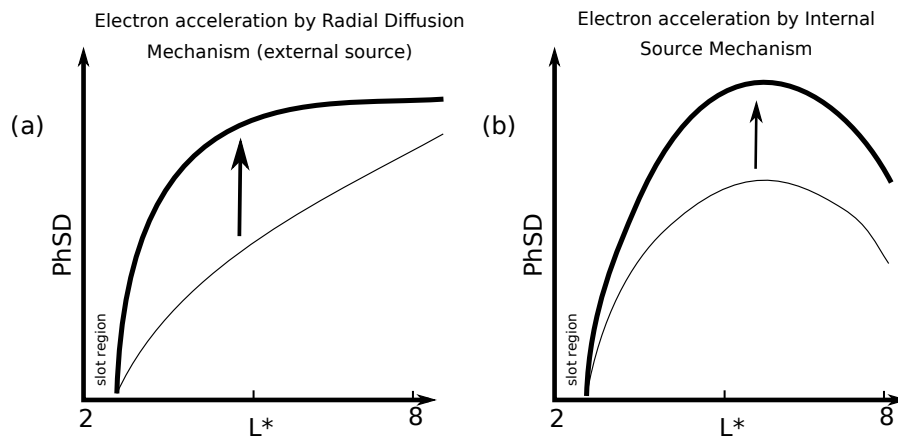


SOURCE: Adapted from Hartley and Denton (2014).

Calculating the PhSD as a function of L^* can help to differentiate between internal acceleration or radial transport processes or processes related to external factors in

the acceleration and electron transport of the radiation belts. In other words, it can be used to differentiate between radial diffusion and local acceleration of particles. Figure 5.8 shows a schematic representation of how PhSD behaves for both processes. Radial diffusion originates from high values of L , thus the PhSD increases or remains constant with the increase of L^* . Local acceleration has its source at lower values of L^* , so the peak of PhSD increases in this region over time.

Figure 5.8 - Diagram depicting the different signatures of radial diffusion (Panel A) and local acceleration (Panel B).



SOURCE: Adapted from Green et al. (2004), Hartley and Denton (2014).

6 STATISTICAL ANALYSIS

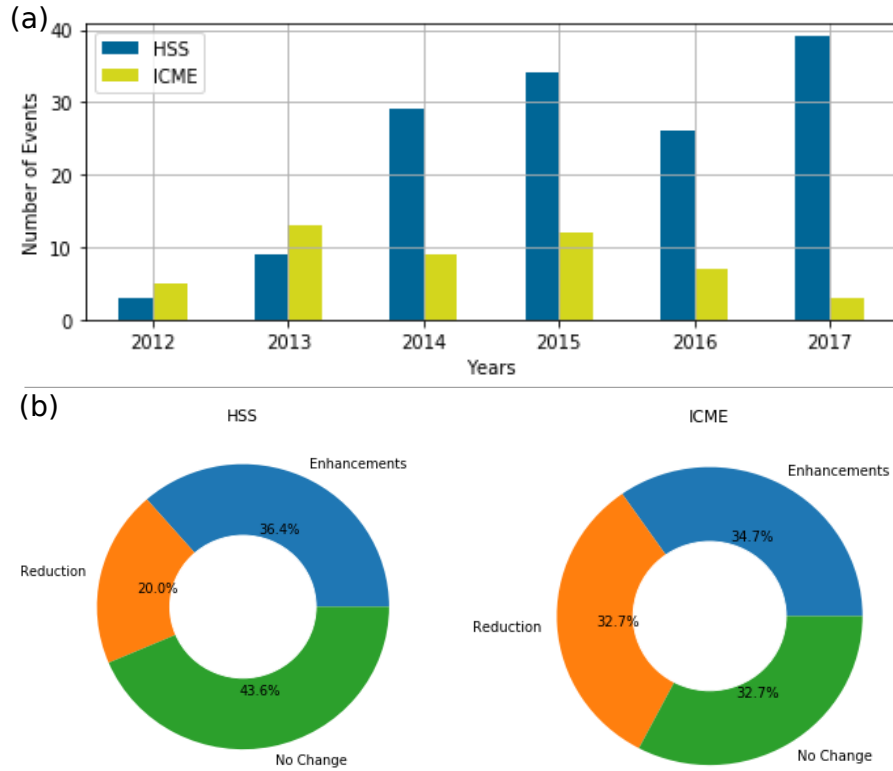
The dynamics in the radiation belts is very complex and the particle flux density variations in these regions can reach several orders of magnitude in just a few hours (REEVES et al., 2013; TURNER et al., 2019; TURNER et al., 2012). This variability is driven by a complex chain of processes extending from the solar wind into the inner magnetosphere (e.g., (PAULIKAS; BLAKE, 1979)). To facilitate this understanding, the scientific community has used geomagnetic storms as an indicator of the electron flux variability (e.g., (KIM; CHAN, 1997; BORTNIK et al., 2006)). A statistical study of the electron flux variability in geosynchronous orbits was made by O'Brien et al. (2001). They performed a cross-correlation between the parameters of the solar wind and the magnetosphere response to 33 storms that caused electron flux increase and 29 that had no changes. One result from O'Brien et al. (2001) that is important to highlight is that the intensity of the main phase, which is defined through the geomagnetic indices, is not a good indicator of the electron response in the outer boundary of the outer radiation belt. Murphy et al. (2018) conducted another statistical study using the total particle content in the radiation belts. They separated the events into the main phase of the geomagnetic storms, dominated by both loss and recovery phase of the radiation belt flux. The results showed that the two phases are clearly distinguished during geomagnetic storms. Recently, a statistical study performed by Turner et al. (2019) analyzed the response of the geomagnetic storms in the radiation belt electron flux variability. They used electrons flux data (20 keV to 6.3 MeV) during 110 storms with SYM-H \leq 50 nT. The response of the radiation belt flux variability shown to be energy and L dependent. They also showed that CME sheaths are more related to electron depletion at > 1 MeV and full CME and CIR are most likely to produce enhancement of MeV electrons around $L \sim 5.5$.

The present work complements these studies, comparing the period of the different solar wind structures (ICME and HSS) and the variability of relativistic electron flux density. The different approach in this work is to separate the events without considering the geomagnetic storms. Here we took into account only the interplanetary structures that may be related to electron flux variability. Thereby, to develop the present work we use observational data from ACE satellite and Van Allen Probes throughout their entire operation period, from both A and B probes. The high-energy electron flux variability in the outer radiation belt is analyzed during all ICME and HSS events, in which the events are separated according to the electron flux density variability (increase and decrease flux). The data and instruments used were described in the Chapter 5. For all events, an overlapping time analysis

was performed in the flux of relativistic electrons, solar wind parameters, and the spectral power integrated into the ULF range. The methodology was described in detail in Chapter 5, in which we used an overlapping time analysis applied to the relativistic electron flux, solar wind parameters, and the spectral power integrated into the ULF range. In the period between October 2012 and December 2017, we identified 49 ICMEs events. Among these, 17 are related to the flux increasing and 16 to flux reduction. For HSS, there were 140 events; among these, 51 are related to the flux increasing and 28 to flux reduction. The criteria for selecting events with an increase or decrease influx were presented in Section 5.3.1. The events were chosen only taking into account the type of the interplanetary event (CME or HSS), regardless of whether or not the event caused any geomagnetic storm or sub-storm, and the relationship to the flux was only defined based on electron flux density measurements in $L - shell = 5 R_E$.

In Figure 6.1-a, the quantities referring to the survey of HSS and ICME events are presented. The proportion between those that may be associated with an electron flux reduction or increase in the outer belt is shown in Figure 6.1-b.

Figure 6.1 - (a) Number of ICME and HSS events per year, arriving on Earth, related to changes in electron flux observed during the first four years of the Van Allen Probes mission. (b) The proportion of events that may be associated with dropouts or acceleration in the flux of electrons from the outer belt. In the panel (b)-left are the HSS related events and the panel (b)-right show the ICME related events.



SOURCE: Author's production.

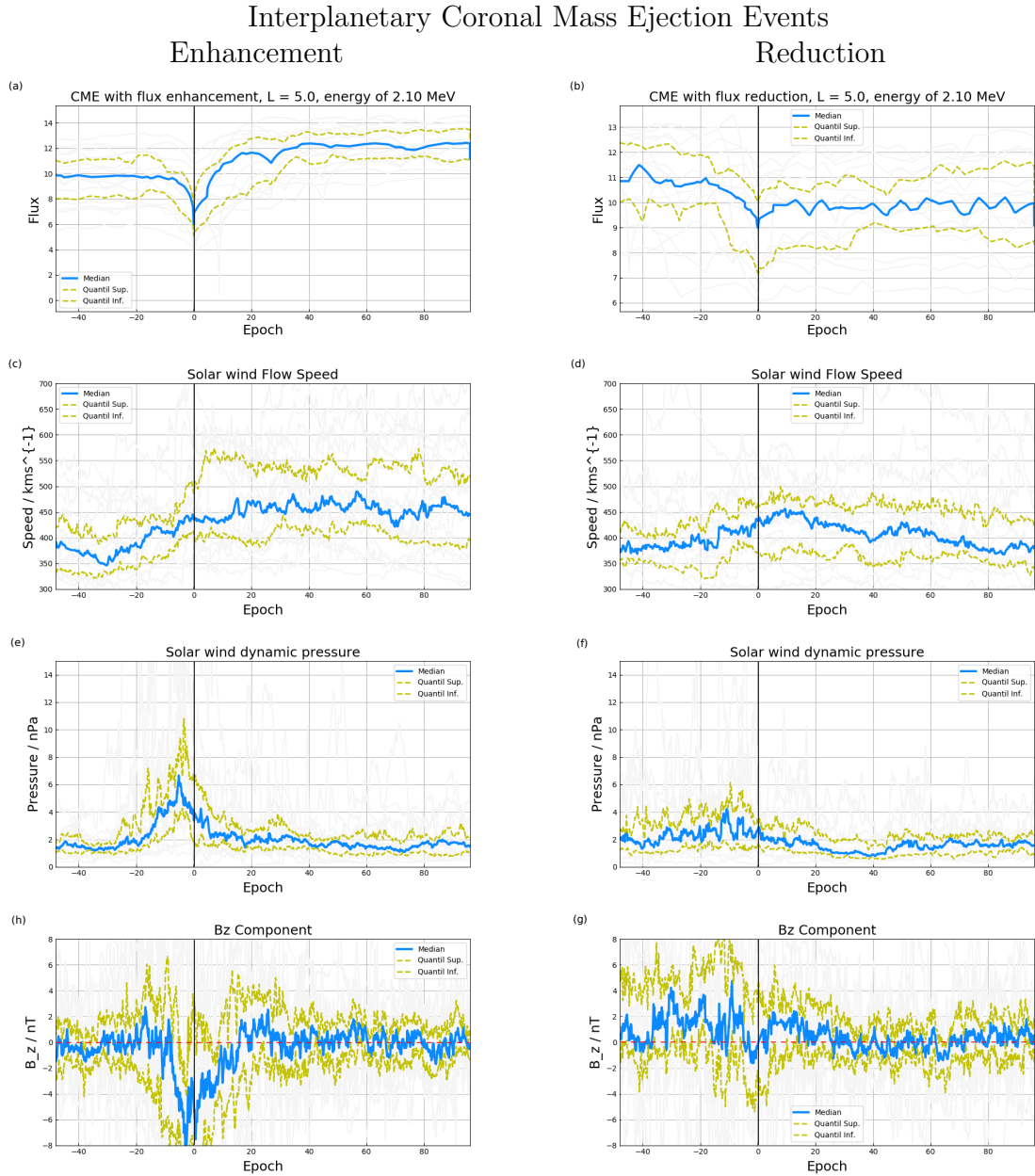
Note that $\sim 34\%$ of ICME may be associated with a reduction in electron flux and $\sim 32\%$ with repopulation. Most HSS is not related to changes in flux, only $\sim 36\%$ can be associated with repopulation and $\sim 20\%$ to flux depletion.

6.1 Coronal mass ejection events

Electron flux density and interplanetary data for all 17 events related to flux increase and 16 events related to flux decrease that are linked to interaction with an ICME, are shown in Figure 6.2. Events with flux increase or decrease are defined from the changes observed in the electron flux density in the energy level of 2.10 MeV in $L^* = 5 R_E$. As mentioned earlier, in Chapter 5, the zero time in the SEA, t_0 , is defined as the instant when the electron flux density value, at L-shell = 5 ER, is

minimum, after the arrival of the solar wind structures in the Earth's magnetosphere, considering the portion before the event, a period of 50 hours before t_0 , and the period after the event, 100 hours after the flux flux minima. Figure 6.2 shows the SEA for the electron flux density with energy 2.10 MeV, together with the solar wind parameters. The events with the increased flux are shown on panels on the left, and for decreased flux are displayed on panels on the right, considering all disturbances in the Earth's magnetic field caused by interaction with ICMEs. The solid blue lines show the median of the values, while the dotted yellow lines represent the upper and lower quartiles. The solid black vertical lines mark the zero time in the time overlay analysis, and the red dotted lines in the g and h panels refers the magnitude zero of the IMF B_z component.

Figure 6.2 - Superposed Epoch analysis on the 2.10 MeV electron flux and solar wind parameters for flux enhancements (panels a, c, e, and g) and reduction (panels b, d, f and h), for ICME events. The solid blue line corresponds to the median, while the yellow ones are the upper and lower quartiles. From top to bottom: Relativist electron flux density, solar wind speed, proton density and Interplanetary Magnetic Field (IMF) in the z-component.



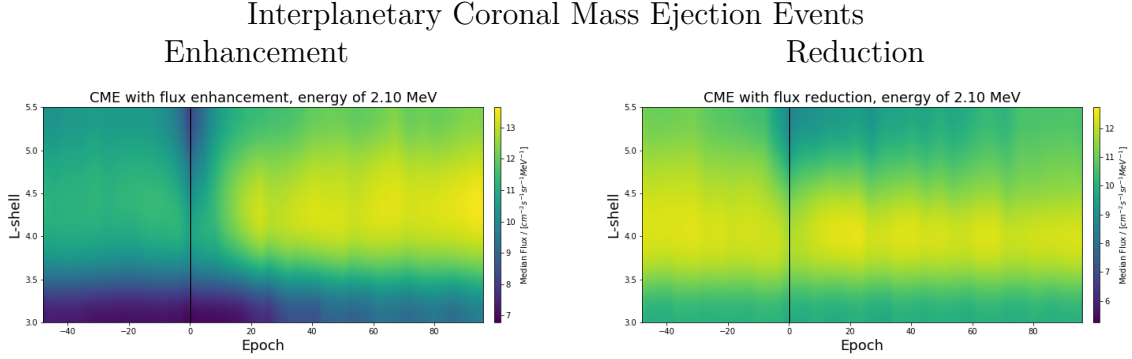
SOURCE: Author's production

Observe that the maximum of solar wind dynamic pressure, Pd_{sw} , occurs, on aver-

age, approximately 6 hours before the minimum of the flux density in both cases. Pd_{sw} presented a value almost twice bigger and a shorter duration in enhancement cases (flux increase) compared to reduced events (flux decrease). It is also observed, both in the enhancement and in the reduction cases that the dropout period occurred during the southward B_z , as found in the statistical studies by Yuan and Zong (2013a), Ni et al. (2016). The characteristics of the solar wind dynamic pressure and B_z component detected here during the electron flux dropouts agree with the superposed epoch analysis performed by Gao et al. (2015). They found that either large solar wind dynamic pressure or southward IMF B_z is capable of driving dropouts. On the other hand, Kilpua et al. (2015) conducted a similar study and organized the results by particular solar wind drivers. They found that the distinct characteristics associated with the different solar wind drivers corresponded to distinct responses by outer belt electrons. It means that the methodology used here is promising to found the new results due to the selection criteria.

The characteristics of the solar wind parameters to both the enhancement and reduction events during ICME are clearly different in terms of intensity. For events with increased flux, the solar wind speed, V_{sw} , has a maximum of about 40 hours after t_0 and remains at that value, on average, in subsequent hours. In contrast, for reduction events, the maximum is around 10 hours after t_0 and gradually reduces its value in the following hours. A significant difference can be seen in the component of the IMF in the z direction, B_z , the intensity is much more expressive and with predominantly negative values for events with enhanced flux. In events with reduced flux, the B_z remains positive, on average, before t_0 , there is a small reduction to negative values, not reaching -2 nT a few hours before t_0 and returns to be positive on average in the subsequent 20 and then returns to an average of zero in subsequent hours.

Figure 6.3 - Superposed Epoch analysis for the electron flux density in L-shell ranging from 3 to 5.5 R_E , in cases of enhancement (Left) and reduction (Right), during coronal mass ejection events.



SOURCE: Author's production

The SEA was performed to the electron flux density, at 2.10 MeV, for measurements along the L-shell. Here, it was also done on the interpolated flux with a zero epoch, t_0 , the same as mentioned before. Figure 6.3 shows the SEA for electron flux density according to L-shell. The values go from 3 to 5.5 R_E . The x-axis shows the epoch times and the y-axis the L-shell in terms of R_E . The vertical black line indicates the t_0 , and the colored map is the median value for the flux density at each L-shell value, for all the ICME events. The panel on the left represents the flux enhancement events, and the right-hand side panel represents the reduction events.

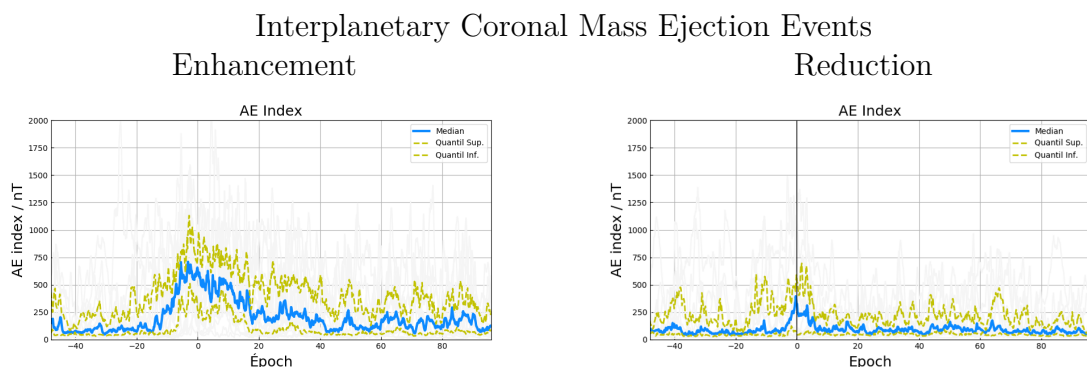
We can see that, for enhancement events, the flux, prior to t_0 , was low in all L-shell range. At the time interplanetary structure interacts with Earth, the depletion is more significantly at high L-shell - this reduction is observed in the Figure 6.3 the reduced intensity denoted by an blue region around the t_0 . Another fact is the low flux density at lower L-shell, before the structure arrival. After the interaction with the magnetosphere, t_0 , the flux starts to increase almost at the same time for all L-shell. This behavior continues as the structure passes through and interacts with Earth's magnetosphere. But, it suggests that the interaction that generates this electron flux enhancement is relatively short, as the flux reaches a maximum value ~ 40 hours after t_0 and remains at his value for the next hours.

Looking to the right panel, we can see a opposite behavior. The flux was high before t_0 , and at the moment of interaction occurs a rapid depletion on all L-shell values.

The flux returns at L-shell around $3.5 - 4.5 R_E$, at values higher than 4.5, the flux stay at lower values. For L-shell values between greater than 5.0 and lower than $5.5 R_E$, the flux reduces at t_0 and remains for the next 20 hours, and starts a small recovery after that. At L-shell between 4.5 and $5.0 R_E$ the flux values reduces, compared to the period before t_0 and stay at same value for all the subsequent period.

Considering the interplanetary medium behavior, showed in Figure 6.2, the enhancement events, due to ICME, are characterized by an intense solar wind pressure and strong B_z with negative values. Those factors are a good indicative of geomagnetic storm onset. The solar wind speed has an increase, on average, less than 100 km s^{-1} with the southward B_z and the solar wind dynamic pressure, can disturb the magnetosphere. As Turner et al. (2019) reported, the main phase of a geomagnetic storm is characterized by a flux reduction on high energy electrons flux. These dropouts are followed by an electron enhancement, during the storm recovery phase. For the depletion events, the solar wind parameter show less intense values with small amplitude in the solar wind pressure and solar wind speed. That could explain the fluz reduction observed in Figure 6.3-right.

Figure 6.4 - Superposed Epoch analysis for the AE index, for enhancement (Left) and reduction (Right), during coronal mass ejection events. The same configuration and color lines as Figure 6.2.



SOURCE: Author production

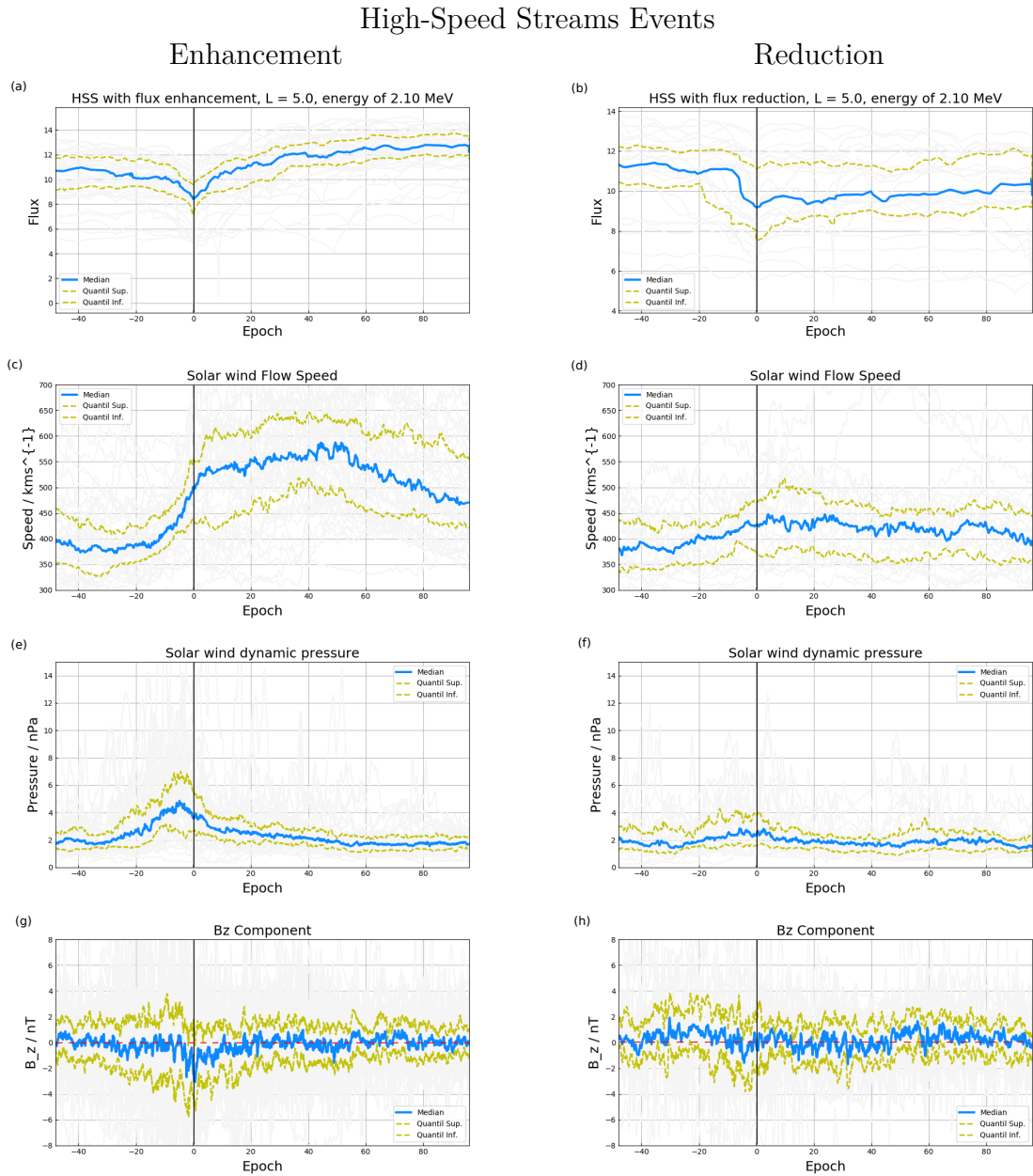
Figure 6.4 shows the SEA for the AE index during enhancement (left) and depletion (right) events. The AE index is higher from t_0 throughout the next ~ 20 hours. For

the depletion cases, the AE index is slightly increased at t_0 and returns to a normal value after a couple of hours, the same occurs to the B_z component in Figure 6.5-h.

6.2 High-speed streams events

Figure 6.5 shows the same configuration as Figure 6.2, but for the events related to HSS arrival. Through the selection criteria presented in Chapter 5, were selected 51 events with electron flux increase (enhancement cases) and 28 to electron flux decrease (reduced cases). Figure 6.5 showed that the maximum value of V_{sw} related to enhancement cases has a maximum of $\sim 600 \text{ km s}^{-1}$, while the results related to reduced flux cases the maximum V_{sw} is $\sim 450 \text{ km s}^{-1}$, which occur around 50 hours and 20 hours after t_0 , respectively. The dynamic pressure is also larger for events with increased flux and its maximum occurs around 10 hours before t_0 for both cases, as well as for ICME events. The B_z component is also southward, on average, for enhancement cases, while for reduced cases, the B_z component is northward. The B_z component for HSS cases (Figure 6.5) is also significantly smaller if we compare both electron flux dropouts in HSS and ICME cases (Figure 6.2).

Figure 6.5 - Superposed Epoch analysis on the 2.10 MeV electron flux and solar wind parameters for flux enhancements (panels a, c, e, and g) and reduction (panels b, d, f and h), for HSS events. The solid blue line corresponds to the median, while the yellow ones are the upper and lower quartiles. From top to bottom: Relativist electron flux density, solar wind speed, proton density and Interplanetary Magnetic Field (IMF) in the z-component.

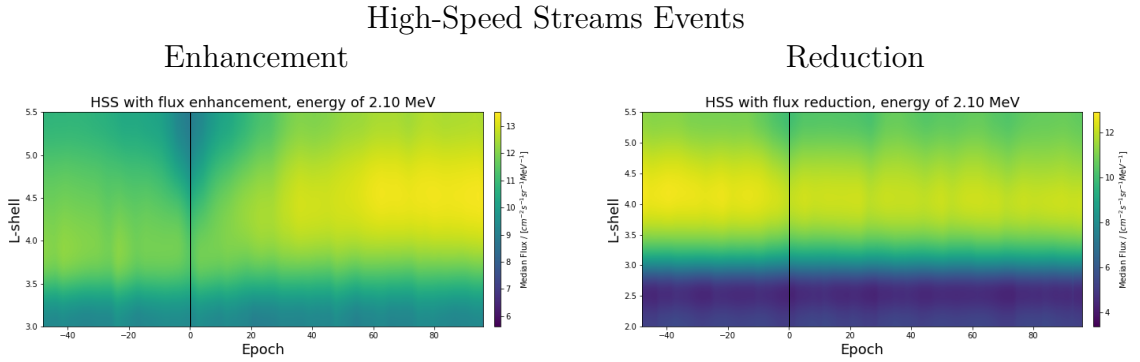


SOURCE: Author's production

We observe that in cases where there is an increase in the high energy electron flux,

the negative value of B_z is a feature present in both ICME and HSS. The opposite occurs for cases with reduced flux. The auroral activity was also verified (Figure 6.7) through the Auroral Electrojet index (AE), which is a good indicator of sub-storm activity, the AE index presents higher intensities for electron flux enhancement cases and is not significant for the electron flux reduction cases. The flux increases related to substorm activity have been reported by Forsyth et al. (2016). Meredith et al. (2003) suggests that periods of prolonged storm activity may be necessary to energize the radiation belts. Also, Rodger et al. (2015) showed that recurrent substorms are more efficient to energizing particles.

Figure 6.6 - Superposed Epoch analysis for the electron flux density in L-shell ranging from 3 to 5.5 R_E , in cases of enhancement (Left) and reduction (Right), during solar wind high-speed streams events.



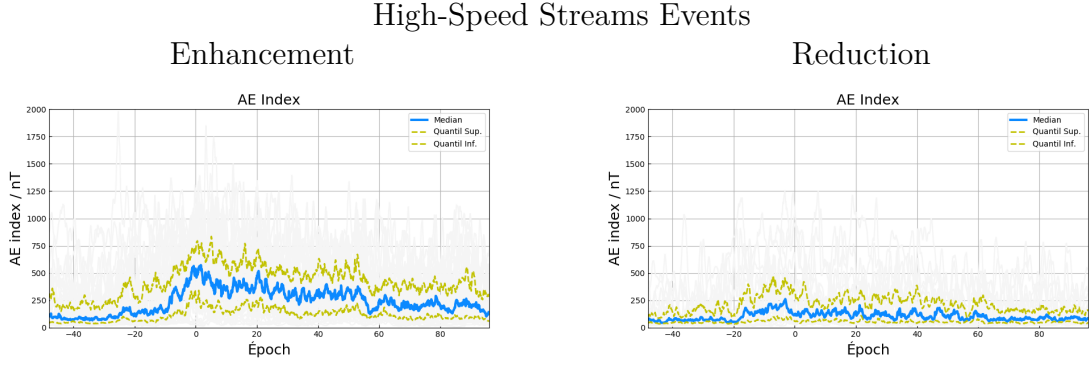
SOURCE: Author's production.

Figure 6.6 shows the SEA for the HSS events, the figure has the same configuration as Figure 6.3. Considering the left side, and comparing with the ICME events, the radiation belt particle enhancement start occurs ~ 20 hours after t_0 continues gradually to increase and reaches a maximum in the subsequent hours. For $L > 5.0$ the flux increase begins after a extended period, ~ 60 hours. The flux at $L < 4.0$ didn't suffer significant variations in both cases.

For reduction events, the most significant region is at $L > 4.5$ and the reduction is not abrupt, it starts to decay gradually. After the t_0 , the flux remains low during all period on average. The region between 3.5 and 4.5 R_E shows a flux reduction as well, and remains with this amount of particles during the period.

Considering the interplanetary parameters in Figure 6.5, the most significant variation is observed at the solar wind speed, in which the higher variation is seen in the enhancement events. The B_z component is also southward at t_0 and remains negative, on average, for the next ~ 60 hours after t_0 . Comparing to Figure 6.6 it corresponds the time period where the flux starts to increase. Figure 6.7 also show similar behavior, the AE index is higher from t_0 throughout the next ~ 60 hours. For the depletion cases, the AE index is slightly increased at t_0 and returns to a normal value after a couple of hours, the same occurs to the B_z component in Figure 6.5-h.

Figure 6.7 - Superposed Epoch analysis for the AE index, for enhancement (Left) and reduction (Right), during HSS events. The same configuration and color lines as Figure 6.2



SOURCE: Author's production

Particle injections promoted by substorms are known as a major contributor to increases the radiation belt particle flux. Substorms are thought to provide the low-energy population of keV electrons, which are subsequently accelerated adiabatically to higher energies, up to MeV (BAKER et al., 1998; HORNE; THORNE, 1998; FOK et al., 2001). These injected particles reach energies, on average, lower than that observed at the relativistic particle population at the outer radiation belt, though do not have sufficient energy, and species, to significantly enhance the relativistic particle population. Thus, those low energy particles, also known as seed population, may be also locally accelerated by wave-particle interactions and can reach the highest energy at the outer radiation belt. The process involves an interaction with whistler-mode chorus waves to accelerate the particles up to relativistic energies.

Miyoshi and Kataoka (2008) suggested that the IMF-Bz dependence of the flux enhancement of relativistic electrons may be attributed to substorm activities during an HSS event. Meredith et al. (2003) found that flux enhancements can occur during prolonged substorm activity even in the absence of a magnetic storm. Lyons et al. (2005) indicated that the enhancement of both relativistic electrons and the whistler-mode waves that drive the electron acceleration processes are associated with the enhanced convection driven by Alfvénic fluctuations within an HSS.

Kilpua et al. (2015) applied the same SEA methodology and a comparison between the variation before and after the interaction between ICME and CIR for the flux of relativistic electrons measured by the Geostationary Operational Environmental Satellite (GOES). The results confirm that CIR is more efficient structures for increasing the flux of these particles in geostationary orbits. They showed that the flux decreases at the moment of interaction with the CIR and then increases during the passage of the whole complex structure, CIR followed by a HSS, through the magnetosphere. Concerning ICME events, sheath compression tends to cause the flux to decrease, but without a definite conclusion about the effects of this structure.

The SEA results presented here show that HSS is more effective at generating enhancements of MeV electrons at L-shells higher than $4.5 R_E$; while ICME related events are more effective causing enhancement from lower to higher L-shells. These results agree with Turner et al. (2019) regarding the behavior of the interplanetary structures and the high energy electrons. They considered only geomagnetic storms with SYM-H minima < -50 nT. As mentioned earlier, we did not distinguish between quiet period or geomagnetic storms, instead we separated two interplanetary events. The characteristics of electron flux depletion at the main phase of a geomagnetic storm, reported by Turner et al. (2019) also appears in the events presented in this work, but not only during geomagnetic storms, but it also appears in many cases where the solar wind pressure increase due to the interactions with Earth’s magnetosphere. This depletion, even if small, occurs in both ICME and HSS events and it was used to define the zero-epoch for the SEA in this work, as mentioned before.

6.3 Power spectrum

Now let us consider the behavior of ULF waves carried by the interplanetary events observed by the Van Allen Probes. The SEA was performed to the Power Spectrum Density (PSD) for the Pc5 wave frequency range recorded by EMFISIS instrument. Here, the t_0 was defined in the same way as the previous analysis, as being the time

when the flux at L-shell = 5 is minimum.

Figures 6.8 and 6.9 show the median value of the Pc5 power spectral density at four different L-shell values for ICME and HSS events, respectively. On the left-hand side panels (a, c, e, and g) are the PSD for enhancement events, while on the right (b, d, f, and h) are the PSD for reduction events. From top to bottom the PSD is presented at L-shell from $5.0 R_E$ to $3.5 R_E$. The lines in blue color are the median of the measurements and the yellow ones are the upper and lower quartiles.

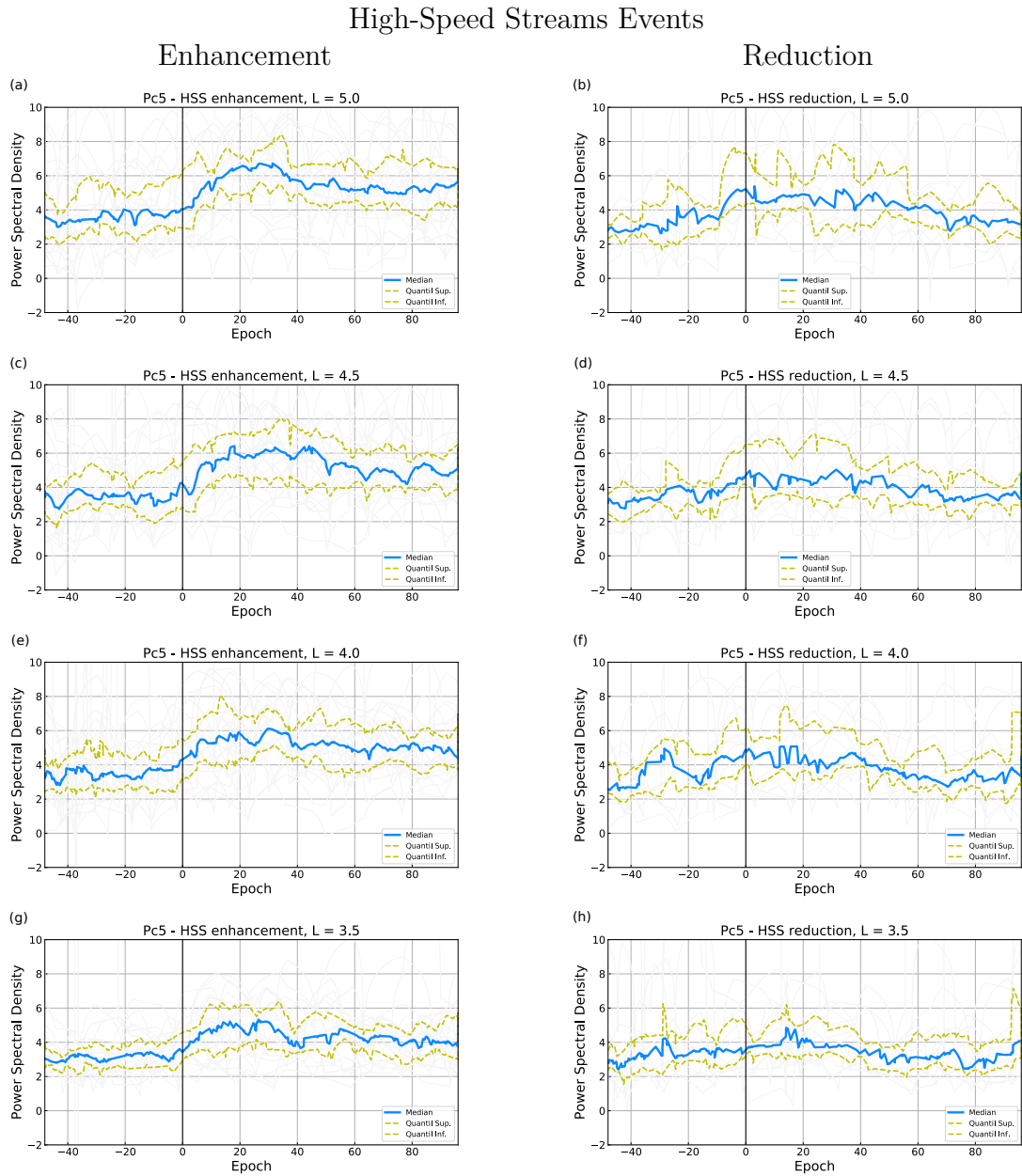
Considering ICMEs related to the enhancement events, in Figure 6.8, the mean PSD has a maximum at around 18-25 hours after the t_0 , for all L-shell values, with higher intensities at higher L-shells. For the reduction related events, the mean PSD maximum occurs at different moments, in which the PSD appears around 20 hours earlier than the t_0 at L-shell equal to $4.5 R_E$ and $5.0 R_E$. For lower L-shell the maximum PSD occurs at around 15 hours after t_0 . After the analysis showed before, we can suggest that the waves can be responsible to take energy from one region and bring to another, besides to diffuse particles, and somewhat contribute to perturb the environment. In this way, for the reduction events related to ICMEs, we can suggest that the ULF waves can contribute to change magnetosphere conditions before the disturbed solar wind arrival, for the enhancement events related to ICME, we observe that the ULF wave activities are maximum after the ICME arrival at magnetosphere.

For HSS events, Figure 6.9, the behavior is a bit different. The maximum PSD, for enhancement events, occurs around a day after the t_0 , and remains high for the next 3-4 days, compared to the time before the t_0 . For depletion related events, the maximum PSD amplitude is not well defined, but we can observe that it occurs around the t_0 and the amplitude is not as high as the other events, the wave activity starts earlier and remains for 3-4 days.

Figure 6.8 - Superposed Epoch Analysis Pc5 Power Spectral Density in L-shell values from 3.5 to 5.0 during flux enhancements (panels a, c, e, and g) and reduction (panels b, d, f and h), for ICME events. The solid blue line correspond to the median, while the yellow ones are the upper and lower quartile.



Figure 6.9 - Superposed Epoch Analysis Pc5 Power Spectral Density in L-shell values from 3.5 to 5.0 during flux enhancements (panels a, c, e, and g) and reduction (panels b, d, f and h), for HSS events. The solid blue line correspond to the median, while the yellow ones are the upper and lower quartile.



SOURCE: Author's production

There is a clear distinction in the mean ULF activity associated with ICME (Figure 6.8) and HSS (Figure 6.9) and also between enhancement related events from

depletion related ones. In both the HSS and ICME cases, the ULF wave amplitude is smaller for depletion events. Also, the duration of ULF wave activity is different between enhancement and depletion events, both for ICME and HSS. For enhancements events, the ULF wave powers lasted longer. Also, during the HSS the ULF wave activities duration is even longer, lasting days. In ICME events, the maximum ULF wave power peak appears earlier at higher L-shell.

Let us focus in the ICME events on Figure 6.8. The mean wave activity of enhancement events (Figure 6.8-left) occurs a day after the t_0 and presents a short duration peak, which subsides after three subsequent days. During reduction events, the ULF wave activity peak occurs earlier for L-shell higher than $4.0 R_E$ and later for lower L-shells. Comparing with Figure 6.2, the maximum PSD in enhancement events is similar to the behavior of the flux enhancement, in which the ULF wave starts to increase at t_0 up to reaches a maximum after around 40 hours. This maximum ULF wave activity occurs around the same time that the flux reaches its maximum. Also, the mean solar wind speed and B_z component present fluctuations 18-20 hours after the t_0 . The flux enhancement in an L-shell, Figure 6.3 on the left, shows how the mean flux increase with L-shell, this behavior agrees with the PSD, in which the electron flux starts to increase around 18 hours after t_0 , and the ULF wave activity also starts to grow. It is important to highlight that the PSD starts to enhance the amplitude in the same way for lower L-shell values.

For reduction events (Figure 6.8-right), as pointed before, there are two moments where the wave amplitude reaches a peak, before t_0 , for higher L-shells and after t_0 , for lower L-shells. Figure 6.2-b shows that the mean electron flux density at L-shell = $5.0 R_E$ starts to decrease ~ 20 hours before t_0 , similar to the mean wave activity for higher L-shells. Also, the mean solar wind speed (Figure 6.2-d) presents a sudden impulse and fluctuations in dynamic pressure (Figure 6.2-f) and B_z (Figure 6.2-h). The right panel in Figure 6.3 shows how occurs the reduction in the electron flux at different L-shell values. The mean electron flux stars to decrease earlier for high L-shells and gradually reaches a minimum at all L-shells at t_0 . After ~ 20 hours, there is another small reduction in electron flux at lower L-shells, around the moment that there is a peak in wave activity at lower L-shells. The AE index, Figure 6.4-right also presents an auroral activity right before t_0 , it can be related to the main phase of the geomagnetic storm caused by ICME and after the activity lasts for ~ 24 hours, suggests a substorm activity due to the impact of this interplanetary event. The impact of the ICME in the magnetosphere can generate impulsive waves right after the shock and this can be transmitted into the magnetosphere.

The relation between ICME interacting with the Earth’s magnetosphere and causing dropouts is a subject of study of many authors. The loss processes in the outer radiation belts were studied by [Hietala et al. \(2014\)](#), they found that ICME was effective on outer radiation belt losses, particularly at storm events, in which they have shown that the Dst can act in concert with magnetopause shadowing and outward radial diffusion by ULF waves. As mentioned before, [Kilpua et al. \(2015\)](#) did a similar study with different solar wind drivers and found that strong magnetic fluctuation and the high solar wind dynamic pressure associated with the stream interface on ICME sheets and ejecta correspond to sudden losses of electrons observed by GOES satellite. [Yuan and Zong \(2013b\)](#) found that enhanced solar wind dynamic pressure and southward interplanetary magnetic field are related to intense electron flux dropouts. [Boynnton et al. \(2017\)](#) found that dropouts at $L \sim 4.2 R_E$ are more pronounced and frequent for electrons with energies higher than 1 MeV, arguing that outward radial diffusion transport and magnetopause shadowing acts in the outer radiation belt losses. Those effects were also reported by [Moya et al. \(2017\)](#), they found that often, losses of electrons started at higher L-shells and than moved in, consistent with magnetopause incursions and outward radial diffusion.

In the HSS events, Figure 6.9-left, we can note that the mean wave activity for enhancement present similar features for the different L-shells with a small difference in intensity. The activity has a maximum around 20h after t_0 and remains high for the subsequent days. In the Figure 6.5-left we can observe how the interplanetary parameters varies at the time of wave activity. The panel (Figure 6.9-a) shows the flux enhancement and it appears that the mean value starts to increase, compared to the values at the time before t_0 , around 18-20 h after, almost at the same time as the ULF wave reaches the maximum. Also, the B_z component (Figure 6.9-g) is mostly southward during the enhancement period on flux and wave activity. The solar wind speed (Figure 6.9-c) up to reaches a maximum around 20 after t_0 and remains with high values during at least 3 days, which is the time wave activity is high. The Figure 6.7-left also presents a high amplitude in the AE index, that is higher at t_0 and remains with auroral activity up to 3 days after, indicating that, as expected, the substorm activity increased during HSS and there was enhancement on the electron flux density, with high ULF waves activity during the period.

In the reduction cases (Figure 6.9-right), ULF activity is not as intense as for the enhancement cases. The solar wind increase are not significant, the mean solar wind speed reaches a maximum of ~ 450 km/s, there are small fluctuations on B_z (Figure 6.9-h), that is mostly northward. It suggests that ULF waves have small im-

pact on those cases. As discussed before, the mean ULF power does not have high amplitudes for reduction cases related to HSS events. The reduction may be associated with another process, that may be related with waves in another frequency range. Turner et al. (2019) performed a study with 47 storms related to SIR events, although they considered storm related events, the results shows that SIR's related events are more linked to MeV electron enhancements at high L-shells. Our results also show a similar result in Figure 6.2. We can observe that in the HSS related events, the enhancement is more relevant at higher L-shell values for the electron energy level of 2.10 MeV.

The choice of zero epoch being the lower flux density at L-Shell = 5 is a factor that may imply on the wave power occurrence time, since it takes into account only the flux variation caused by an external interaction. We noted that in most cases there are this minimum on flux after the interaction with a solar wind structure, that was the motivation to chose that specific time as the zero epoch for the SEA. This study complements the work performed by other authors, e.g. Turner et al. (2019), Kilpua et al. (2015), Murphy et al. (2018) and add another framework to analyze flux variation due to the interaction with different solar wind structures. We did not consider there was a storm or substorm to select the events, only the interplanetary medium was taken into account in this selection. The results on flux variations agreed with previous works, showing that ULF waves are more intense during enhancements both for ICME and HSS related events. In the reduction cases ULF waves are present but with lower intensity and not well correlated. It may indicate that ULF waves are acting together with other processes, such as magnetopause shadowing, or interaction with higher frequency waves (e.g. Chorus or EMIC waves).

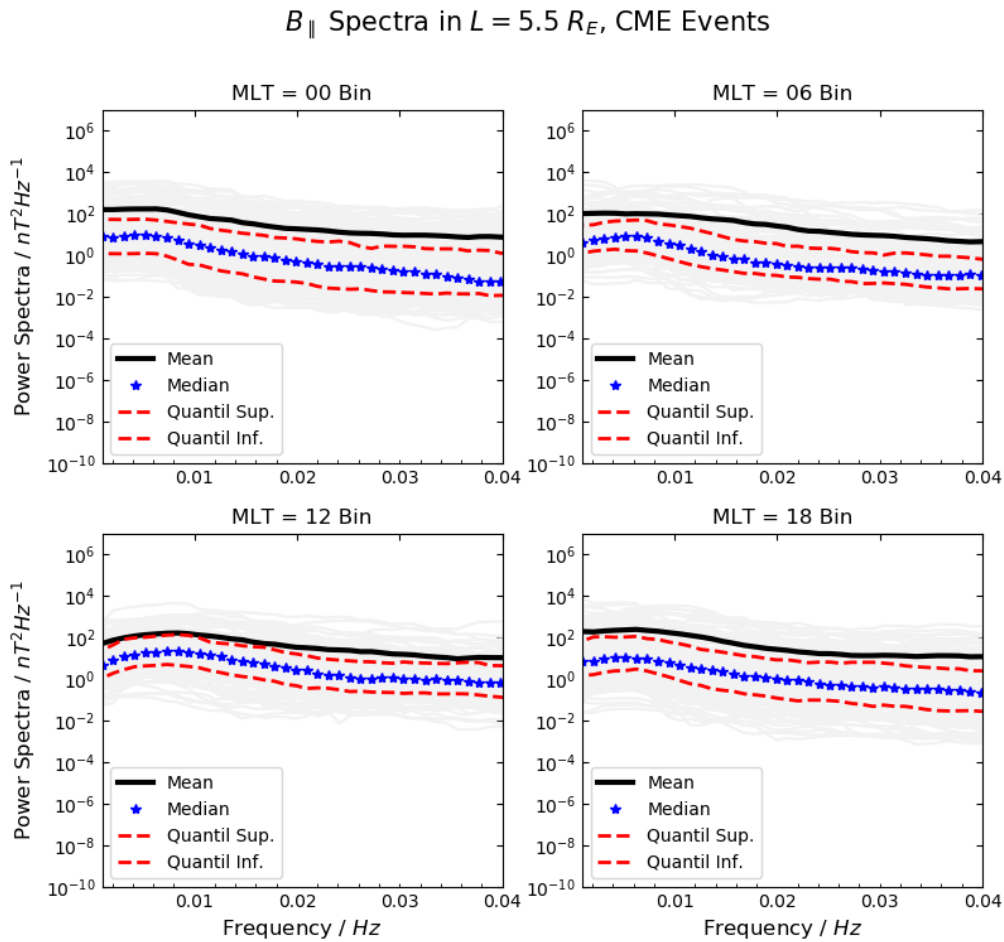
6.3.1 Integrated Power Spectrum

It is essential to estimate the spectral power in relation to the values of $L - shell$ and the Magnetic Local Time (MLT) to analyze the behavior of the spectral power and its relationship with the increase of the electron flux in the radiation belt. The ULF waves act as a mechanism able to change particle's energy. They can accelerate or decelerate particles, or transport them by means of diffusion processes trough the magnetosphere. The formulations of the diffusion coefficients proposed by Fei et al. (2006) is based on the value of power spectrum density as a function of L-shell, because of that these parameters are important and necessary. This formulation requires the spectral power, in the ULF waves range, for the compressional mode of the magnetic field and the azimuthal mode of the electric field, in an average

according to the drift of the particle around the Earth, as explained in Section 5.5.

To contribute with the understanding of ULF waves diffusion ability in the Van Allen Probes era scope, we calculate the PSD, in the ULF frequency range to L-shell values ranging from 3.0 to 5.0 ER. For L-shell, six bins were used, which are centered at 3.0, 3.5, 4.0, 4.5, 5.0 and 5.5 ER. Each L-shell bin are 0.5 ER wide. The calculation was done using all ICME and HSS events.

Figure 6.10 - Power Spectrum Density for the compressional magnetic field at $L^* = 5.5$ and MLT sectors of 0, 6, 12 and 18 for all ICME events. The lines colored red shows the upper and lower quartile, the mean is in black and the median in blue.

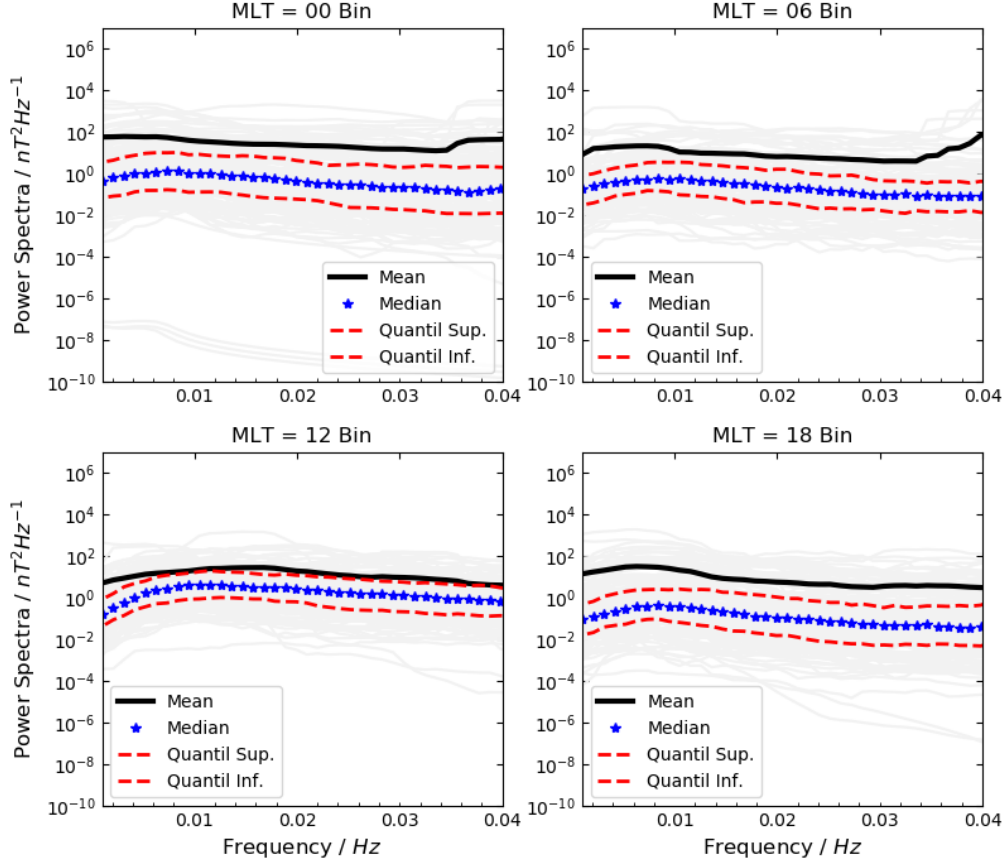


SOURCE: Author's production.

The Figure 6.10 shows the power spectrum of the compressional magnetic field at $L^* = 5.5$ ER for all ICME events and in four different MLT sectors 0, 6, 12 and 18. The power spectra within each *bin* are in the gray shaded color. The panels also show the mean, the median, and the lower and upper quartile. There is a large variation, in the power spectral frequency range, this shows that there is a great variation in the power density even for a single *bin* or MLT. We can also verify that the average is not a good parameter to represent the central trend of these values, it is clear that the average is above the upper quartile for all MLTs. In these cases, the median is more appropriate as a measure of the central tendency. The Figure 6.11 shows the same configuration of Figure 6.10, but for the electric field component E_{phi} . The same procedure was also made for all HSS related events. For the discussion is only pretend the figure for ICME events.

Figure 6.11 - Power Spectrum Density for the azimuthal electric field component E_{phi} at $L^* = 5.5$ and MLT sectors of 0, 6, 12 and 18 for all ICME events. The lines colored red shows the upper and lower quartile, the mean is in black and the median in blue.

E_{ϕ} Spectra in $L = 5.5 R_E$, CME Events



SOURCE: Author's production.

The median curve presented in Figures 6.10 and 6.11 shows that the noon sector tends to have power higher than the other three sectors, with no statistically significant difference in ULF wave power between the dawn, dusk, and midnight sectors. These results agree with those presented by [Ali et al. \(2016\)](#), derived from the Combined Release and Radiation Effect Satellite (CRRES) and Van Allen Probes. [Ali et al. \(2016\)](#) selected and separated the data considering only the Kp index for the events, the variation of electron flux during those events was not taking into account.

In this work, we considered the electron flux density variation and the interplanetary solar wind magnetic structures, ICME and HSS. We selected only those that may be related with flux variation in the outer radiation belt. We did not consider if there was a geomagnetic storm onset, only the interplanetary event and the flux variation was taken into account in the event selection. In comparison with [Ali et al. \(2016\)](#), our results for power spectrum density are almost four orders of magnitude. This can be related to the number of events and, in the case of [Figures 6.10 and 6.11](#). Since we separated only ICME events, generally they are able to produce high amplitude ULF waves due to the shock with magnetosphere, it may increase the median wave power spectrum.

Several authors argue that the diffusion coefficient is better estimated if we consider measurements from several positions in the same L-shell, since we can get different m-modes. To obtain the diffusion coefficient easily, some authors proposed an empirical formulation for the coefficient, and also an empirical estimate for the power spectral density associated with, considering the equations [5.12 and 5.13](#) ([OZEKE et al., 2012; OZEKE et al., 2014](#)). According to [Equations 5.9 and 5.10](#), the diffusion coefficient is proportional to the sum over all the wave modes power spectral density. Thus it is possible to compare the ability of an empirical formulation for the total power spectra to mimic the measured total power spectra in a given L-shell.

In order to perform such study of ULF in given average in the MLT values and through the L-shell, we select the median value shown in [Figures 6.10 and 6.11](#) to compute ULF waves distribution through different MLTs and L-shells. The estimation was done according to the following steps:

- select the median value of the PSD for the magnetic and electric field from each MLT bin;
- perform the average of PSD across the MLT bins (giving us the averaged spectra across the drift shell at one L-shell value);
- for each L-shell bin, integrate the drift averaged spectra over the frequency range ~ 0.4 mHz to ~ 8 mHz.

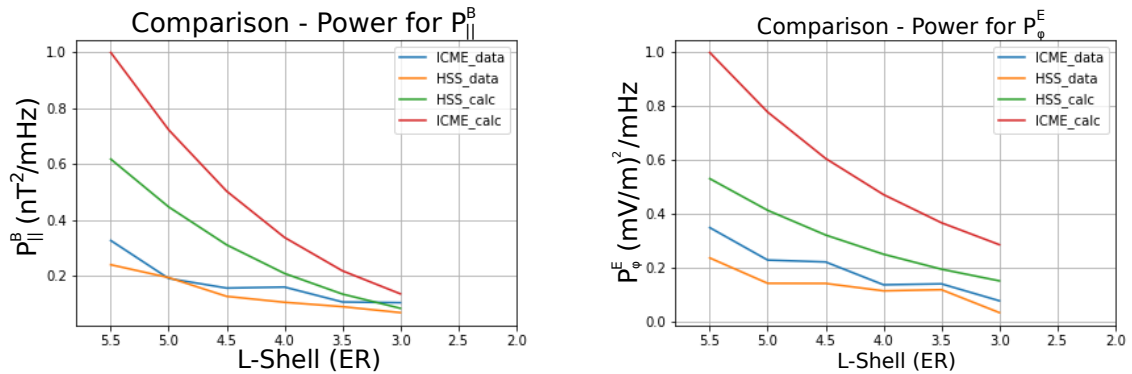
The process was done for all L-shell and MLT bins. The results are presented in [Figure 6.12](#).

[Figure 6.12](#) shows the integrated power spectrum density in the ULF frequency range for all the parallel component of the magnetic field ([Figure 6.12-left](#)) and the

azimuthal component of the electric field (Figure 6.12-right). The red and green lines are the PSD for ICME and HSS events, respectively, estimated using the Equations 5.12 and 5.13. The blue and orange lines are the ICME and HSS PSD, calculated using our approximation.

For both, magnetic and electrical component of the integrated PSD, calculated using Van Allen Probes dataset, increase for higher L-shells, as expected. Besides, for the different solar wind structures, the integrated power for ICME events is continually higher than that calculated for HSS. The comparison between the empirical estimates with the estimate using data show that the former is overestimated in both cases (magnetic power and electrical power), with a significant discrepancy for ICME.

Figure 6.12 - Drift averaged Power Spectrum Density, integrated over the frequency range ~ 0.4 mHz to ~ 8 mHz versus L-shell, for all the parallel component of the magnetic field (left) and the azimuthal component of the electric field (right). The red and green lines are the PSD for ICME and HSS events, respectively, estimated using the Equations 5.12 and 5.13. The blue and orange lines are the ICME and HSS PSD, calculated using our approximation.

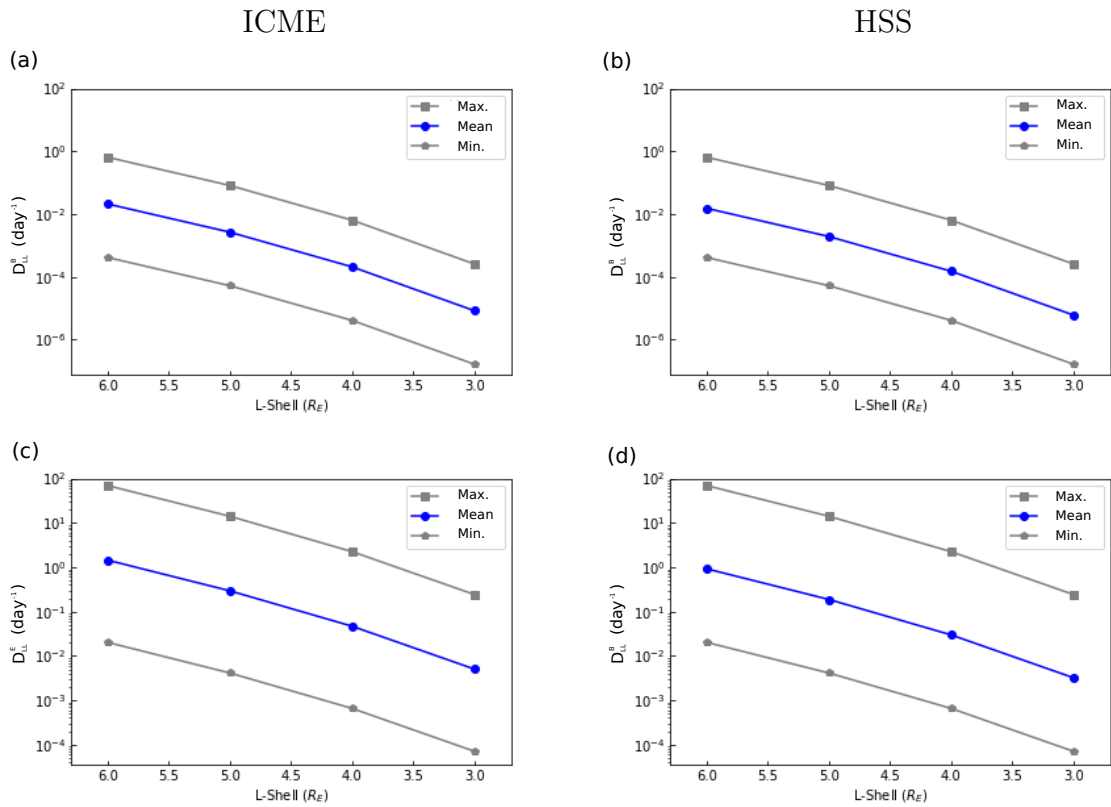


SOURCE: Author's production.

As already discussed in the Chapter 5, the calculation of the diffusion coefficients is, in most cases, based on geomagnetic indices. The most used in the literature is the one proposed by Ozeke et al. (2014), which uses the Kp index as a parameter in the calculation of diffusion coefficients. The diffusion coefficients were calculated using the Equations 5.9 and 5.10(OZEKE et al., 2014) for all the time period analyzed in

this thesis. The calculation was performed considering the Kp index during the day of each solar wind event (HSS and ICME). The D_{LL}^B and D_{LL}^E was calculated for L-shell varying from 3.0 to 6.0 R_E all this data were compiled in Figure 6.13 shows the diffusion coefficients for the compressional magnetic field and the electric field calculated for a mean value of Kp during ICME and HSS events. The blue line shows the mean value and the gray ones represent the maximum and minimum values in each L-shell.

Figure 6.13 - The diffusion coefficients calculated using Ozeke et al. (2014) equation. This is a mean value for all Kp during the period chosen for each event type. The panels on the left are for ICME events, and on the right are the HSS events. The gray lines represent the maximum and minimum values in each L-shell.



SOURCE: Author's production.

Considering Figure 6.13 the profile of the diffusion coefficients do not differ in a significant way between the events of the two solar wind structures (HSS and ICME), both for electric and magnetic components. The empirical formulation used here

estimates the power spectral density in function of Kp , it can be observed that if we assume an mean value for the geomagnetic disturbances, considering the Kp index value, the differences in the coefficients are not significant. Also, during the end period of Van Allen, the Sun was at a quiet time, and the variations on the magnetosphere were not so significant. Figure 6.12 shows a clear difference in the mean estimated PSD between the two solar wind structures, for both the calculated values and the estimate using Van Allen Probes data. It also shows an overestimate on the PSD calculated with the established empirical equations.

The statistical analysis of this work presents a framework to analyze the flux variation in the outer radiation belts, considering only the perturbation on flux to select the events and the solar wind structures involved in this process. The PSD profile versus L-shell for the HSS and ICME related events underestimate those calculated using the well established empirical equations proposed by Ozeke et al. (2014). A future approach to those results could be an estimation using solar wind parameters, such as B_z or the solar wind speed, for the two distinct solar wind structures, HSS and ICME.

7 COMPLEX CASE STUDY

On February 9, 2014, the ACE satellite detected disturbances in the plasma and interplanetary magnetic field (IMF) of the solar wind related to an Interplanetary Coronal Mass Ejection (ICME) followed by a High-Speed Solar Wind flux (HSS) event. During this period, the flux of relativistic electrons in the outer belt gradually increased.

The greatest interest is in the period in which the HSS interacts with the magnetosphere, around 18:00 UT, when the electron flux density in the outer radiation belt exhibited a gradual increase just a few hours after the arrival of the interplanetary structure. The electron flux density data was obtained by the Relativistic Electron Proton Telescope (REPT) instrument, onboard the Van Allen Probes. For this period, the Probes were located in MLT ~ 15 and $L \sim 5$. The IMF shows predominantly negative fluctuations in B_z component. The main focus here is to assess the role of each ULF wave frequency range, corresponding to Pc3, Pc4, and Pc5, in the electron acceleration of the external radiation range. Observations show an increase in the power spectrum of the ULF waves for the electric and magnetic fields in the Van Allen Probes, in electron flux density at energies of 1.80 to 3.40 MeV. That may indicate that ULF waves play a more important role in the process of accelerating this complex event.

7.1 Solar wind conditions and electron flux density

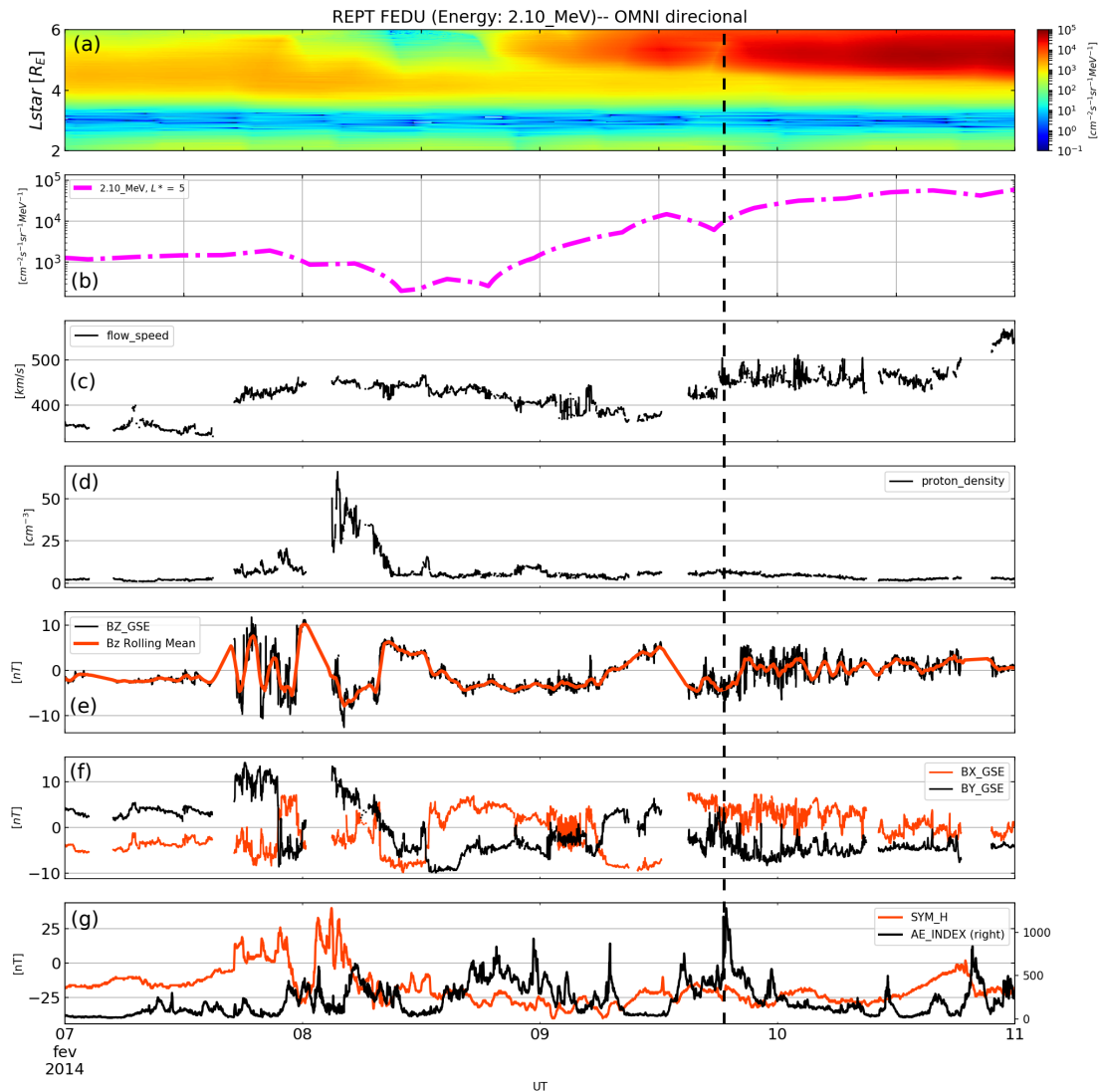
Figure 7.1 presents the electron flux density with energy of 2.10 MeV along with the parameters of the solar wind from 07 to 11 February, 2014. From top, the panel (a) presents the omnidirectional (i.e., averaged over all 17 pitch angle bins) electron flux density with energy of 2.10 MeV recorded by REPT instrument onboard the Van Allen probe A and the Roederer L , or L^* parameter (ROEDERER, 1970). (b) 2.10 MeV electron flux density at $L^* = 5.0$ RE. (c) solar wind speed; (d) solar wind proton density; (e) Interplanetary Magnetic Field (IMF) B_z component; (f) B_x and B_y component of the IMF recorded by the Advanced Composition Explorer (ACE) satellite in the Lagrangian L1 point. Panel (g) shows the auroral activity index, AE and the ring current index, SYM-H. The vertical dashed line shows the time of the enhancement on flux and the increase on solar wind speed coincident to the substorm expansion onset.

The beginning of the period, between the 8th and 9th of February, is characterized by the interaction between a complex solar wind structure. The Earth's magnetosphere

is on the effect of the interaction between a interplanetary coronal mass ejection followed by a solar wind High-Speed Stream these structures can be seen in panels (c) - (e) of Figure 7.1, where an increase in solar wind speed, from $\sim 350 \text{ km s}^{-1}$ to $\sim 450 \text{ km s}^{-1}$, is followed by an increase in solar wind proton density. The three components of the interplanetary magnetic field also show significant fluctuations. The electron flux density at this point was at low levels, specially at L^* higher than $4 R_E$. At the end of February 7 and beginning of February 8, with the arrival of the ICME, we can note, in panels (a) and (b) an slight decrease in the REPT's electron flux density at L^* greater than $\sim 5 R_E$ in two steps: first a small reduction, at the same time, solar wind speed increases and the IMF components present high fluctuations; and another decrease on flux more abrupt when there is an peak on solar wind proton density, the time when the ICME shock reaches the Earth's magnetosphere. A few hours later, the flux value returns to what it was before the structure arrived.

After this first perturbation, at the second half portion of February 08 and the beginning of February 09, a gradual increase in flux density is noted, concomitant with a period in which the average component B_z of the IMF remains southward ($B_z < 0$) for a few hours, then turns positive ($B_z > 0$) as the components B_x and B_y presents rapid variations, and it is a sector boundary crossing with reversals in the polarity of their magnitudes. The auroral activity remains high as one can see in panel (g) of Figure 7.1 during the period were B_z is southward and there is correlated with the flux enhancement. Right after the period with southward B_z turns to north direction ($B_z > 0$), when the flux (Figure 7.1-b) reaches an local maximum and then has a small reduction. After this local minimum we can observe a graduall enhancement in the electron flux at $L^* = 5.0 R_E$. The enhancement is followed by an increase in the solar wind speed (Figure 7.1-c) and the auroral index AE (Figure 7.1-g).

Figure 7.1 - From top: (a) Electron flux density at 2.10 MeV energy as a function of L^* (vertical axes) and time (horizontal axis); (b) 2.10 MeV electron flux density at $L^* = 5.0ER$; (c) solar wind speed; (d) solar wind proton density; (e) Interplanetary Magnetic Field (IMF) B_z component; (f) B_x and B_y component of the IMF. The electron fluxes are obtained by the REPT instrument on board of the Van Allen Probes The flux speed, Density, B_z , B_x and B_y are obtained by the Advanced Composition Explorer (ACE) satellite in the Lagrangian $L1$ point. Panel (f) shows the auroral activity index AE and the SYM-H index. The vertical dashed line shows the time of the enhancement on flux and the increase on solar wind speed coincident to the substorm expansion onset.

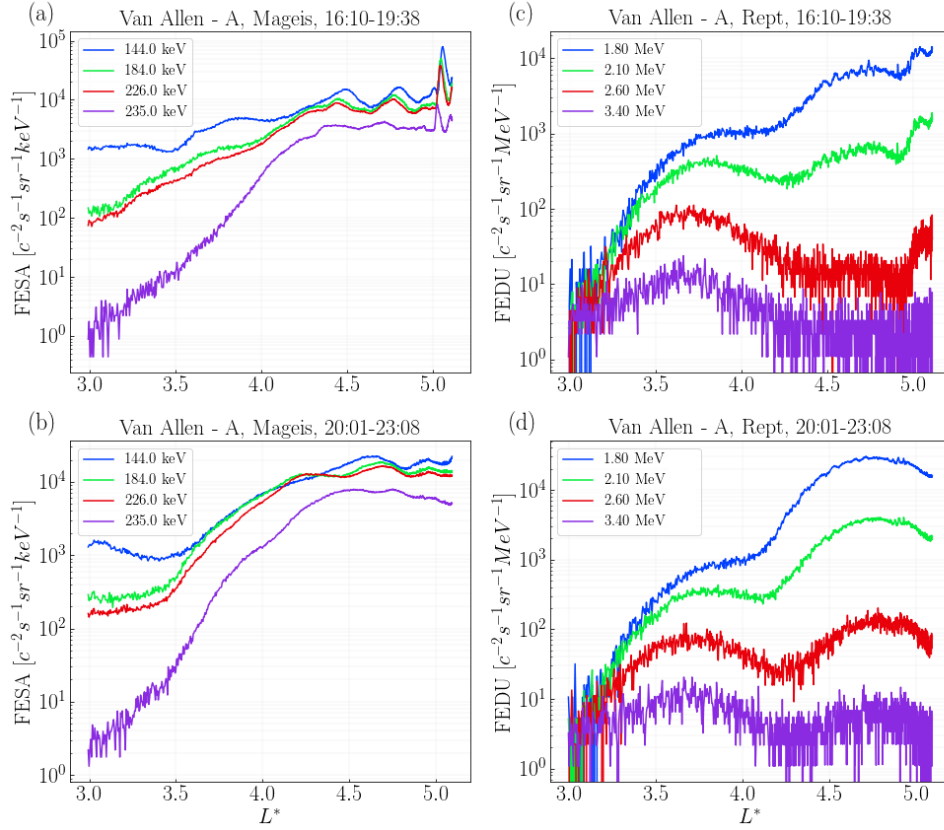


SOURCE: Author's production.

A prolonged interval with southward B_z and low-frequency fluctuations in the solar wind, or Alfvénic fluctuations (LEE et al., 2006; ZHANG et al., 2014) can initiate reconnection on the Earth’s dayside magnetopause, which allows solar wind energy to enter the magnetosphere and drive moderate-intensity geomagnetic storms (GONZALEZ et al., 1994; TSURUTANI et al., 1995) and recurrent substorms. The arrival of such structures can generate a range of magnetospheric oscillations, among them, ULF wave modes, which are known as an efficient mechanism on the transport of seed population particles responsible for outer radiation belt recovery (ELKINGTON et al., 1999; SUMMERS; MA, 2000; HORNE et al., 2005; ELKINGTON, 2006; OZEKE et al., 2014). Generally, seed population, a name given to the injection of low-energy particles into the magnetosphere, comes from the plasma sheet, due to storms and increased convection in these regions (BAKER et al., 1996; GANUSHKINA et al., 2013; TANG et al., 2016). This work aims to investigate the ULF waves contribution on the particles radial diffusion related to the perturbations on the magnetosphere, specially after the 18 : 30 UT on February 09, marked with the dashed line in Figure 7.1. The period, as mentioned before, is perturbed by an substorm activity and Alfvénic fluctuations in the solar wind.

Figure 7.2 shows the electron flux density in the probe’s orbit profile. Panels (a) and (b) are the measurements for low energy particles (keV) recorded by MagEIS instruments. Panels (c) and (d) show the REPT instrument measurements for high-energy and relativistic electrons (MeV). The y-axis are the flux density and the x-axis of the panels show the Roeders parameter L^* from 3 to 5.3 R_E . Panels (a) and (b), left side of the figure, show the measurements made by the MagEIS instrument for different energies, 144 keV, 184 keV, 226 keV and 235 keV. On the right side, panels (c) and (d) show the relativistic electron flux density, with energies 1.8 keV, 2.1 keV, 2.6 keV and 3.4 MeV, recorded by the REPT instrument, both onboard the Van Allen probe A. The upper part of figure, panels (a) and (c) correspond to the period between 16 : 10 and 19 : 38 UT for February 9, (a) presents the measurements in low energy, and (c) the measurements of the relativistic electrons. The lower half, panels (b) and (d), follow the same pattern for energies, but for another time, from 20 : 01 to 23 : 08 UT.

Figure 7.2 - Flux density for low energies, panels (a) and (b), in the energy channels of 144 keV, 184 keV, 226 keV and 235 keV measured by the MagEIS instrument. The panels (c) and (d) the channels at higher energies, 1.8 MeV, 2.1 MeV, 2.6 MeV and 3.4 MeV registered by REPT instrument, both onboard Van Allen Probe A.



SOURCE: Author's production.

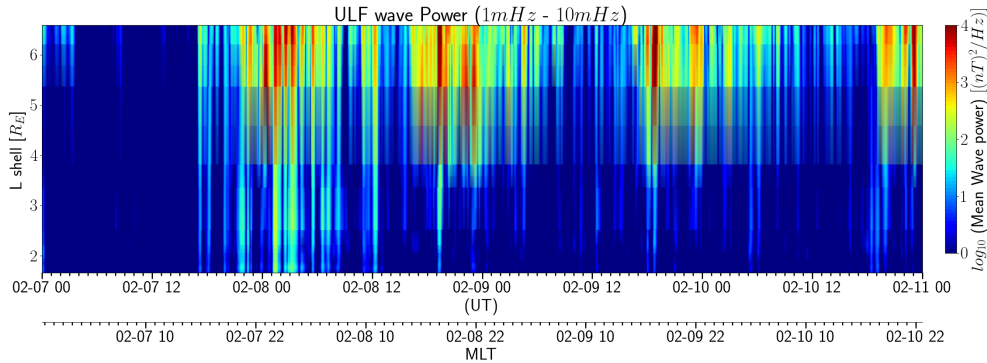
For both time intervals, the probe covers practically the same values of L^* , so we can compare the flux conditions before the lower energy particle injection and the orbit after that. In the first orbit portion (Figure 7.2, panels (a) and (c)) we can see an increase in flux at lower energies at $L \sim 5 E_R$ in panel (a). Panel (d) shows an increase in the flux of relativistic electrons when compared to the previous orbit portion, in panel (c). During the first orbit portion, the high energy flux, panel (c), has slight increased values mainly in the flux of electrons with 1.80 and 2.10 MeV.

In the subsequent orbit, panel (d), the flux of those particles increase in almost one order of magnitude. This enhancement is observed in the Figure 7.1-a,b for 2.10 MeV electrons, the enhancement also occurs for the 1.8 MeV, 2.6 MeV and 3.4 MeV. The period is disturbed by a strong sub-storm, as shown in Figure 7.1-g. The abrupt enhancement on low energy, at around 1830 UT, in Figure 7.2-a can be injection of seed population into the outer radiation belt, at $L^* = 5$ ER associated with this substorm activity.

Several physical mechanisms act to alter the dynamics of the outer radiation belt electrons. Among these mechanisms, it is considered that the activity of ULF waves has a great impact on the energy transfer to the particles, promoting particle diffusion to both inward and outward through the magnetosphere and may also cause the particles to accelerate. Those waves can be generated by the interaction of short fluctuation in solar wind parameters (density, velocity, and dynamic pressure) with the magnetosphere with similar periods, whether or not substorms occur (KEPKO et al., 2002; KEPKO; SPENCE, 2003).

Figure 7.3 shows the spectral power density calculated by the Morlet wavelet transform, from 07 to 11 February 2014 using observations from the IMAGE ground-based magnetometer network. The instrument's signal was filtered using a Butterworth band-pass filter, which only allows the passage of signals within the Pc5 frequency range (1 – 10 mHz). The spectral power was integrated within the mentioned frequency range for each station of the IMAGE network, located at longitudes close to the 110° meridian, in the northern hemisphere. This representation allows seeing this wave power with the depth in the magnetosphere, represented by the parameter of McIlwain L , the y-axis of the Figure 7.1.

Figure 7.3 - The power spectrum of ULF waves, within the frequency range between 1 to 10 mHz using data from the magnetometer network on the Earth's surface, IMAGE as a function of the McIlwain parameter, L-shell and time (UT and MLT) between the 7th until the 11th of February 2014.



SOURCE: Author's production.

Note that during almost the whole day of February 7th, the activity of ULF waves recorded on the ground was very low, almost without disturbances. Around 17:00h UT there is an impulsive signal, and the spatial coverage extends through low L-shell values, this increase co-occurs with the abrupt increase in the speed of the solar wind shown in Figure 7.1-c. The wave activity continues with high intensities until midday of the 8th. The wave activity intensifies, with a period of more significant intensity concomitant with the increase in proton density and the negative IMF B_z component (Figure 7.1, d-e). The second interval with wave activity relates to the change in polarity of the B_x and B_y components of the IMF and the injection observed in Figure 7.2 occurs, around 18 : 30 UT at February 09. The wave power spectrum time duration in this last period is short, around 2 hours, but the intensity is high and reaches lower l-shell values.

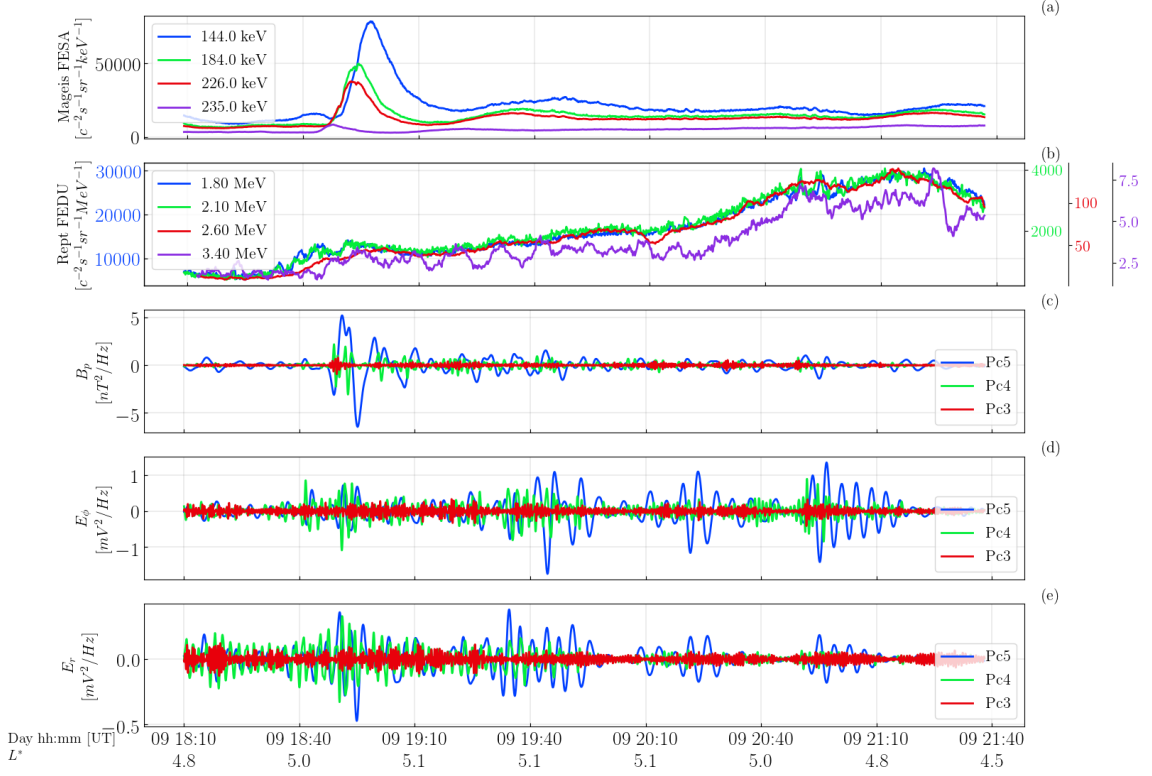
The electron flux density during February 09 increases gradually concurrent with the ULF wave activity increase. Also, the electron flux variations happens at the L-shell locations where the ULF activity is predominant. The IMF conditions suggest enhanced substorm activity, which is confirmed by the maintenance of intense auroral activity seen in Figure 7.1-g. In the Chapter 6 we showed that on the average, flux enhancement events related to High-Speed Streams are linked to prolonged auroral and substorm activity that may lead on low energy injection that will further be transported by ULF waves.

The role of ULF waves in the acceleration processes is still not well understood. It may occur in conjunction to another frequency waves that can increase the particles energy and than the ULF waves can act on the transportation through inward radial diffusion process driven by drift resonant interactions (ELKINGTON, 2006; UKHORSKIY et al., 2005). The polarization modes can affect the efficiency of wave-particle interactions. Interactions with waves in the azimuthal direction of electric fields, the resulting in poloidal modes are likely to be more effective to radiation belt dynamics than are interactions relying on the radial component of the electric field (ELKINGTON, 2006).

We applied a Butterworth band-pass filter to the EMFISIS magnetic field and EFW electric field measurements. The ULF wave modes are characterized as fast (compressional), poloidal, and toroidal according to the predominant PSD component, that is, magnetic parallel (B_{\parallel}), electric azimuthal (E_{ϕ}), and electric radial (E_r), respectively. To identify the polarization modes of the ULF waves, we rotate the electric and magnetic field vectors into the field-aligned coordinate system as explained in Chapter 5.

The Figure 7.4 shows the rapid increase in the flux of low-energy electrons, presented in Figure 7.2, focusing on a sudden increase in electrons with energies of up to 342 keV, those particles can be directly related to an increase in seed population in the outer belt and can contribute to the increase of relativistic electrons in that region. We can observe that the signal of the ULF waves in the frequencies of Pc4 and Pc5 presents a substantial increase in amplitude at the same moment that there is a sudden increase in the flux at low energies. These waves have a distinct shape in wave packets, similar to continuous geomagnetic pulsations (SAMSON, 1991). This signal can be seen in the components B_{\parallel} and in the electric fields E_{ϕ} and E_r in the first instance where there is a sudden increase. This signal lasts in the E_{ϕ} and E_r components for the next few hours, along with the increased flux at high energies.

Figure 7.4 - (a) MagEIS electron flux density, energies range from 144 keV to 235 keV. (b) Flux of relativistic electrons from the REPT instrument, energies from 1.8 MeV to 3.4 MeV. (c), (d) and (e) present the ULF signal filtered in the frequency bands Pc3, Pc4 and Pc5 for the B_p component of the geomagnetic field, and for the E_ϕ and E_r components of the electric field.



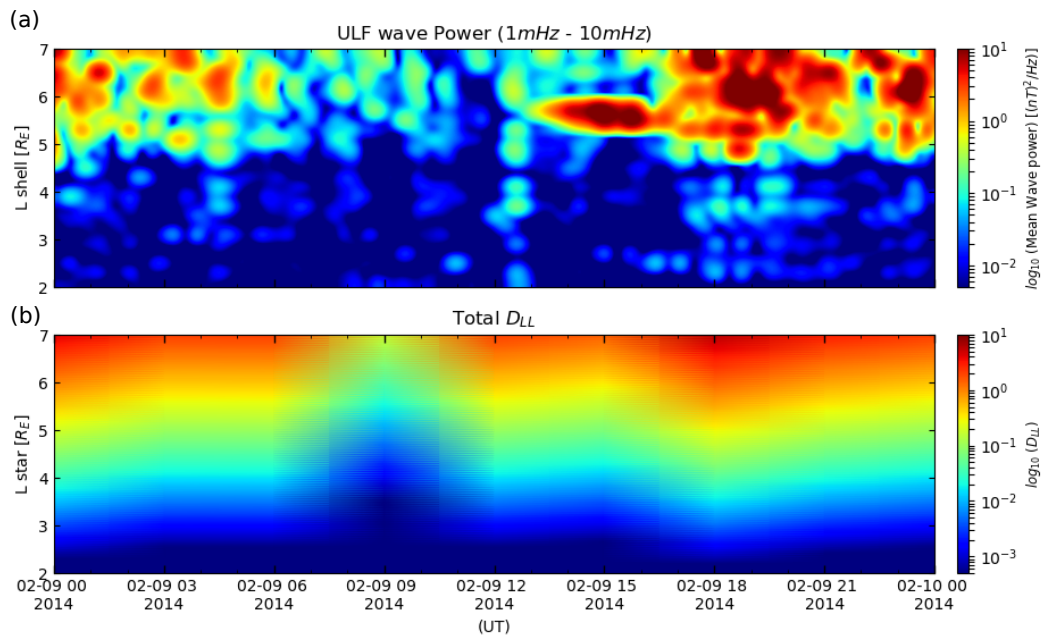
SOURCE: Author's production.

In Figure 7.4 we can note that the signal of ULF waves on the azimuthal component of the electric field (E_ϕ) is more significant than the radial component. Since the azimuthal component is more effective on the electron acceleration via diffusion process, it may indicate that those waves can be acting on the diffusion of the particle content.

The efficiency of drift-resonant ULF wave-particle interactions can be estimated employing an model for the radial diffusion coefficient D_{LL} (see *e.g.*, (OZEKE et al., 2012; OZEKE et al., 2014; ALI et al., 2016)). Here we used the empirical model developed

by Ozeke et al. (2014) (equations 5.12 and 5.13) using as parameters the Kp index and L-shell.

Figure 7.5 - (a) Ultralow-frequency (ULF) power spectral density in the 1 to 10 mHz frequency range (color scale) as a function of L-shell and time, during 9 February 2014. (b) Radial diffusion coefficient D_{LL} (color scale) as a function of L-shell (vertical axis-left) and time (horizontal axis) during 9 February 2014.



The calculation was estimated using the equation proposed by Ozeke et al. (2014), using the Kp index provided by the German Geosciences Research Center (GFZ-Potsdam).

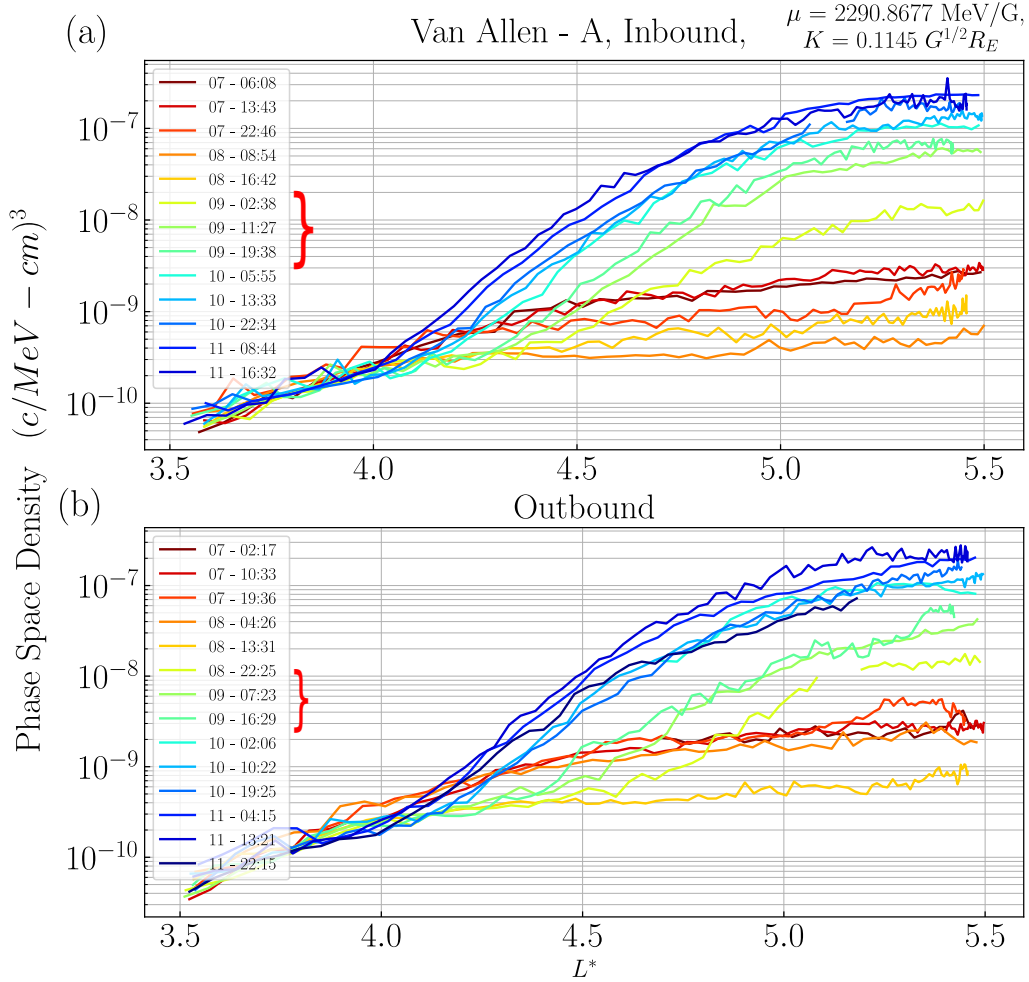
SOURCE: Author's production.

Figure 7.5 show, in the panel (a), the ULF power spectral density in the 1 to 10 mHz frequency range during 9 February 2014 and the panel (b) shows the corresponding D_{LL} coefficient. The ULF wave PSD was calculated using observations from the IMAGE network and the D_{LL} was calculated applying the Equations 5.12 and 5.13. The time evolution of D_{LL} shows an increase in the coefficients coincident with ULF PSD around 1800 UT. It is interesting to note that there is a high wave power around midday and L-shell $\sim 5 R_E$, but the D_{LL} is not influenced. Only around the time where there is an injection and after an enhancement on high energy electrons that the D_{LL} increase its intensity and L-shell coverage.

The evaluation of phase space density (PhSD) is essential for understanding how ULF waves are acting to contribute to the increase in the flux of relativistic electrons. It is a tool to distinguish whether diffusive processes are relevant to local acceleration processes with interaction in other higher frequency ranges. PhSD is calculated using quantities that are conserved under specific circumstances, for example, the three adiabatic invariants that constrain the electron motion: μ , related to the particle motion around the magnetic field line; K , related to the bouncing motion between magnetic mirrors and the Roederer parameter L^* (ROEDERER, 1970), related to the particle drift around the magnetosphere, as explained on Section 5.6.

Figure 7.6 shows the temporal evolution of the PhSD, for fixed values of the invariant μ and K for the orbit portions of the probe in which it is approaching and moving away from Earth. The legend in Figure 7.6 shows the moments of the beginning of the orbit portions, ranging from the 7th to the 11th of February, covering L values from 2.5 to 5.5 ER.

Figure 7.6 - Temporal evolution of the radial profile of the phase space density to fixed values of the adiabatic invariants μ and K . The legend shows the start times of the orbit portions of the Van Allen A.



SOURCE: Author's production.

The evolution of the radial PhSD shows an positive gradient, at L^* larger than $\sim 4.5 R_E$. If we look to the PhSD for inbound and outbound portions, specially at the beginning times marked with the red brackets, the PhSD at fixed μ and K increases almost two orders of magnitude. The inward radial diffusion can be inferred looking to the panel (b) of Figure 7.6 where the PhSD starts to increase at the orbit portion beginning at 06 : 53 UT of 9 February and there is a small shift in L^* in

the subsequent orbit intervals. The inward orbit portions, panel (a) of Figure 7.6, also presents a positive gradient on PhSD. Taking into account the Figure 5.8, the analysis of the time evolution of the radial PhSD may indicate that there is a radial diffusion that can transport the electrons through the outer radiation belts.

The event on 09 February 2014 occurred during strong substorm. The enhancements of the seed populations were directly caused by substorm electron injections. Due to the intense substorm electric fields during the event, the characteristics of substorm electron injections were observed by Van Allen Probe A. The energies of these electrons that were injected into the heart of the outer radiation belt were up to 342 keV. The rapid enhancements of the seed populations could contribute to enhancements of relativistic electrons in the heart of the outer radiation belt (Figure 7.1-a).

In summary, the D_{LL} analysis of Figure 7.5 and the PhSD time evolution profile showed in Figure 7.6 agree with enhancement on high energy electrons followed by the particle injection at 18 : 30 UT of February 09 and the ULF waves activity recorded on the ground during that day, also the ULF waves activity recorded by Van Allen Probes shows a correlation between the oscillation in the E_ϕ component and the enhancements, which may be related to the radial diffusion caused by those waves.

8 CONCLUSIONS

The main objective of this work was to give a description, of the radial diffusion mechanism due to ULF waves, acting on the outer radiation belt particles flux, using ground measurements and in situ observational data. To do that, it was performed the description of ULF waves in the frequency bands corresponding to the natural oscillations of the magnetosphere, i.e. Pc4 and Pc5 ULF frequency range, observed in the region of external radiation belt, during periods of increased relativistic electron flux density in the external radiation belt. In order to perform this description we carried out a survey of the HSS and ICME events during the Van Allen Probes program, October 2014 to December 2018. The events were selected based on the Richardson List, for ICME and the DONKI repository, in case of HSS events. The criteria used for filtering the ICME events was based on the occurrence or not of Magnetic Cloud in the structure, the feature is marked on the Richardson List. For HSS the criteria was to be detected by WIND or ACE Satellites, which can ensure the interaction with Earth's magnetosphere a few time after the detection.

The electron flux density variation in the radiation belts was divided into those that can be related to HSS events and those to ICME. We split the reduction related events and the enhancements on the 2.10 MeV electrons, detected at L-shell= 5 R_E . We applied the SEA on those data based, defining the zero-epoch as the time were a small reduction on flux occur. We also performed the SEA for all Solar Wind parameters at the same instant. Here we presented a new framework to analyze the outer radiation belt flux density variation: to look on the minimum electron flux density in order to set a common time to compare all the related events. For all selected events we separate the compressional component of the magnetic field, measured by EMFISIS instrument on board Van Allen Probes and applied an Butterworth filter in order to get only the signal corresponding to the Pc4 and Pc5 frequency spectra. An wavelet transform was applied to get the power spectral density and then the SEA was applied to estimate the average behavior of the spectral power integrated in the frequency range during the periods of analysis to compare the events. The Wavelet spectra was integrated over the L-shell and MLT interval to calculate an estimated PSD over the HSS and ICME periods. The D_{LL} was calculated using the empirical equation by [Ozeke et al. \(2014\)](#). Also, the power spectral density was estimated using the Equations 5.12 and 5.13 and compared with the estimate using all data from Van Allen probes separated into the interplanetary events (HSS and ICME).

The SEA showed that the enhancement events, due to ICME, are characterized by an intense solar wind dynamic pressure and strong B_z with negative values. Those factors are an good indicative of geomagnetic storm onset. The solar wind speed has an increase, on average, less than 100 km/s. Together with the southward B_z and the solar wind dynamic pressure, it can disturb the magnetosphere. For HSS events, the most significant region in reduction events, is at $L > 4.5$ and, it starts to decay gradually. After the t_0 , the flux remains at low value for all period, on average. The region between $3.5 - 4.5 R_E$ show a flux reduction as well, and remains with the amount of particles during the period.

The SEA applied to the Power Spectrum density for the compressional magnetic field registered by EMFISIS instrument shows a clear distinction in the mean ULF activity associated to ICME (Figure 6.8) and HSS (Figure 6.9) and also between enhancement related events from depletion related ones. In both for HSS and ICME cases, the wave amplitude are smaller for depletion. Also, the duration of ULF wave activity is different between enhancement and depletion events, both for ICME and HSS. For enhancements, the wave power lasts longer. Also, for HSS the wave duration is even longer, lasts for days. In the ICME events the maximum wave power peak appears earlier at higher L-shell.

We list the main results from this thesis and their contribution to the radiation belt scientific field:

- 1- Statistical Analysis of the outer radiation belt following an ICME arrival observed at L-shell 5, show that, on average:
 - The average ICMEs parameters related to flux enhancement are: solar wind velocity in the Earth vicinity around 450 km/s; dynamic pressure peaks at 10 nPa and $B_z < -8$ nT. Besides, solar wind speed is sustained increased for a couple of days after the arrival;
 - The outer radiation belt flux shows a fast decrease, around 5 hours after both the solar wind dynamic pressure and southward magnetic field component peak;
 - The flux growth undergo roughly 30 hours to reach its maximum, the solar wind speed increases through this period and B_z component oscillates;
 - Magnetospheric convection and substorms can be related to AE index and show to be higher than 500 nT through 50 hours after the ICME

- arrival;
- ULF waves are analyzed in this context using SEA based only in Van Allen Probes dataset, PSD is increased throughout the first 20h after the ICME arrival;
- ULF PSD is observed to increase also deep magnetosphere, such as $L = 4$;
- The average ICMEs parameters related to the cases with a persistent decrease in the flux are: solar wind speed in the Earth vicinity around > 450 km/s; dynamic pressure peaks at 6 nPa and B_z is around -5 nT. Besides, solar wind speed tends to decrease as a function of time;
 - The outer radiation belt flux decrease slow;
 - The outer radiation belt flux persists at low values in the same time interval that solar wind speed decreases and B_z component oscillates around zero;
 - Magnetospheric convection and substorms can be related to AE index and show to be slightly increased before the ICME arrival but always lower than 500 nT through 50 hours after the ICME arrival;
 - ULF waves do not show, on average, any typical tendency when related to flux decrease in the magnetospheric outer region. However, inner magnetosphere ($L \leq 4$) PSD is increased as the ICMEs arrive;

2- Statistical Analysis of the outer radiation belt following an HSS arrival observed at L-shell 5, show that, on average:

- The average HSS parameters related to flux enhancements are: solar wind speed in the Earth's vicinity around 550 Km/s, dynamic pressure peaks at around 4.5 nPa and $B_z < -2$ nT. The solar wind speed remains high few days after the structure arrival, and reaches a maximum at about 2 days after when starts to decrease;
 - The flux gradually increases, coincident to the solar wind speed enhancement, and the average southward B_z ;
 - The flux increases and reaches a plato after ~ 3 days after the structure arrival;
 - Magnetospheric convection and substorm activity represented by AE index present values higher than 450 nT until almost 60 hours after the arrival;
 - The AE index higher values are coincident to the flux increase;

- The average ULF wave activity analyzed under the SEA approach, increases at the first 24 hours after the arrival and remains at elevated amplitudes for 3 to 4 days after;
- The ULF waves present a similar behavior also deep in the magnetosphere, down to $L = 3.5 R_E$;
- For the cases with flux decrease, the HSS parameters on average are: solar wind speed in the Earth’s vicinity less than ~ 450 Km/s, the dynamic pressure peaks at around 3 nPa and B_z around zero. The high values of solar wind speed remains elevated during almost all analyzed period after the structure arrival;
 - The electron flux content decrease is fast;
 - The average electron flux density decreases and remains at the reduced value for all analyzed period;
 - The magnetospheric convection and substorm activity presents an small increase when the structure arrives and rapidly returns to the normal value bellow 100 nT;
 - ULF waves do not show significant activity related to flux decrease.

3- Integrated PSD for $B_{||}$ and E_{ϕ} show:

- ULF waves contribution is very similar for ICMEs and HSS events;
- The integrated PSD for $B_{||}$ presents the same value in ICMEs and HSS events at $L = 5 R_E$;
- Empirical models applied to quantify integrated power overestimate the power measured in all L-shells.

Besides, the study case analyzed the ULF contribution to the enhancement and electron flux density during a complex event involving an ICME and HSS that happened between 08 and 09 February 2014. The flux was reduced immediately after the ICME reaches the magnetosphere and in the subsequent hours the 2.10 MeV starts to increase gradually. The enhancement periods are coincident with a predominant B_z southward and the IMF components presents Alfvénic fluctuations. The southward B_z contributed to provide energy input to the Earth’s inner magnetosphere via dayside reconnection, which in turn may drive enhanced substorm activity. The substorms are known to produce injection of low energy particles that can be turned on seed population and can be transported to the radiation belts. The D_{LL} analysis (Figure 7.5) and the PhSD time evolution profile (Figure 7.6) agree

with enhancement on high energy electrons followed by the particle injection at 18 : 30 UT of February 09. The ULF waves activity recorded on the ground during that day and the ULF waves activity recorded by Van Allen Probes show correlation between the oscillation in the E_ϕ component and the high energy electron flux density enhancements, which may be related to the radial diffusion caused by those waves.

Future Perspectives of Work

We think that this work is an important continuation of what has been done so far for the study and prediction of the Van Allen radiation belts electron content. This work provides a new approach and framework to select and analyze flux variations in the outer belt related to different solar wind structures.

As future work, we suggest to continue this study, considering the different solar wind structures, adding the lower energy channels from Van Allen Probes in the statistical analysis. This will help us to see the relation between low energy particles that can be accelerated and transported to the heart of radiation belts due to ULF waves radial diffusion processes.

We also suggest to estimate the diffusion coefficients, based on the equation proposed by Fei et al. (2006), considering the interplanetary parameters, such as B_z and solar wind speed. Also include the contribution of higher Pc frequency bands and formulate an empirical equation that takes into account the different solar wind structures (HSS and ICME).

REFERENCES

ALI, A. F.; MALASPINA, D. M.; ELKINGTON, S. R.; JAYNES, A. N.; CHAN, A. A.; WYGANT, J.; KLETZING, C. A. Electric and magnetic radial diffusion coefficients using the van allen probes data. **Journal of Geophysical Research: Space Physics**, v. 121, n. 10, p. 9586–9607, 2016. 80, 81, 93

ALVES, L. R.; SILVA, L. A. D.; SOUZA, V. M.; SIBECK, D. G.; JAUER, P. R.; VIEIRA, L. E. A.; WALSH, B. M.; SILVEIRA, M. V. D.; MARCHEZI, J. P.; ROCKENBACH, M.; LAGO, A. D.; MENDES, O.; TSURUTANI, B. T.; KOGA, D.; KANEKAL, S. G.; BAKER, D. N.; WYGANT, J. R.; KLETZING, C. A. Outer radiation belt dropout dynamics following the arrival of two interplanetary coronal mass ejections. **Geophysical Research Letters**, v. 43, n. 3, p. 978–987, 2016. Available from: <<https://agupubs.onlinelibrary.wiley.com/doi/abs/10.1002/2015GL067066>>. 2, 29, 42

ALVES, L. R.; SOUZA, V. M.; JAUER, P. R.; SILVA, L. A. da; MEDEIROS, C.; BRAGA, C. R.; ALVES, M. V.; KOGA, D.; MARCHEZI, J. P.; MENDONÇA, R. R. S. de; DALLAQUA, R. S.; BARBOSA, M. V. G.; ROCKENBACH, M.; LAGO, A. D.; MENDES, O.; VIEIRA, L. E. A.; BANIK, M.; SIBECK, D. G.; KANEKAL, S. G.; BAKER, D. N.; WYGANT, J. R.; KLETZING, C. A. The role of solar wind structures in the generation of ulf waves in the inner magnetosphere. **Solar Physics**, v. 292, n. 7, p. 92, Jun 2017. ISSN 1573-093X. 42

ARTEMYEV, A.; AGAPITOV, O.; MOURENAS, D.; KRASNOSELSKIKH, V.; ZELENYI, L. Storm-induced energization of radiation belt electrons: effect of wave obliquity. **Geophysical Research Letters**, v. 40, n. 16, p. 4138–4143, 2013. 2, 29

ASCHWANDEN, M. J. The sun. In: SPOHN, T.; BREUER, D.; JOHNSON, T. V. (Ed.). **Encyclopedia of the solar system**. 3.ed.. ed. Boston: [s.n.], 2014. p. 235 – 259. ISBN 978-0-12-415845-0. Available from: <<http://www.sciencedirect.com/science/article/pii/B9780124158450000116>>. 7

BAKER, D.; LI, X.; BLAKE, J.; KANEKAL, S. Strong electron acceleration in the earth's magnetosphere. **Advances in Space Research**, v. 21, n. 4, p. 609–613, 1998. 70

BAKER, D. N. Satellite anomalies due to space storms. In: _____. **Space storms and space weather hazards**. [S.l.: s.n.], 2001. 1

BAKER, D. N.; JAYNES, A. N.; LI, X.; HENDERSON, M. G.; KANEKAL, S. G.; REEVES, G. D.; SPENCE, H. E.; CLAUDEPIERRE, S. G.; FENNELL, J. F.; HUDSON, M. K.; THORNE, R. M.; FOSTER, J. C.; ERICKSON, P. J.; MALASPINA, D. M.; WYGANT, J. R.; BOYD, A.; KLETZING, C. A.; DROZDOV, A.; SHPRITS, Y. Y. Gradual diffusion and punctuated phase space density enhancements of highly relativistic electrons: Van allen probes observations. **Geophysical Research Letters**, v. 41, n. 5, p. 1351–1358, 2014. [2](#), [29](#)

BAKER, D. N.; KANEKAL, S. G.; HOXIE, V. C.; BATISTE, S.; BOLTON, M.; LI, X.; ELKINGTON, S. R.; MONK, S.; REUKAUF, R.; STEG, S.; WESTFALL, J.; BELTING, C.; BOLTON, B.; BRAUN, D.; CERVELLI, B.; HUBBELL, K.; KIEN, M.; KNAPPMILLER, S.; WADE, S.; LAMPRECHT, B.; STEVENS, K.; WALLACE, J.; YEHLE, A.; SPENCE, H. E.; FRIEDEL, R. The relativistic electron-proton telescope (rept) instrument on board the radiation belt storm srobes (rbsp) spacecraft: characterization of earth's radiation belt high-energy particle populations. In: _____. **The Van Allen probes mission**. [S.l.: s.n.], 2014. [33](#)

BAKER, D. N.; PULKKINEN, T.; ANGELOPOULOS, V.; BAUMJOHANN, W.; MCPHERRON, R. Neutral line model of substorms: past results and present view. **Journal of Geophysical Research: Space Physics**, v. 101, n. A6, p. 12975–13010, 1996. [88](#)

BAME, S.; ASBRIDGE, J.; FELDMAN, W.; GOSLING, J. Solar cycle evolution of high-speed solar wind streams. **The Astrophysical Journal**, v. 207, p. 977–980, 1976. [13](#)

BARFIELD, J. N.; MCPHERRON, R. L. Statistical characteristics of storm-associated pc 5 micropulsations observed at the synchronous equatorial orbit. **Journal of Geophysical Research**, v. 77, n. 25, p. 4720–4733, 1972. ISSN 2156-2202. [3](#)

BAUMJOHANN, W.; TREUMANN, R. A. **Basic space plasma physics**. [S.l.: s.n.], 1997. [2](#), [8](#), [16](#), [22](#), [23](#), [26](#), [27](#), [28](#)

BIERMANN, L. The plasma tails of comets and the interplanetary plasma. **Space Science Reviews**, v. 1, n. 3, p. 553–553, 1963. ISSN 0038-6308. [8](#)

BLAKE, J. B.; CARRANZA, P. A.; CLAUDEPIERRE, S. G.; CLEMMONS, J. H.; CRAIN, W. R.; DOTAN, Y.; FENNELL, J. F.; FUENTES, F. H.;

GALVAN, R. M.; GEORGE, J. S.; HENDERSON, M. G.; LALIC, M.; LIN, A. Y.; LOOPER, M. D.; MABRY, D. J.; MAZUR, J. E.; MCCARTHY, B.; NGUYEN, C. Q.; O'BRIEN, T. P.; PEREZ, M. A.; REDDING, M. T.; ROEDER, J. L.; SALVAGGIO, D. J.; SORENSEN, G. A.; SPENCE, H. E.; YI, S.; ZAKRZEWSKI, M. P. The magnetic electron ion spectrometer (mageis) instruments aboard the radiation belt storm probes (rbsp) spacecraft. **Space Science Reviews**, v. 179, n. 1, p. 383–421, Nov 2013. ISSN 1572-9672. 33

BOLZAN, M. J. A. Transformada em ondeleta: uma necessidade. **Revista Brasileira de Ensino de Física**, v. 28, p. 563 – 567, 00 2006. ISSN 1806-1117. 43

BOROVSKY, J. E.; DENTON, M. H. Differences between cme-driven storms and cir-driven storms. **Journal of Geophysical Research: Space Physics**, v. 111, n. A7, 2006. 12

_____. Relativistic-electron dropouts and recovery: a superposed epoch study of the magnetosphere and the solar wind. **Journal of Geophysical Research: Space Physics**, v. 114, n. A2, 2009. 41

BORTNIK, J.; THORNE, R. The dual role of elf/vlf chorus waves in the acceleration and precipitation of radiation belt electrons. **Journal of Atmospheric and Solar-Terrestrial Physics**, v. 69, n. 3, p. 378–386, 2007. 2

BORTNIK, J.; THORNE, R.; O'BRIEN, T.; GREEN, J.; STRANGEWAY, R.; SHPRITS, Y.; BAKER, D. Observation of two distinct, rapid loss mechanisms during the 20 november 2003 radiation belt dropout event. **Journal of Geophysical Research: Space Physics**, v. 111, n. A12, 2006. 59

BORTNIK J; THORNE, R. The dual role of elf/vlf chorus waves in the acceleration and precipitation of radiation belt electrons. **Journal of Atmospheric and Solar-Terrestrial Physics**, v. 69, n. 3, p. 378–386, 2007. 29

BOSCHER, D.; BOURDARIE, S.; O'BRIEN, P.; GUILD, T. **IRBEM library V4. 3, 2004-2008, ONERA-DESP**. 2010. 55

BOTHMER, V.; DAGLIS, I. A. **Space weather: physics and effects**. [S.l.: s.n.], 2007. 8, 25

BOYNTON, R.; MOURENAS, D.; BALIKHIN, M. Electron flux dropouts at l 4.2 from global positioning system satellites: occurrences, magnitudes, and main driving factors. **Journal of Geophysical Research: Space Physics**, v. 122, n. 11, p. 11–428, 2017. 76

- BRAUTIGAM, D.; ALBERT, J. Radial diffusion analysis of outer radiation belt electrons during the october 9, 1990, magnetic storm. **Journal of Geophysical Research: Space Physics**, v. 105, n. A1, p. 291–309, 2000. 3, 31, 51, 52
- BRAUTIGAM, D.; GINET, G.; ALBERT, J.; WYGANT, J.; ROWLAND, D.; LING, A.; BASS, J. Crres electric field power spectra and radial diffusion coefficients. **Journal of Geophysical Research: Space Physics**, v. 110, n. A2, 2005. 21, 31
- BRIZARD, A. J.; CHAN, A. A. Relativistic bounce-averaged quasilinear diffusion equation for low-frequency electromagnetic fluctuations. **Physics of Plasmas**, v. 8, n. 11, p. 4762–4771, 2001. 54
- BROUSSARD, R.; SHEELEY, N.; TOUSEY, R.; UNDERWOOD, J. A survey of coronal holes and their solar wind associations throughout sunspot cycle 20. **Solar Physics**, v. 56, n. 1, p. 161–183, 1978. 13
- CAMPBELL, W. H. **Introduction to geomagnetic Fields**. 2. ed. [S.l.]: Cambridge University Press, 2003. 18
- CANE, H.; RICHARDSON, I. Interplanetary coronal mass ejections in the near-earth solar wind during 1996–2002. **Journal of Geophysical Research: Space Physics**, v. 108, n. A4, 2003. 10, 40
- CARVALHO, V. Werneck de; BENYOSEF, L.; SANTIS, A. D. A comparative study of pc's 5-6 geomagnetic pulsations at low and middle latitudes. In: **I PAN AMERICAN WORKSHOP ON GEOMAGNETISM – II PANGEO**. [S.l.: s.n.], 2017. v. 1, p. 111–114. 3
- CASTILHO, J. E.; DOMINGUES, M. O.; PAGAMISSE, A.; MENDES, O. **Introdução ao mundo das wavelets**. São Carlos, São Paulo: Sociedade Brasileira de matemática Aplicada e Computacional, 2012. 144 p. (Notas em Matemática Aplicada, v. 62). ISBN 9788582150139. 43, 45
- CAYTON, T. E.; BELIAN, R. D.; GARY, S. P.; FRITZ, T. A.; BAKER, D. N. Energetic electron components at geosynchronous orbit. **Geophysical Research Letters**, v. 16, n. 2, p. 147–150, 1989. Available from: <<https://agupubs.onlinelibrary.wiley.com/doi/abs/10.1029/GL016i002p00147>>. 25
- CHEN, Y.; FRIEDEL, R.; REEVES, G.; ONSAGER, T.; THOMSEN, M. Multisatellite determination of the relativistic electron phase space density at

geosynchronous orbit: methodology and results during geomagnetically quiet times. **Journal of Geophysical Research: Space Physics**, v. 110, n. A10, 2005. 56

CLAUDEPIERRE, S.; ELKINGTON, S.; WILTBERGER, M. Solar wind driving of magnetospheric ulf waves: pulsations driven by velocity shear at the magnetopause. **Journal of Geophysical Research: Space Physics**, v. 113, n. A5, 2008. 21

CLAUDEPIERRE, S.; WILTBERGER, M.; ELKINGTON, S.; LOTKO, W.; HUDSON, M. Magnetospheric cavity modes driven by solar wind dynamic pressure fluctuations. **Geophysical Research Letters**, v. 36, n. 13, 2009. 21

CLAUDEPIERRE, S. G.; WILTBERGER, M.; ELKINGTON, S. R.; LOTKO, W.; HUDSON, M. K. Magnetospheric cavity modes driven by solar wind dynamic pressure fluctuations. **Geophysical Research Letters**, v. 36, n. 13, 2009. Available from: <<https://agupubs.onlinelibrary.wiley.com/doi/abs/10.1029/2009GL039045>>. 3

DAUBECHIES, I. **Ten lectures on wavelets**. Philadelphia, PA: [s.n.], 1992. 357 p. (CBMS-NSF Regional Conference Series in Applied Mathematics; 61, v. 61). ISSN 00014966. ISBN 0898712742. 44, 46

DENTON, M. H.; BOROVSKY, J. E.; HORNE, R. B.; MCPHERSON, R. L.; MORLEY, S. K.; TSURUTANI, B. T. High-speed solar wind streams: a call for key research. **Eos, Transactions American Geophysical Union**, v. 89, n. 7, p. 62–62, 2008. 12

DOMINGUES, M. O.; MENDES, O.; COSTA, A. M. da. On wavelet techniques in atmospheric sciences. **Advances in Space Research**, v. 35, n. 5, p. 831–842, 2005. ISSN 0273-1177. 44, 45

DROZDOV, A. Y.; SHPRITS, Y. Y.; ORLOVA, K. G.; KELLERMAN, A. C.; SUBBOTIN, D. A.; BAKER, D. N.; SPENCE, H. E.; REEVES, G. D. Energetic, relativistic, and ultrarelativistic electrons: Comparison of long-term verb code simulations with van allen probes measurements. **Journal of Geophysical Research: Space Physics**, v. 120, n. 5, p. 3574–3587, 2015. Available from: <<https://agupubs.onlinelibrary.wiley.com/doi/abs/10.1002/2014JA020637>>. 53

DUNGEY, J. Hydromagnetic waves, physics of geomagnetic phenomena s. **Matsushita, WH Campbell**, v. 913, 1967. 21

DUNGEY, J. W. Interplanetary magnetic field and the auroral zones. **Physical Review Letters**, v. 6, n. 2, p. 47–48, jan. 1961. 16, 18

ECHER, E.; TSURUTANI, B.; GONZALEZ, W.; KOZYRA, J. High speed stream properties and related geomagnetic activity during the whole heliosphere interval (whi): 20 march to 16 april 2008. **Solar Physics**, v. 274, n. 1-2, p. 303–320, 2011. 2, 29

ELKINGTON, S. A review of ulf interactions with radiation belt electrons. In: TAKAHASHI P.J.; CHI, R. D.; LYSAK, R. (Ed.). **Magnetospheric ULF waves: synthesis and new directions**. [S.l.]: American Geophysical Union (AGU), 2006. p. 177–193. 2, 3, 29, 30, 52, 88, 92

ELKINGTON, S. R.; HUDSON, M. K.; CHAN, A. A. Acceleration of relativistic electrons via drift-resonant interaction with toroidal-mode pc-5 ulf oscillations. **Geophysical Research Letters**, v. 26, n. 21, p. 3273–3276, 1999. 2, 3, 29, 30, 51, 52, 88

_____. Resonant acceleration and diffusion of outer zone electrons in an asymmetric geomagnetic field. **Journal of Geophysical Research: Space Physics**, v. 108, n. A3, 2003. 3, 52

FÄLTHAMMAR, C.-G. Effects of time-dependent electric fields on geomagnetically trapped radiation. **Journal of Geophysical Research**, v. 70, n. 11, p. 2503–2516, 1965. 3

FEI, Y.; CHAN, A. A.; ELKINGTON, S. R.; WILTBERGER, M. J. Radial diffusion and mhd particle simulations of relativistic electron transport by ulf waves in the september 1998 storm. **Journal of Geophysical Research: Space Physics**, v. 111, n. A12, 2006. 5, 52, 77, 103

FERNÁNDEZ, M. H. C. **Three dimensional configuration and evolution of coronal mass ejections**. PhD Thesis (PhD) — Technischen Universität Carolo-Wilhelmina, Braunschweig, 2005. 9, 10

FOK, M.-C.; MOORE, T. E.; SPJELDVIK, W. N. Rapid enhancement of radiation belt electron fluxes due to substorm dipolarization of the geomagnetic field. **Journal of Geophysical Research: Space Physics**, v. 106, n. A3, p. 3873–3881, 2001. 70

FORSYTH, C.; RAE, I.; MURPHY, K.; FREEMAN, M.; HUANG, C.-L.; SPENCE, H.; BOYD, A.; COXON, J.; JACKMAN, C.; KALMONI, N. M. E.;

WATT, C. E. J. What effect do substorms have on the content of the radiation belts? **Journal of Geophysical Research. Space physics**, v. 121, n. 7, p. 6292–6306, July 2016. ISSN 2169-9380. 69

GANUSHKINA, N. Y.; AMARIUTEI, O.; SHPRITS, Y.; LIEMOHN, M. Transport of the plasma sheet electrons to the geostationary distances. **Journal of Geophysical Research: Space Physics**, v. 118, n. 1, p. 82–98, 2013. 88

GAO, X.; LI, W.; BORTNIK, J.; THORNE, R. M.; LU, Q.; MA, Q.; TAO, X.; WANG, S. The effect of different solar wind parameters upon significant relativistic electron flux dropouts in the magnetosphere. **Journal of Geophysical Research: Space Physics**, v. 120, n. 6, p. 4324–4337, 2015. Available from: <<https://agupubs.onlinelibrary.wiley.com/doi/abs/10.1002/2015JA021182>>. 64

GIBSON, S. E.; KOZYRA, J. U.; TOMA, G. de; EMERY, B. A.; ONSAGER, T.; THOMPSON, B. J. If the sun is so quiet, why is the earth ringing? a comparison of two solar minimum intervals. **Journal of Geophysical Research: Space Physics**, v. 114, n. A9, 2009. Available from: <<https://agupubs.onlinelibrary.wiley.com/doi/abs/10.1029/2009JA014342>>. 13

GJERLOEV, J. A global ground-based magnetometer initiative. **Eos, Transactions American Geophysical Union**, v. 90, n. 27, p. 230–231, 2009. 50

GLAUERT, S. A.; HORNE, R. B.; MEREDITH, N. P. Three-dimensional electron radiation belt simulations using the bas radiation belt model with new diffusion models for chorus, plasmaspheric hiss, and lightning-generated whistlers. **Journal of Geophysical Research: Space Physics**, v. 119, n. 1, p. 268–289, 2014. Available from: <<https://agupubs.onlinelibrary.wiley.com/doi/abs/10.1002/2013JA019281>>. 25

GONZALEZ, W. D.; JOSELYN, J. a.; KAMIDE, Y.; KROEHL, H. W.; ROSTOKER, G.; TSURUTANI, B. T.; VASYLIUNAS, V. M. What is a geomagnetic storm? **Journal of Geophysical Research**, v. 99, n. A4, p. 5771–5792, 1994. ISSN 0148-0227. 2, 18, 29, 88

GONZALEZ, W. D.; MOZER, F. S. A quantitative model for the potential resulting from reconnection with an arbitrary interplanetary magnetic field. **Journal of Geophysical Research (1896-1977)**, v. 79, n. 28, p. 4186–4194, 1974. Available from: <<https://doi.org/10.1029/JA079i028p04186>>.

[//agupubs.onlinelibrary.wiley.com/doi/abs/10.1029/JA079i028p04186](https://agupubs.onlinelibrary.wiley.com/doi/abs/10.1029/JA079i028p04186)>.

16

GOSLING, J.; HILDNER, E.; MACQUEEN, R.; MUNRO, R.; POLAND, A.; ROSS, C. Direct observations of a flare related coronal and solar wind disturbance. **Solar Physics**, v. 40, n. 2, p. 439–448, 1975. 9

GREEN, J.; KIVELSON, M. A tale of two theories: how the adiabatic response and ulf waves affect relativistic electrons. **Journal of Geophysical Research: Space Physics**, v. 106, n. A11, p. 25777–25791, 2001. 2, 29

GREEN, S.; BURNELL, S.; JONES, M.; BURNELL, S. **An introduction to the sun and stars**. [s.n.], 2004. ISBN 9780521546225. Available from: <<https://books.google.com.br/books?id=lb5owLGIQGsC>>. 7, 55, 56, 58

GUBBINS, D.; HERRERO-BERVERA, E. **Encyclopedia of geomagnetism and paleomagnetism**. [S.l.: s.n.], 2007. (Encyclopedia of Geomagnetism and Paleomagnetism). ISBN 9781402044236. 20

HARGREAVES, J. K. **The solar-terrestrial environment: an introduction to geospace-the science of the terrestrial upper atmosphere, ionosphere, and magnetosphere**. [S.l.: s.n.], 1992. 1

HARTLEY, D.; DENTON, M. Solving the radiation belt riddle. **Astronomy & Geophysics**, v. 55, n. 6, p. 6–17, 2014. 55, 57, 58

HIETALA, H.; KILPUA, E.; TURNER, D.; ANGELOPOULOS, V. Depleting effects of icme-driven sheath regions on the outer electron radiation belt. **Geophysical Research Letters**, v. 41, n. 7, p. 2258–2265, 2014. 76

HORNE, R. B. et al. Wave acceleration of electrons in the van allen radiation belts. **Nature**, v. 437, n. 7056, p. 227–230, 2005. 88

HORNE, R. B.; THORNE, R. M. Potential waves for relativistic electron scattering and stochastic acceleration during magnetic storms. **Geophysical Research Letters**, v. 25, n. 15, p. 3011–3014, 1998. 70

HOWARD, R.; BRUECKNER, G.; CYR, O. S.; BIESECKER, D.; DERE, K.; KOOMEN, M.; KORENDYKE, C.; LAMY, P.; LLEBARIA, A.; BOUT, M.; MICHELS, D.; MOSES, J.; PASWATERS, S.; PLUNKETT, S.; SCHWENN, R.; SIMNETT, G.; SOCKER, D.; TAPPIN, S.; WANG, D. Observations of cmes from soho/lasco. In: _____. **Coronal Mass Ejections**. [S.l.: s.n.], 2013. p. 17–26. ISBN 9781118664377. 9

HOWARD, R.; MICHELS, D.; JUNIOR, N. S.; KOOMEN, M. The observation of a coronal transient directed at earth. **The Astrophysical Journal**, v. 263, p. L101–L104, 1982. 10

HUBBARD, B. B. **The world according to wavelets: the story of a mathematical technique in the making**. 2. ed. Natick, MA: [s.n.], 1998. (Ak Peters Series). ISBN 9781568810720. 44

HUDSON, M.; ELKINGTON, S.; LYON, J.; GOODRICH, C.; ROSENBERG, T. Simulation of radiation belt dynamics driven by solar wind variations. **Sun-Earth Plasma Connections**, p. 171–182, 1999. 30

HUDSON, M. K.; DENTON, R. E.; LESSARD, M. R.; MIFTAKHOVA, E. G.; ANDERSON, R. R. A study of pc-5 ulf oscillations. **Annales Geophysicae**, v. 22, n. 1, p. 289–302, 2004. Available from: <<https://angeo.copernicus.org/articles/22/289/2004/>>. 3

HUGHES, W. J. Magnetospheric ULF waves: a tutorial with a historical perspective. In: ENGBRETSON, M. J.; TAKAHASHI, K.; SCHOLER, M. (Ed.). **Solar wind sources of magnetospheric ultra-low-frequency waves**. Washington, D. C: [s.n.], 1994. p. 1 – 11. ISBN 9781118663943. 21

INTRILIGATOR, D. S. Evidence for a constant speed of shock propagation between 0.8 au and 2.2 au. In: **International Cosmic Ray Conference**. [S.l.: s.n.], 1977. v. 11, p. 225–229. 13

JACOBS, J. A. **Geomagnetism**. London, UK: [s.n.], 1991. 806 p. (Geomagnetism, v. 4). ISBN 0-12-378674-6. 2, 3, 18, 19

KAMIDE, Y.; CHIAN, A. C. L. **Handbook of the solar-terrestrial environment**. Berlin, Germany: [s.n.], 2007. 1–539 p. ISSN 0096-3941. ISBN 9783540463146. 8, 19, 20, 21

KATSAVRIAS, C.; DAGLIS, I. A.; LI, W. On the statistics of acceleration and loss of relativistic electrons in the outer radiation belt: a superposed epoch analysis. **Journal of Geophysical Research: Space Physics**, v. 124, n. 4, p. 2755–2768, 2019. Available from: <<https://agupubs.onlinelibrary.wiley.com/doi/abs/10.1029/2019JA026569>>. 41

KAVANAGH, A.; DENTON, M. High-speed solar-wind streams and geospace interactions. **Astronomy & Geophysics**, v. 48, n. 6, p. 6–24, 2007. 12

KELLEY, M. **The earth's ionosphere: plasma physics & electrodynamics.** [S.l.: s.n.], 2009. (International Geophysics). ISBN 9780080916576. 17

KEPKO, L.; SPENCE, H. E. Observations of discrete, global magnetospheric oscillations directly driven by solar wind density variations. **Journal of Geophysical Research: Space Physics**, v. 108, n. A6, 2003. 90

KEPKO, L.; SPENCE, H. E.; SINGER, H. Ulf waves in the solar wind as direct drivers of magnetospheric pulsations. **Geophysical Research Letters**, v. 29, n. 8, p. 39–1, 2002. 90

KILPUA, E.; HIETALA, H.; TURNER, D.; KOSKINEN, H.; PULKKINEN, T. I.; RODRIGUEZ, J.; REEVES, G.; CLAUDEPIERRE, S.; SPENCE, H. E. Unraveling the drivers of the storm time radiation belt response. **Geophysical Research Letters**, v. 42, n. 9, p. 3076–3084, 2015. 64, 71, 76, 77

KIM, H.-J.; CHAN, A. A. Fully adiabatic changes in storm time relativistic electron fluxes. **Journal of Geophysical Research: Space Physics**, v. 102, n. A10, p. 22107–22116, 1997. 59

KIVELSON, M. G.; RUSSELL, C. T. **Introduction to space physics.** Cambridge, UK: [s.n.], 1995. 568 p. (Cambridge atmospheric and space science series). ISBN 978-0-521-45714-9. 7, 8, 9, 15, 16, 21, 25

KLETZING, C. A.; KURTH, W. S.; ACUNA, M.; MACDOWALL, R. J.; TORBERT, R. B.; AVERKAMP, T.; BODET, D.; BOUNDS, S. R.; CHUTTER, M.; CONNERNEY, J.; CRAWFORD, D.; DOLAN, J. S.; DVORSKY, R.; HOSPODARSKY, G. B.; HOWARD, J.; JORDANOVA, V.; JOHNSON, R. A.; KIRCHNER, D. L.; MOKRZYCKI, B.; NEEDELL, G.; ODOM, J.; MARK, D.; PFAFF, R.; PHILLIPS, J. R.; PIKER, C. W.; REMINGTON, S. L.; ROWLAND, D.; SANTOLIK, O.; SCHNURR, R.; SHEPPARD, D.; SMITH, C. W.; THORNE, R. M.; TYLER, J. The electric and magnetic field instrument suite and integrated science (emfisis) on rbsp. **Space Science Reviews**, v. 179, n. 1, p. 127–181, Nov 2013. ISSN 1572-9672. 33, 49

KUMAR, P.; FOUFOULA-GEORGIOU, E. Wavelet analysis for geophysical applications. **Reviews of Geophysics**, v. 35, n. 4, p. 385, 1997. ISSN 8755-1209. 46

LEE, D.-Y.; LYONS, L. R.; KIM, K. C.; BAEK, J.-H.; KIM, K.-H.; KIM, H.-J.; WEYGAND, J.; MOON, Y.-J.; CHO, K.-S.; PARK, Y. D.; HAN, W. Repetitive

substorms caused by alfvénic waves of the interplanetary magnetic field during high-speed solar wind streams. **Journal of Geophysical Research: Space Physics**, v. 111, n. A12, 2006. 88

LI, W.; THORNE, R. M.; BORTNIK, J.; BAKER, D. N.; REEVES, G. D.; KANEKAL, S. G.; SPENCE, H. E.; GREEN, J. C. Solar wind conditions leading to efficient radiation belt electron acceleration: a superposed epoch analysis. **Geophysical Research Letters**, v. 42, n. 17, p. 6906–6915, 2015. Available from: <<https://agupubs.onlinelibrary.wiley.com/doi/abs/10.1002/2015GL065342>>. 41

LINDBLAD, B. A.; LUNDSTEDT, H. A catalogue of high-speed plasma streams in the solar wind. **Solar Physics**, v. 74, n. 1, p. 197–206, Nov 1981. ISSN 1573-093X. 13

LIU, W.; ROSTOKER, G.; BAKER, D. Internal acceleration of relativistic electrons by large-amplitude ulf pulsations. **Journal of Geophysical Research: Space Physics**, v. 104, n. A8, p. 17391–17407, 1999. 29

LIU, W.; TU, W.; LI, X.; SARRIS, T.; KHOTYAINTSEV, Y.; FU, H.; ZHANG, H.; SHI, Q. On the calculation of electric diffusion coefficient of radiation belt electrons with in situ electric field measurements by themis. **Geophysical Research Letters**, v. 43, n. 3, p. 1023–1030, 2016. 54

LOPEZ, R. E.; GONZALEZ, W. D. Magnetospheric balance of solar wind dynamic pressure. **Geophysical Research Letters**, v. 44, n. 7, p. 2991–2999, 2017. Available from: <<https://agupubs.onlinelibrary.wiley.com/doi/abs/10.1002/2017GL072817>>. 15

LUEHR, H.; GRAFE, A.; PELLINEN, R.; KATAJA, E. International monitor for auroral geomagnetic effects (image): a new magnetometer network in scandinavia. In: **Fifth EISCAT Scientific Workshop**. [S.l.: s.n.], 1991. 34

LYONS, L.; LEE, D.-Y.; THORNE, R.; HORNE, R.; SMITH, A. Solar wind-magnetosphere coupling leading to relativistic electron energization during high-speed streams. **Journal of Geophysical Research: Space Physics**, v. 110, n. A11, 2005. 71

MANN, I.; O'BRIEN, T.; MILLING, D. Correlations between ulf wave power, solar wind speed, and relativistic electron flux in the magnetosphere: solar cycle dependence. **Journal of Atmospheric and Solar-Terrestrial Physics**, v. 66, n. 2, p. 187–198, 2004. 2, 29

MANN, I. R.; MILLING, D. K.; RAE, I. J.; OZEKE, L. G.; KALE, A.; KALE, Z. C.; MURPHY, K. R.; PARENT, A.; USANOVA, M.; PAHUD, D. M.; LEE, E.-A.; AMALRAJ, V.; WALLIS, D. D.; ANGELOPOULOS, V.; GLASSMEIER, K.-H.; RUSSELL, C. T.; AUSTER, H.-U.; SINGER, H. J. The upgraded carisma magnetometer array in the themis era. **Space Science Reviews**, v. 141, n. 1, p. 413–451, Dec 2008. ISSN 1572-9672. 34

MANN, I. R.; WRIGHT, A. N.; MILLS, K. J.; NAKARIAKOV, V. M. Excitation of magnetospheric waveguide modes by magnetosheath flows. **Journal of Geophysical Research: Space Physics**, v. 104, n. A1, p. 333–353, 1999. Available from: <<https://agupubs.onlinelibrary.wiley.com/doi/abs/10.1029/1998JA900026>>. 24

MAUK, B.; FOX, N. J.; KANEKAL, S.; KESSEL, R.; SIBECK, D.; UKHORSKIY, A. Science objectives and rationale for the radiation belt storm probes mission. **Space Science Reviews**, v. 179, n. 1-4, p. 3–27, 2013. 33, 34

MAVROMICHALAKI, H.; VASSILAKI, A. Fast plasma streams recorded near the earth during 1985-1996. **Solar Physics**, v. 183, n. 1, p. 181–200, 1998. ISSN 1573-093X. Available from: <<https://doi.org/10.1023/A:1005004328071>>. 13, 14

MAVROMICHALAKI, H.; VASSILAKI, A.; MARMATSOURI, E. A catalogue of high-speed solar-wind streams: further evidence of their relationship to ap-index. **Solar Physics**, v. 115, n. 2, p. 345–365, 1988. ISSN 1573-093X. Available from: <<https://doi.org/10.1007/BF00148733>>. 13

MCCOMAS, D.; BAME, S.; BARKER, P.; FELDMAN, W.; PHILLIPS, J.; RILEY, P.; GRIFFEE, J. Solar wind electron proton alpha monitor (swepam) for the advanced composition explorer. In: MEWALDT R. A.; VON ROSENVINGE, T. T. R. C. (Ed.). **The advanced composition explorer mission**. [S.l.: s.n.], 1998. p. 563–612. 33

MCILWAIN, C. E. Coordinates for mapping the distribution of magnetically trapped particles. **Journal of Geophysical Research (1896-1977)**, v. 66, n. 11, p. 3681–3691, 1961. Available from: <<https://agupubs.onlinelibrary.wiley.com/doi/abs/10.1029/JZ066i011p03681>>. 21

MCPHERRON, R. L. Magnetic pulsations: their sources and relation to solar wind and geomagnetic activity. **Surveys in Geophysics**, v. 26, n. 5, p. 545–592, 2005. ISSN 01693298. 22, 23

MENDES, O.; COSTA, A. M. D.; DOMINGUES, M. O. Introduction to planetary electrodynamics: a view of electric fields, currents and related magnetic fields. **Advances in Space Research**, v. 35, n. 5, p. 812–828, 2005. ISSN 02731177. 18

MEREDITH, N. P.; CAIN, M.; HORNE, R. B.; THORNE, R. M.; SUMMERS, D.; ANDERSON, R. R. Evidence for chorus-driven electron acceleration to relativistic energies from a survey of geomagnetically disturbed periods. **Journal of Geophysical Research: Space Physics**, v. 108, n. A6, 2003. 69, 71

MERRILL, R. T.; MCFADDEN, P. L.; MCELHINNY, M. W. **The magnetic field of the Earth**: paleomagnetism, the core, and the deep mantle. ilustrada. San Diego, California: [s.n.], 1998. 531 p. (International geophysics series). ISBN 9780124912465. 15, 17, 47

MIERLA, M.; INHESTER, B.; ANTUNES, A.; BOURSIER, Y.; BYRNE, J. P.; COLANINNO, R.; DAVILA, J.; KONING, C. A. de; GALLAGHER, P. T.; GISSOT, S.; HOWARD, R. A.; HOWARD, T. A.; KRAMAR, M.; LAMY, P.; LIEWER, P. C.; MALONEY, S.; MARQUÉ, C.; MCATEER, R. T. J.; MORAN, T.; RODRIGUEZ, L.; SRIVASTAVA, N.; CYR, O. C. S.; STENBORG, G.; TEMMER, M.; THERNISIEN, A.; VOURLIDAS, A.; WEST, M. J.; WOOD, B. E.; ZHUKOV, A. N. On the 3-d reconstruction of coronal mass ejections using coronagraph data. **Annales Geophysicae**, v. 28, n. 1, p. 203–215, 2010. 9

MIYOSHI, Y.; KATAOKA, R. Flux enhancement of the outer radiation belt electrons after the arrival of stream interaction regions. **Journal of Geophysical Research: Space Physics**, v. 113, n. A3, 2008. 71

MOLCHANOV, O.; SCHEKOTOV, a.; FEDOROV, E.; BELYAEV, G.; GORDEEV, E. Preseismic ULF electromagnetic effect from observation at Kamchatka. **Natural Hazards and Earth System Science**, v. 3, n. 3/4, p. 203–209, 2003. ISSN 1684-9981. 2, 18

MOLDWIN, M. B. **Introduction to space weather**. Cambridge, UK: [s.n.], 2008. 134 p. ISSN 02659646. ISBN 978-0-521-86149-6. 9, 16

MOLDWIN, M. B.; DOWNWARD, L.; RASSOUL, H. K.; AMIN, R.; ANDERSON, R. R. A new model of the location of the plasmopause: Crres

results. **Journal of Geophysical Research: Space Physics**, v. 107, n. A11, p. SMP 2–1–SMP 2–9, 2002. Available from: <<https://agupubs.onlinelibrary.wiley.com/doi/abs/10.1029/2001JA009211>>. 25

MORLEY, S.; ROUILLARD, A.; FREEMAN, M. P. Recurrent substorm activity during the passage of a corotating interaction region. **Journal of atmospheric and solar-terrestrial physics**, v. 71, n. 10-11, p. 1073–1081, 2009. 12

MOYA, P. S.; PINTO, V. A.; SIBECK, D. G.; KANEKAL, S. G.; BAKER, D. N. On the effect of geomagnetic storms on relativistic electrons in the outer radiation belt: Van allen probes observations. **Journal of Geophysical Research: Space Physics**, v. 122, n. 11, p. 11–100, 2017. 76

MURPHY, K. R.; WATT, C.; MANN, I. R.; RAE, I. J.; SIBECK, D. G.; BOYD, A.; FORSYTH, C.; TURNER, D.; CLAUDEPIERRE, S.; BAKER, D. et al. The global statistical response of the outer radiation belt during geomagnetic storms. **Geophysical Research Letters**, v. 45, n. 9, p. 3783–3792, 2018. 41, 42, 59, 77

NAKAMURA, R.; BLAKE, J.; ELKINGTON, S.; BAKER, D.; BAUMJOHANN, W.; KLECKER, B. Relationship between ulf waves and radiation belt electrons during the march 10, 1998, storm. **Advances in Space Research**, v. 30, n. 10, p. 2163–2168, 2002. 2, 29

NI, B.; XIANG, Z.; GU, X.; SHPRITS, Y. Y.; ZHOU, C.; ZHAO, Z.; ZHANG, X.; ZUO, P. Dynamic responses of the earth’s radiation belts during periods of solar wind dynamic pressure pulse based on normalized superposed epoch analysis. **Journal of Geophysical Research: Space Physics**, v. 121, n. 9, p. 8523–8536, 2016. Available from: <<https://agupubs.onlinelibrary.wiley.com/doi/abs/10.1002/2016JA023067>>. 64

NORTHROP, T. G. Adiabatic charged-particle motion. **Reviews of Geophysics**, v. 1, n. 3, p. 283–304, 1963. Available from: <<https://agupubs.onlinelibrary.wiley.com/doi/abs/10.1029/RG001i003p00283>>. 27

O’BRIEN, T.; MCPHERRON, R.; SORNETTE, D.; REEVES, G.; FRIEDEL, R.; SINGER, H. Which magnetic storms produce relativistic electrons at geosynchronous orbit? **Journal of Geophysical Research: Space Physics**, v. 106, n. A8, p. 15533–15544, 2001. 41, 59

OWENS, M. J.; FORSYTH, R. J. The heliospheric magnetic field. **Living Reviews in Solar Physics**, v. 10, n. 1, p. 5, 2013. 9

- OZEKE, L. G.; MANN, I. R.; MURPHY, K. R.; RAE, I. J.; MILLING, D. K.; ELKINGTON, S. R.; CHAN, A. A.; SINGER, H. J. Ulf wave derived radiation belt radial diffusion coefficients. **Journal of Geophysical Research: Space Physics**, v. 117, n. A4, 2012. 31, 53, 81, 93
- OZEKE, L. G.; MANN, I. R.; MURPHY, K. R.; RAE, I. J.; MILLING, D. K. Analytic expressions for ulf wave radiation belt radial diffusion coefficients. **Journal of Geophysical Research: Space Physics**, v. 119, n. 3, p. 1587–1605, 2014. xvii, 3, 5, 31, 51, 52, 53, 54, 81, 82, 83, 84, 88, 93, 94, 99
- PARKER, E. N. Dynamics of the interplanetary gas and magnetic fields. **The Astrophysical Journal**, v. 128, p. 664, 1958. ISSN 0004-637X. 8
- PARKS, G. K. **Physics of space plasmas: an introduction**. Redwood City, CA: [s.n.], 1991. 538 p. 7, 8, 19
- PAULIKAS, G.; BLAKE, J. Effects of the solar wind on magnetospheric dynamics: energetic electrons at the synchronous orbit. **Quantitative Modeling of Magnetospheric Processes, Geophysics, Monography Series**, v. 21, p. 180–202, 1979. 59
- PHILLIPS, J.; BAME, S.; FELDMAN, W.; GOSLING, J.; HAMMOND, C.; MCCOMAS, D.; GOLDSTEIN, B.; NEUGEBAUER, M.; SCIME, E.; SUESS, S. Ulysses solar wind plasma observations at high southerly latitudes. **Science**, v. 268, n. 5213, p. 1030–1033, 1995. 12
- PILIPENKO, V. A. ULF waves on the ground and in space. **Journal of Atmospheric and Terrestrial Physics**, v. 52, n. 12, p. 1193–1209, 1990. ISSN 00219169. 2, 18
- PRESS, W. H. **Numerical recipes: the art of scientific computing**. 3. ed. [S.l.: s.n.], 2007. 1235 p. ISSN 00401706. ISBN 9780521880688. 43
- PRIEST, E. **Magnetohydrodynamics of the Sun**. [S.l.: s.n.], 2014. 8
- REEVES, G. D.; MCADAMS, K. L.; FRIEDEL, R. H. W.; O'BRIEN, T. P. Acceleration and loss of relativistic electrons during geomagnetic storms. **Geophysical Research Letters**, v. 30, n. 10, p. n/a–n/a, 2003. ISSN 1944-8007. 1529. 27
- REEVES, G. D.; SPENCE, H. E.; HENDERSON, M. G.; MORLEY, S. K.; FRIEDEL, R. H. W.; FUNSTEN, H. O.; BAKER, D. N.; KANEKAL, S. G.;

BLAKE, J. B.; FENNELL, J. F.; CLAUDEPIERRE, S. G.; THORNE, R. M.; TURNER, D. L.; KLETZING, C. A.; KURTH, W. S.; LARSEN, B. A.; NIEHOF, J. T. Electron acceleration in the heart of the Van Allen radiation belts. **Science**, v. 341, n. 6149, p. 991–994, 2013. ISSN 0036-8075. 59

RICHARDSON, I.; CANE, H. Near-earth interplanetary coronal mass ejections during solar cycle 23 (1996–2009): catalog and summary of properties. **Solar Physics**, v. 264, n. 1, p. 189–237, 2010. 10, 11, 40

RODGER, C. J.; HENDRY, A. T.; CLILVERD, M. A.; KLETZING, C. A.; BRUNDELL, J. B.; REEVES, G. D. High-resolution in situ observations of electron precipitation-causing emic waves. **Geophysical Research Letters**, v. 42, n. 22, p. 9633–9641, 2015. 69

ROEDERER, J. G. **Dynamics of geomagnetically trapped radiation**. [S.l.: s.n.], 1970. 29, 85, 95

ROEDERER, J. G.; ZHANG, H. **Dynamics of magnetically trapped particles: foundations of the physics of radiation belts and space plasmas**. 2. ed. Berlin: Springer, 2014. (Astrophysics and Space Science Library). 27, 29

SAITO, T. Geomagnetic pulsations. **Space Science Reviews**, v. 10, n. 3, p. 319–412, 1969. ISSN 00386308. 2, 3, 18, 19

_____. Resonance model of Pc3 in subtropical regions. In: CARDÚS, J. O. (Ed.). **Scientific contributions in commemoration of ebro observatory's 75th anniversary**. São Paulo: [s.n.], 1983. p. 175–180. 3

SAMSON, J. C. Geomagnetic pulsations and plasma waves in the earth's magnetosphere. In: JACOBS, J. (Ed.). **Geomagnetism, Volume 4**. London, UK: [s.n.], 1991. ISBN 0123786746. 19, 20, 51, 92

SARRIS, T. E.; LI, X. Calculating ultra-low-frequency wave power of the compressional magnetic field vs. l and time: multi-spacecraft analysis using the van allen probes, themis and goes. **Annales Geophysicae**, v. 34, n. 6, p. 565–571, 2016. Available from:
<<https://angeo.copernicus.org/articles/34/565/2016/>>. 54

SCHULZ, M.; LANZEROTTI, L. J. **Particle diffusion in the radiation belts**. [S.l.: s.n.], 2012. 3, 5, 27, 51, 55

SCHUNK, R. W.; NAGY, A. F. **Ionospheres: physics, plasma physics, and chemistry**. 2. ed.. ed. Cambridge, UK: [s.n.], 2009. 628 p. ISBN 0521632374 0521607701. 7, 15

SCHWENN, R. Space weather: the solar perspective. **Living Reviews in Solar Physics**, v. 3, n. 1, p. 2, 2006. 10

SCHWENN, R.; LAGO, A. D.; HUTTUNEN, E.; GONZALEZ, W. D. The association of coronal mass ejections with their effects near the earth. **Annales Geophysicae**, v. 23, n. 3, p. 1033–1059, 2005. Available from: <<https://angeo.copernicus.org/articles/23/1033/2005/>>. 10

SILVA, G. B. D.; PADILHA, A. L.; ALVES, L. R. Latitudinal variation of pc3–pc5 geomagnetic pulsation amplitude across the dip equator in central south america. **Annales Geophysicae**, v. 38, n. 1, p. 35–49, 2020. Available from: <<https://angeo.copernicus.org/articles/38/35/2020/>>. 3

SILVA, L. A. D.; SIBECK, D.; ALVES, L. R.; SOUZA, V. M.; JAUER, P. R.; CLAUDEPIERRE, S. G.; MARCHEZI, J. P.; AGAPITOV, O.; MEDEIROS, C.; VIEIRA, L. E. A.; WANG, C.; JIANKUI, S.; LIU, Z.; GONZALEZ, W.; LAGO, A. D.; ROCKENBACH, M.; PADUA, M. B.; ALVES, M. V.; BARBOSA, M. V. G.; FOK, M.-C.; BAKER, D.; KLETZING, C.; KANEKAL, S. G.; GEORGIU, M. Contribution of ulf wave activity to the global recovery of the outer radiation belt during the passage of a high-speed solar wind stream observed in september 2014. **Journal of Geophysical Research: Space Physics**, v. 124, n. 3, p. 1660–1678, 2019. Available from: <<https://agupubs.onlinelibrary.wiley.com/doi/abs/10.1029/2018JA026184>>. 5, 42

SIMOES, M. C. **Identificação de distúrbios em magnetogramas associados a tempestades magnéticas utilizando técnicas wavelets**. 2011. 147 p. PhD Thesis (Dissertação) — Instituto Nacional de Pesquisas Espaciais - INPE, São José dos Campos, 2011. 45

SMITH, C. W.; L'HEUREUX, J.; NESS, N. F.; ACUÑA, M. H.; BURLAGA, L. F.; SCHEIFELE, J. The ace magnetic fields experiment. In: _____. **The advanced composition explorer mission**. [S.l.: s.n.], 1998. 33

SMITH, E. J.; WOLFE, J. H. Observations of interaction regions and corotating shocks between one and five au: Pioneers 10 and 11. **Geophysical Research Letters**, v. 3, n. 3, p. 137–140, 1976. 12

- SOUTHWOOD, D. J.; KIVELSON, M. G. Charged particle behavior in low-frequency geomagnetic pulsations 1. transverse waves. **Journal of Geophysical Research: Space Physics**, v. 86, n. A7, p. 5643–5655, 1981. 30
- SOUZA, V. M.; LOPEZ, R. E.; JAUER, P. R.; SIBECK, D. G.; PHAM, K.; SILVA, L. A. D.; MARCHEZI, J. P.; ALVES, L. R.; KOGA, D.; MEDEIROS, C.; ROCKENBACH, M.; GONZALEZ, W. D. Acceleration of radiation belt electrons and the role of the average interplanetary magnetic field bz component in high-speed streams. **Journal of Geophysical Research: Space Physics**, v. 122, n. 10, p. 10,084–10,101, 2017. 42
- STONE, E. C.; FRANDBSEN, A.; MEWALDT, R.; CHRISTIAN, E.; MARGOLIES, D.; ORMES, J.; SNOW, F. The advanced composition explorer. **Space Science Reviews**, v. 86, n. 1-4, p. 1–22, 1998. 33
- SUBBOTIN, D. A.; SHPRITS, Y. Y. Three-dimensional modeling of the radiation belts using the versatile electron radiation belt (verb) code. **Space Weather**, v. 7, n. 10, 2009. Available from: <<https://agupubs.onlinelibrary.wiley.com/doi/abs/10.1029/2008SW000452>>. 53
- SUMMERS, D.; MA, C.-y. Rapid acceleration of electrons in the magnetosphere by fast-mode mhd waves. **Journal of Geophysical Research: Space Physics**, v. 105, n. A7, p. 15887–15895, 2000. 30, 88
- TAKAHASHI, K. Ulf waves in the inner magnetosphere. In: _____. **Low-frequency waves in space plasmas**. [s.n.], 2016. chapter 4, p. 51–63. ISBN 9781119055006. Available from: <<https://agupubs.onlinelibrary.wiley.com/doi/abs/10.1002/9781119055006.ch4>>. 22, 23
- TANG, C.; ZHANG, J.-C.; REEVES, G. D.; SU, Z.; BAKER, D.; SPENCE, H.; FUNSTEN, H.; BLAKE, J.; WYGANT, J. Prompt enhancement of the earth's outer radiation belt due to substorm electron injections. **Journal of Geophysical Research: Space Physics**, v. 121, n. 12, p. 11–826, 2016. 88
- THORNE, R. M. Radiation belt dynamics: the importance of wave-particle interactions. **Geophysical Research Letters**, v. 37, n. 22, 2010. 21
- THORNE, R. M.; LI, W.; NI, B.; MA, Q.; BORTNIK, J.; CHEN, L.; BAKER, D. N.; SPENCE, H. E.; REEVES, G. D.; HENDERSON, M. G.; KLETZING, C. A.; KURTH, W. S.; HOSPODARSKY, G. B.; BLAKE, J. B.; FENNELL, J. F.;

CLAUDEPIERRE, S. G.; KANEKAL, S. G. Rapid local acceleration of relativistic radiation-belt electrons by magnetospheric chorus. **Nature**, v. 504, n. 7480, p. 411–414, Dec 2013. ISSN 1476-4687. Available from: <<https://doi.org/10.1038/nature12889>>. 2, 29

TRIVEDI, N. B.; ARORA, B. R.; PADILHA, A. L.; Da Costa, J. M.; DUTRA, S. L. G.; CHAMALAUN, F. H.; RIGOTI, A. Global Pc5 geomagnetic pulsations of March 24, 1991, as observed along the American Sector. **Geophysical Research Letters**, v. 24, n. 13, p. 1683, 1997. ISSN 0094-8276. 3

TSURUTANI, B. T.; GONZALEZ, W. D.; GONZALEZ, A. L.; TANG, F.; ARBALLO, J. K.; OKADA, M. Interplanetary origin of geomagnetic activity in the declining phase of the solar cycle. **Journal of Geophysical Research: Space Physics**, v. 100, n. A11, p. 21717–21733, 1995. 2, 18, 29, 88

TSURUTANI, B. T.; GONZALEZ, W. D.; GONZALEZ, A. L. C.; GUARNIERI, F. L.; GOPALSWAMY, N.; GRANDE, M.; KAMIDE, Y.; KASAHARA, Y.; LU, G.; MANN, I.; MCPHERRON, R.; SORAAS, F.; VASYLIUNAS, V. Corotating solar wind streams and recurrent geomagnetic activity: a review. **Journal of Geophysical Research: Space Physics**, v. 111, n. A7, 2006. Available from: <<https://agupubs.onlinelibrary.wiley.com/doi/abs/10.1029/2005JA011273>>. 12

TSURUTANI, B. T.; SMITH, E. J.; PYLE, K. R.; SIMPSON, J. A. Energetic protons accelerated at corotating shocks: pioneer 10 and 11 observations from 1 to 6 au. **Journal of Geophysical Research: Space Physics**, v. 87, n. A9, p. 7389–7404, 1982. Available from: <<https://agupubs.onlinelibrary.wiley.com/doi/abs/10.1029/JA087iA09p07389>>. 12

TURNER, D. L.; KILPUA, E. K. J.; HIETALA, H.; CLAUDEPIERRE, S. G.; O'BRIEN, T. P.; FENNELL, J. F.; BLAKE, J. B.; JAYNES, A. N.; KANEKAL, S.; BAKER, D. N.; SPENCE, H. E.; RIPOLL, J.-F.; REEVES, G. D. The response of earth's electron radiation belts to geomagnetic storms: statistics from the van allen probes era including effects from different storm drivers. **Journal of Geophysical Research: Space Physics**, v. 124, n. 2, p. 1013–1034, 2019. Available from: <<https://agupubs.onlinelibrary.wiley.com/doi/abs/10.1029/2018JA026066>>. 41, 42, 59, 66, 71, 77

- TURNER, D. L.; SHPRITS, Y.; HARTINGER, M.; ANGELOPOULOS, V. Explaining sudden losses of outer radiation belt electrons during geomagnetic storms. **Nature Physics**, v. 8, n. 3, p. 208–212, 2012. 41, 59
- UKHORSKIY, A.; ANDERSON, B.; TAKAHASHI, K.; TSYGANENKO, N. Impact of ulf oscillations in solar wind dynamic pressure on the outer radiation belt electrons. **Geophysical Research Letters**, v. 33, n. 6, 2006. 21
- UKHORSKIY, A. Y.; TAKAHASHI, K.; ANDERSON, B. J.; KORTH, H. Impact of toroidal ulf waves on the outer radiation belt electrons. **Journal of Geophysical Research: Space Physics**, v. 110, n. A10, 2005. ISSN 2156-2202. A10202. 92
- VILLANTE, U. Ultra low frequency waves in the magnetosphere. In: KAMIDE, Y.; CHIAN, A. (Ed.). **Handbook of the solar-terrestrial environment**. [S.l.: s.n.], 2007. p. 397–422. ISBN 978-3-540-46314-6. 20, 21
- VOURLIDAS, A.; BALMACEDA, L. A.; STENBORG, G.; LAGO, A. D. Multi-viewpoint coronal mass ejection catalog based on stereo cor2 observations. **The Astrophysical Journal**, v. 838, n. 2, p. 141, 2017. 10
- VOURLIDAS, A.; LYNCH, B. J.; HOWARD, R. A.; LI, Y. How many cmes have flux ropes? deciphering the signatures of shocks, flux ropes, and prominences in coronagraph observations of cmes. **Solar Physics**, v. 284, n. 1, p. 179–201, 2013. 10
- WOODROFFE, J. R. **Ultra-low frequency waves, magnetic pulsations, and the ionospheric Alfvén resonator**. PhD Thesis (Phd Thesis) — University of Minnesota, 2010. 19
- WYGANT, J. R.; BONNELL, J. W.; GOETZ, K.; ERGUN, R. E.; MOZER, F. S.; BALE, S. D.; LUDLAM, M.; TURIN, P.; HARVEY, P. R.; HOCHMANN, R.; HARPS, K.; DALTON, G.; MCCAULEY, J.; RACHELSON, W.; GORDON, D.; DONAKOWSKI, B.; SHULTZ, C.; SMITH, C.; DIAZ-AGUADO, M.; FISCHER, J.; HEAVNER, S.; BERG, P.; MALSAPINA, D. M.; BOLTON, M. K.; HUDSON, M.; STRANGWAY, R. J.; BAKER, D. N.; LI, X.; ALBERT, J.; FOSTER, J. C.; CHASTON, C. C.; MANN, I.; DONOVAN, E.; CULLY, C. M.; CATTELL, C. A.; KRASNOSELSKIKH, V.; KERSTEN, K.; BRENNEMAN, A.; TAO, J. B. The electric field and waves instruments on the radiation belt storm probes mission. **Space Science Reviews**, v. 179, n. 1, p. 183–220, Nov 2013. ISSN 1572-9672. Available from: <<https://doi.org/10.1007/s11214-013-0013-7>>. 49

XYSTOURIS, G.; SIGALA, E.; MAVROMICHALAKI, H. A complete catalogue of high-speed solar wind streams during solar cycle 23. **Solar Physics**, v. 289, n. 3, p. 995–1012, 2014. 14

YUAN, C.; ZONG, Q. The double-belt outer radiation belt during cme- and cir-driven geomagnetic storms. **Journal of Geophysical Research: Space Physics**, v. 118, n. 10, p. 6291–6301, 2013. Available from: <<https://agupubs.onlinelibrary.wiley.com/doi/abs/10.1002/jgra.50564>>. 64

_____. The double-belt outer radiation belt during cme-and cir-driven geomagnetic storms. **Journal of Geophysical Research: Space Physics**, v. 118, n. 10, p. 6291–6301, 2013. 76

YUMOTO, K. External and internal sources of low-frequency MHD waves in the magnetosphere - a review. **Journal of Geomagnetism and Geoelectricity**, v. 40, p. 293–311, 1988. 3

ZHANG, X.-Y.; MOLDWIN, M.; STEINBERG, J.; SKOUG, R. Alfvén waves as a possible source of long-duration, large-amplitude, and geoeffective southward imf. **Journal of Geophysical Research: Space Physics**, v. 119, n. 5, p. 3259–3266, 2014. 88

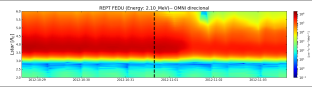
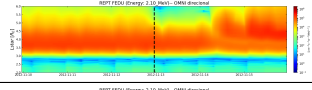
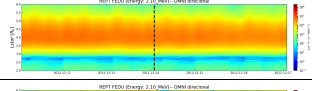
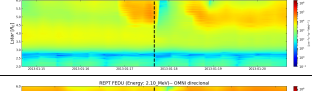
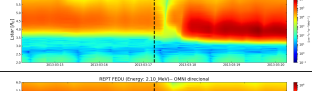
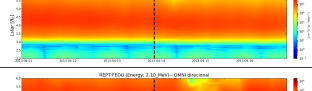
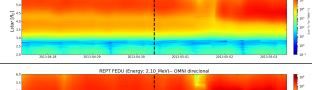
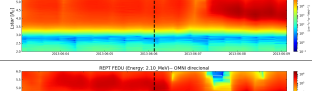
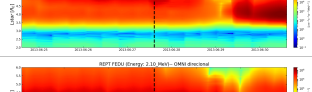
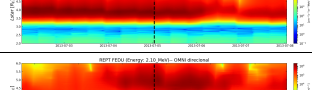
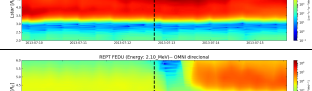
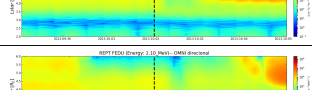
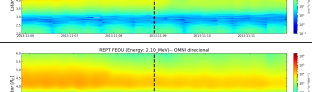
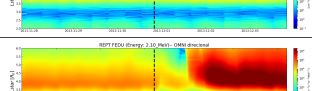
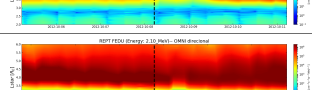
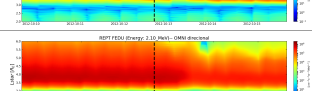
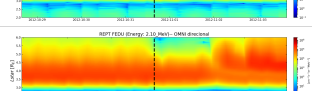
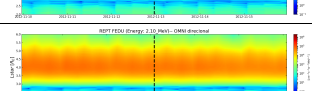
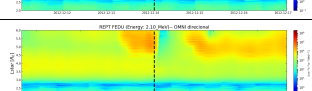
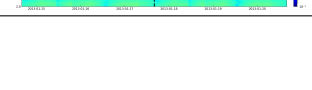
APPENDIX A - ICME EVENT DATES AND FLUX

Table A.1 - All the events with flux variations related to ICME events. The columns represents the event type, the day that it occurs and the instant that the structure arrives and interact with Earth's magnetosphere. The last column show the 2.10 MeV electron flux density during the event, plotted with respect of L^* (y-axis) and time (x-axis). The period corresponds to 3 days before and after the event, marked with the dashed black line in each graph.

Event	Day	Hour	Flux
CME	2012-10-08	05:16	
CME	2012-10-12	19:00	
CME	2012-10-31	15:38	
CME	2012-11-12	23:11	
CME	2012-12-14	02:00	
CME	2013-01-17	16:00	
CME	2013-03-17	05:59	
CME	2013-04-13	22:54	
CME	2013-04-30	09:49	
CME	2013-06-06	02:55	
CME	2013-06-27	14:38	
CME	2013-07-05	01:00	
CME	2013-07-12	17:14	
CME	2013-10-02	01:54	
CME	2013-11-08	22:00	

CME	2013-11-30	20:00	
CME	2013-12-15	13:00	
CME	2013-12-24	21:00	
CME	2014-02-07	17:05	
CME	2014-02-15	13:16	
CME	2014-02-19	03:48	
CME	2014-04-05	10:00	
CME	2014-04-11	06:00	
CME	2014-04-29	20:00	
CME	2014-08-19	06:57	
CME	2014-09-12	15:53	
CME	2014-12-21	19:11	
CME	2015-01-07	06:16	
CME	2015-03-17	04:45	
CME	2015-03-28	00:00	
CME	2015-03-31	08:32	
CME	2015-04-10	00:00	
CME	2015-05-06	01:41	
CME	2015-05-10	12:00	
CME	2015-05-18	19:00	

CME	2015-09-07	14:00	
CME	2015-11-06	18:18	
CME	2015-12-19	16:16	
CME	2015-12-31	00:50	
CME	2016-01-18	21:57	
CME	2016-03-05	10:00	
CME	2016-07-19	23:05	
CME	2016-07-24	15:00	
CME	2016-08-02	14:00	
CME	2016-10-12	22:01	
CME	2016-11-09	06:04	
CME	2017-04-04	01:00	
CME	2017-05-27	15:34	
CME	2017-07-16	05:59	
CME	2018-03-09	18:00	
CME	2018-06-06	11:00	
CME	2018-07-10	12:00	
CME	2018-08-25	02:00	
CME	2012-10-08	05:16	
CME	2012-10-12	19:00	

CME	2012-10-31	15:38	
CME	2012-11-12	23:11	
CME	2012-12-14	02:00	
CME	2013-01-17	16:00	
CME	2013-03-17	05:59	
CME	2013-04-13	22:54	
CME	2013-04-30	09:49	
CME	2013-06-06	02:55	
CME	2013-06-27	14:38	
CME	2013-07-05	01:00	
CME	2013-07-12	17:14	
CME	2013-10-02	01:54	
CME	2013-11-08	22:00	
CME	2013-11-30	20:00	
CME	2012-10-08	05:16	
CME	2012-10-12	19:00	
CME	2012-10-31	15:38	
CME	2012-11-12	23:11	
CME	2012-12-14	02:00	
CME	2013-01-17	16:00	

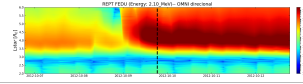
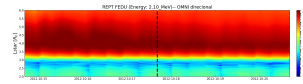
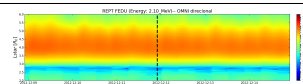
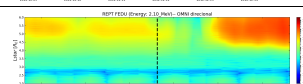
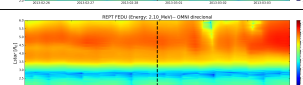
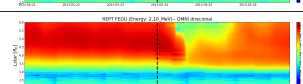
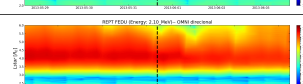
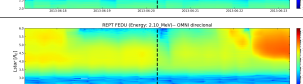
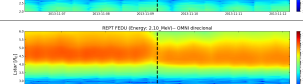
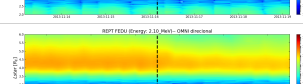
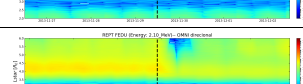
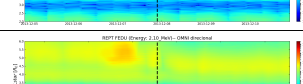
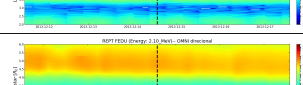
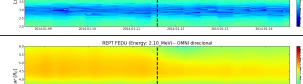
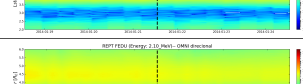
CME	2013-03-17	05:59	
CME	2013-04-13	22:54	
CME	2013-04-30	09:49	
CME	2013-06-06	02:55	
CME	2013-06-27	14:38	
CME	2013-07-05	01:00	
CME	2013-07-12	17:14	
CME	2013-10-02	01:54	
CME	2013-11-08	22:00	
CME	2013-11-30	20:00	
CME	2013-12-15	13:00	
CME	2013-12-24	21:00	
CME	2014-02-07	17:05	
CME	2014-02-15	13:16	
CME	2014-02-19	03:48	
CME	2014-04-05	10:00	
CME	2014-04-11	06:00	
CME	2014-04-29	20:00	
CME	2014-08-19	06:57	
CME	2014-09-12	15:53	

CME	2014-12-21	19:11	
CME	2015-01-07	06:16	
CME	2015-03-17	04:45	
CME	2015-03-28	00:00	
CME	2015-03-31	08:32	
CME	2015-04-10	00:00	
CME	2015-05-06	01:41	
CME	2015-05-10	12:00	
CME	2015-05-18	19:00	
CME	2015-09-07	14:00	
CME	2015-11-06	18:18	
CME	2015-12-19	16:16	
CME	2015-12-31	00:50	
CME	2016-01-18	21:57	
CME	2016-03-05	10:00	
CME	2016-07-19	23:05	
CME	2016-07-24	15:00	
CME	2016-08-02	14:00	
CME	2016-10-12	22:01	
CME	2016-11-09	06:04	

CME	2017-04-04	01:00	
CME	2017-05-27	15:34	
CME	2017-07-16	05:59	
CME	2018-03-09	18:00	
CME	2018-06-06	11:00	
CME	2018-07-10	12:00	
CME	2018-08-25	02:00	

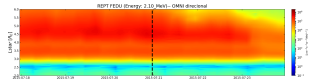
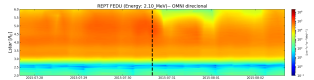
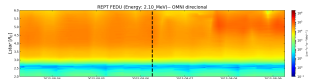
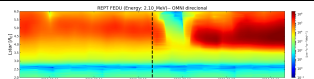
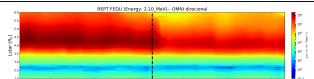
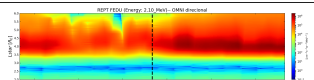
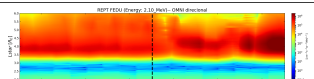
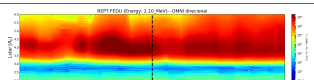
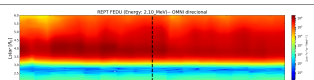
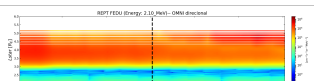
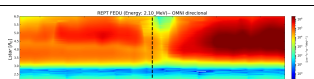
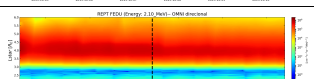
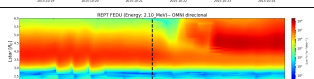
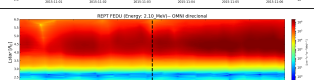
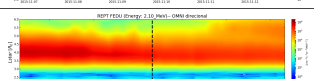
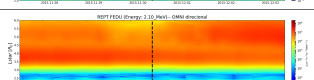
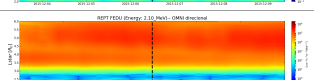
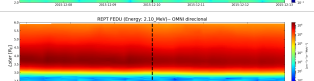
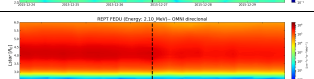
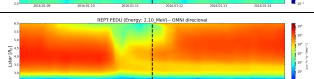
APPENDIX B - HSS EVENT DATES AND FLUX

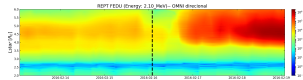
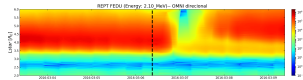
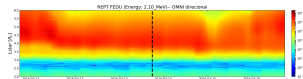
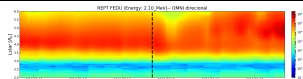
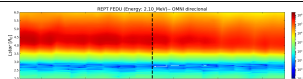
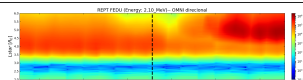
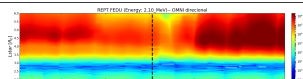
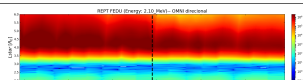
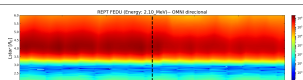
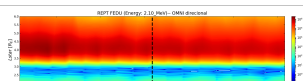
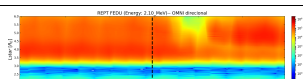
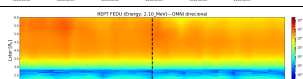
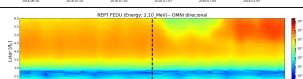
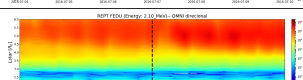
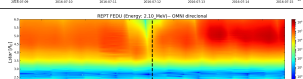
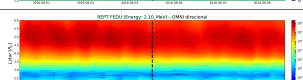
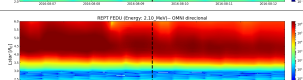
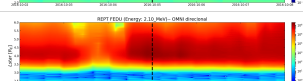
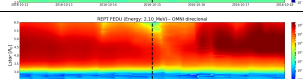
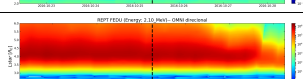
Table B.1 - All the events with flux variations related to HSS events. The columns represents the event type, the day that it occurs and the instant that the structure arrives and interact with Earth's magnetosphere. The last column show the 2.10 MeV electron flux density during the event, plotted with respect of L^* (y-axis) and time (x-axis). The period corresponds to 3 days before and after the event, marked with the dashed black line in each graph.

Event	Day	Hour	Flux
HSS	2012-10-09	18:30	
HSS	2012-10-17	16:30	
HSS	2012-12-11	22:00	
HSS	2013-02-28	15:00	
HSS	2013-05-23	22:45	
' HSS	2013-05-31	15:45	
HSS	2013-06-20	06:00	
HSS	2013-11-09	06:30	
HSS	2013-11-16	03:56	
HSS	2013-11-29	12:00	
HSS	2013-12-07	21:30	
HSS	2013-12-14	13:30	
HSS	2014-01-11	14:00	
HSS	2014-01-21	13:10	
HSS	2014-01-28	12:12	

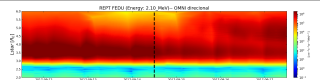
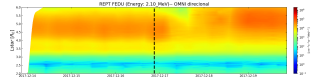
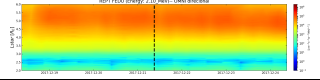
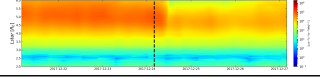
HSS	2014-02-09	11:27	
HSS	2014-03-12	19:49	
HSS	2014-03-18	04:02	
HSS	2014-03-18	06:24	
HSS	2014-04-07	11:04	
HSS	2014-05-01	18:00	
HSS	2014-06-10	11:30	
HSS	2014-07-15	00:00	
HSS	2014-07-21	22:00	
HSS	2014-07-28	03:12	
HSS	2014-08-01	00:00	
HSS	2014-08-10	12:00	
HSS	2014-08-28	00:00	
HSS	2014-09-19	00:00	
HSS	2014-10-04	17:40	
HSS	2014-10-13	11:00	
HSS	2014-10-20	08:00	
HSS	2014-10-30	21:56	
HSS	2014-11-01	06:33	
HSS	2014-11-05	00:00	

HSS	2014-11-15	20:59	
HSS	2014-12-01	16:36	
HSS	2014-12-06	12:05	
HSS	2014-12-11	22:00	
HSS	2015-01-05	00:00	
HSS	2015-01-21	00:17	
HSS	2015-02-01	00:00	
HSS	2015-02-08	06:00	
HSS	2015-02-17	12:13	
HSS	2015-02-23	04:20	
HSS	2015-02-28	12:00	
HSS	2015-02-28	18:06	
HSS	2015-03-16	00:00	
HSS	2015-03-28	04:01	
HSS	2015-04-15	03:15	
HSS	2015-05-12	17:20	
HSS	2015-06-08	00:16	
HSS	2015-07-04	11:59	
HSS	2015-07-10	18:30	
HSS	2015-07-14	21:00	

HSS	2015-07-20	23:14	
HSS	2015-07-30	16:00	
HSS	2015-08-06	06:24	
HSS	2015-08-15	07:41	
HSS	2015-08-23	07:15	
HSS	2015-08-28	16:00	
HSS	2015-09-07	12:22	
HSS	2015-09-11	06:43	
HSS	2015-09-14	07:35	
HSS	2015-10-04	01:00	
HSS	2015-10-07	13:00	
HSS	2015-10-21	09:48	
HSS	2015-11-03	05:29	
HSS	2015-11-09	19:00	
HSS	2015-11-30	07:48	
HSS	2015-12-06	11:52	
HSS	2015-12-10	00:13	
HSS	2015-12-26	20:24	
HSS	2016-01-11	12:00	
HSS	2016-01-21	10:00	

HSS	2016-02-16	01:55	
HSS	2016-03-06	09:00	
HSS	2016-03-13	18:00	
HSS	2016-03-14	16:20	
HSS	2016-04-22	12:17	
HSS	2016-05-01	13:30	
HSS	2016-05-08	01:21	
HSS	2016-05-14	21:33	
HSS	2016-05-21	01:02	
HSS	2016-05-23	04:00	
HSS	2016-06-04	23:00	
HSS	2016-07-02	18:00	
HSS	2016-07-07	00:00	
HSS	2016-07-12	00:00	
HSS	2016-08-03	12:15	
HSS	2016-08-09	08:57	
HSS	2016-10-05	00:00	
HSS	2016-10-15	00:00	
HSS	2016-10-25	09:29	
HSS	2016-11-08	06:00	

HSS	2016-11-10	16:38	
HSS	2016-11-12	10:00	
HSS	2016-11-12	10:00	
HSS	2017-03-27	00:00	
HSS	2017-04-05	18:00	
HSS	2017-04-07	18:00	
HSS	2017-04-11	20:00	
HSS	2017-04-18	18:02	
HSS	2017-04-21	11:20	
HSS	2017-05-19	18:08	
HSS	2017-06-02	06:00	
HSS	2017-06-03	06:00	
HSS	2017-06-05	08:30	
HSS	2017-07-08	23:13	
HSS	2017-07-20	12:00	
HSS	2017-08-17	08:00	
HSS	2017-08-31	04:40	
HSS	2017-09-04	19:12	
HSS	2017-09-05	06:30	
HSS	2017-09-14	00:00	

HSS	2017-09-14	12:00	
HSS	2017-12-16	21:00	
HSS	2017-12-21	09:00	
HSS	2017-12-24	04:00	

PUBLICAÇÕES TÉCNICO-CIENTÍFICAS EDITADAS PELO INPE

Teses e Dissertações (TDI)

Teses e Dissertações apresentadas nos Cursos de Pós-Graduação do INPE.

Manuais Técnicos (MAN)

São publicações de caráter técnico que incluem normas, procedimentos, instruções e orientações.

Notas Técnico-Científicas (NTC)

Incluem resultados preliminares de pesquisa, descrição de equipamentos, descrição e ou documentação de programas de computador, descrição de sistemas e experimentos, apresentação de testes, dados, atlas, e documentação de projetos de engenharia.

Relatórios de Pesquisa (RPQ)

Reportam resultados ou progressos de pesquisas tanto de natureza técnica quanto científica, cujo nível seja compatível com o de uma publicação em periódico nacional ou internacional.

Propostas e Relatórios de Projetos (PRP)

São propostas de projetos técnico-científicos e relatórios de acompanhamento de projetos, atividades e convênios.

Publicações Didáticas (PUD)

Incluem apostilas, notas de aula e manuais didáticos.

Publicações Seriadas

São os seriados técnico-científicos: boletins, periódicos, anuários e anais de eventos (simpósios e congressos). Constam destas publicações o Internacional Standard Serial Number (ISSN), que é um código único e definitivo para identificação de títulos de seriados.

Programas de Computador (PDC)

São a seqüência de instruções ou códigos, expressos em uma linguagem de programação compilada ou interpretada, a ser executada por um computador para alcançar um determinado objetivo. Aceitam-se tanto programas fonte quanto os executáveis.

Pré-publicações (PRE)

Todos os artigos publicados em periódicos, anais e como capítulos de livros.